Design improvements of negative refractive index metamaterial and characterization of refractive index discontinuity in effective parameters retrieval algorithm

Antoine Yann Wegrowski

A dissertation
submitted in partial fulfillment of the
requirements for the degree of

Doctor of Philosophy

University of Washington

2021

Reading Committee:

Wei-Chih Wang, Chair

Per Reinhall, Chair

Albert Kobayashi

Program Authorized to Offer Degree:
Mechanical Engineering

University of Washington

Abstract

Design improvements
of negative refractive index metamaterial
and characterization of refractive index discontinuity
in effective parameters retrieval algorithm

Antoine Yann Wegrowski

Co-Chairs of the Supervisory Committee:
Professor Wei-Chih Wang
Mechanical Engineering

Professor Per Reinhall
Mechanical Engineering

For the past 20 years, metamaterials have been investigated as a promising tool for sub-wavelength image rendition and cloaking device. Sometimes termed "double negative" materials, they possess the peculiar characteristic of displaying, over a certain range of frequencies, both negative permeability and negative permittivity, a characteristic which has been demonstrated to lead to a negative refractive index. Research on metamaterials faces many challenges, from constraints of negative refraction to impractical frequency spectra, to consistenly highly lossy designs. In this thesis, we present an overview of the history of the research on metamaterials, from its conceptual imagination by Veselago to a detailed analyzis of the currently most common designs. We discuss in details the Nicolson-Ross-Weir (NRW) algorithm and the Chien and Hsieh effective boundary retrieval algorithms, all of which are extensively used in the field of metamaterial research as a way to determine the effective parameters of metamaterials. In addition, we present a novel design and demonstrate its superior characteristics, for various ranges of frequencies and scales, compared to mainstream metamaterial: lower loss, lower negative refractive index and larger span of frequencies dur-

ing which negative refraction occurs. Finally, we present an additional challenge observed in the literature: reports of discontinuity in the refractive index. We analyze those reports and offer explanations for this phenomenon, as well as a numerical method to overcome this challenge.

TABLE OF CONTENTS

LIST OF FIGURES

GLOSSARY

FOM: Figure Of Merit

NIM: Negative (refractive) Index Material

NWR: Nicolson-Ross-Weir (method/algorithm)

SCR: Split Cylinders Resonator

SRR: Split Ring Resonator

ACKNOWLEDGMENTS

The author wishes to express sincere appreciation to his research adviser, Dr. Wei-Chih Wang, for his continued guidance and financial support, as well as the opportunity to visit on several occasions, as a visiting scholar, the Microtechnology Lab of the National Tsing Hua University of Taiwan, and to discover by the same occasion the rich and vibrant culture of Taiwan.

The author also thanks the Department of Physics and the Department of Mechanical Engineering of the University of Washington for funding part of his Ph.D. program through teaching assistantship. Special feelings of appreciation go to Prof. Nikolai Tolich for continued trust in the author's services.

Oftentimes a doctorate is recognized as a journey testing one's mental resilience. The author expresses his most sincere gratitude for the comforting presence and moral support of his peers: Dalin Williams, Fuki Miyamoto, Robert Masse, Konrad Kalpen, Weikun Hu, Jack Gullick, Tiffany Gentle, Adam Frost, Brian Connelly, Nikki Boggs, Bachir Bastien, Adrien Barton, Ibrahim Alawadhi, and Jakub Aftowicz.

Chapter 1

INTRODUCTION

1.1 Veselago's negative refractive index

The propagation of electromagnetic waves in a given material are governed by two complex quantities characteristic of that material: the permittivity ε, and the permeability μ. These two quantities are used to define a third one, the refractive index n, given by the Maxwell relation (1.1).

$$n^2 = \varepsilon\mu \tag{1.1}$$

This refractive index has been believed to be always positive, until 1968, when Veselago [78] introduced the idea of a substance that can have a negative refractive index. He hypothesized a material whose permittivity ε and permeability μ are negative and demonstrated that, in such a case, n has its real part taking a negative value out of the two possible, opposed in sign, solutions of 1.1.

Veselago showed that this result does not violate any law of physics, and described how familiar effects, such as the Doppler effect or the Vavilov-Cherenkov radiation, would be counterintuitively modified when taking place within negative refractive index materials (henceforth NIM). While Veselago suggested a way to produce such NIMs, his results received at the time very little attention, dismissed as theoretical fantasy, as no naturally occurring material presented this feature.

1.2 Expreimental Realization of NIMs and applications

It was not until 2000 that Smith *et al.* [70] produced a composite medium displaying the double negative permittivity and permeability Veselago predicted. This material, by the fact that it was composite and displayed exotic characteristics, *i.e.* characteristics not found

in nature, fitted the definition of metamaterials. This experimental realization caused an explosion of interest toward NIMs. A major figure in this initial impetus was John Pendry, who, a few months after Smith *et al.*, suggested that a lens made of NIMs would beat the "natural" lenses resolution (*i.e.* no smaller than a wavelength) [54], and in 2006 introduced, at the same time as, yet independently from, Ulf Leonhardt, the idea of an invisibility cloak [53, 36]. Such theoretical promises, quickly followed by experimental realizations [19, 75, 61], reinforced the academic interest surrounding negative refraction. While the original design by Smith *et al.* was based on the so-called split ring resonator (SRR), a variety of designs appeared throughout the following years [34, 81, 9, 89, 88, 14, 12, 17, 8]. Notably, the design that will be of interest in this thesis is the so-called fishnet structure, suggested by Zhang *et al.* [89].

Most of the proposed NIMs, Zhang *et al.*'s fishnet included, are *metasurfaces*, that is, films that can be laid on top of one another in order to create a layer of metamaterial of desired thickness [22] (see Fig. 1.1). Additionally, most NIMs are anisotropic and only display negative refraction when the plane wave incident upon them is polarized along one specific axis. These constrain the shapes and uses for which metamaterials can be used. 3D metamaterials do exist [7, 76, 27], but have been much more challenging to develop.

Another challenge is the limitations in transmission and frequency of operation of metamaterials. Most metamaterials developed so far are operable only in the infrared to microwave frequency range, as the development of negative refraction at optical frequencies meets serious technical challenges due to the dimensions constraints of the metamaterial's structure [74]. Metamaterials also display significant absorption around magnetic resonance; such absorption is often quantified using the Figure Of Merit (FOM), calculated as the ratio of the real to imaginary part of the refractive index. Absorption is evidently an undesirable effect to any application of metamaterials: a metamaterial-based imagery device would reduce the quality of the resolved image, while an invisibility cloaking system, typically designed for stealth, could be detected by noticing the unusual absorption of the system's location.

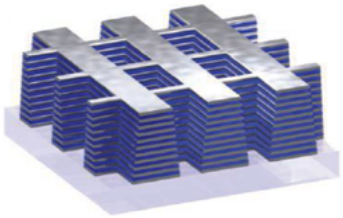

Figure 1.1: Fishnet metamaterial made of superposed layers of Au-Al_2O_3-Au sandwiches (reproduced from [8]).

1.3 The fishnet

1.3.1 Description

In 2005, Zhang *et al.* [89] managed to produce a NIM using a 60-nm-thick layer of aluminum oxide sandwiched between two 30-nm-thick layers of gold, the whole composite material being punctured with 360-nm-wide holes spaced 838nm apart in a square array. Such NIM displayed a refractive index of about -2 for incident light of 2μm of wavelength. Other NIMs based on a similar designed soon appeared, all gathered under the term "fishnets" (see Fig. 1.1).

1.3.2 Negative refractive index mechanism

Kafesaki *et al.* [28] detailed the mechanisms leading to the emergence of negative refractive index within the fishnet.

The idea is to combine negative permeability and negative permittivity within a slab of material sufficiently thin compared to the wavelength of the resonant frequency so that the material can be considered homogeneous from the point of view of the wavelength (Koschny *et al.* [31] suggests a ratio of wavelength-to-unit-cell-length of 30, although many proposed designed, including the metamaterials studied in this thesis, consider a much smaller ratio, with the unit cell length sometimes being bigger than the effective wavelength crossing the metamaterial).

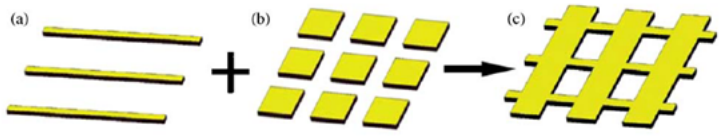

Figure 1.2: Deconstruction of one fishnet layer into its effective components (reproduced from [14]).

The two negative properties are obtained by separate mechanisms that are each more easily understood if, instead of considering the metamaterial as a dielectric sandwiched between two layers of metal and punctured in a square array (Fig. 1.2, c), we see the material as an array of metallic wires (Fig. 1.2, a) blended with larger square tiles made of a dielectric layer sandwiched between two metal layers (Fig. 1.2, b).

The **negative permittivity** is obtained through the array of metallic wires. As Pendry *et al.* [51] demonstrated, such an array behaves as a low-frequency plasma, displaying a negative permittivity below the plasmonic frequency. It is worth pointing out that, although Pendry *et al.* studied a cubic array of wires, they suggested the exact structure didn't matter, so that the same results can be applied to the parallelepipedal array of wires one finds in the fishnet structure.

The **negative permeability** is obtained thanks to the slab of dielectric material sandwiched between the metallic slabs. The plasmonic oscillation of the wires drives surface currents oscillating in opposite direction in the front and back metallic layer. The constantly accelerating and decelerating charged particles at the metallic surfaces create an oscillating magnetic field within the dielectric, leading, above resonance frequency, to negative permeability, as demonstrated by Pendry *et al.* [52].

1.4 Effective electromagnetic parameters retrieval

One way to retrieve the NIM's effective electromagnetic parameters, and in particular the refractive index, requires a knowledge of the complex transmission and reflection coefficients

of the wave incident to the material. Regardless of whether transmission and reflection are obtained by experiment or numerical simulation, one needs a way to convert these to the optical parameters.

Such an algorithm has been developed. In 1970, Nicolson *et al.* [44] are the first to derive the set of equations relating transmission and reflection to refractive index and impedance.

Chen *et al.* [11] in turn improved this algorithm, allowing the first boundary and thickness of the effective metamaterial (those being different from the physical boundaries and thickness of the metamaterial, as the electromagnetic wave is usually affected ahead and after the physical boundaries by the metamaterial) as well as the sign of the effective impedance and the branch of the real part of the refractive index to be determined. More recently, Hsieh *et al.* [24] suggested another method applied to bianisotropic materials and based on material dispersion models.

The most important assumption that the above algorithms rest upon is that of the material's *homogeneity*: the inhomogeneities within the material, mainly, its stratified composition and planar pattern, have to be designed within length scales that are very small compared to the free space wavelength of the incoming radiation (as an example, Ding *et al.*'s fishnet [14] is constituted of 30μm-thick unit cells, displaying negative refractive index for electromagnetic waves of wavelength 0.3mm, ten times larger).

In their article Chen *et al.* point out how, around resonance frequency, the wavelength within the material approaches the material's length scale, thereby excluding the possibility of a homogeneity assumption and making the situation one that is outside of the range of application of their algorithm. This is true inasmuch as the wavelength within a material equals the product of the wavelength in free space and the refractive index of the material: the larger the refractive index, the smaller the wavelength within the material. Regardless, this homogeneity assumption has often been disregarded in other papers [9, 88, 14, 12, 17, 8], who make the choice of presenting the results of the retrieval of effective electromagnetic parameters as accurate, even in the region of magnetic resonance, precisely where the wavelength of the radiation within the medium reduces to the same order of magnitude as the

thickness of the material. The fact that the algorithm's hypothesis is not verified in the window of frequency where magnetic resonance occurs is tantalizing since, as mentioned in section 1.3.2, this is precisely where the refractive index turns negative!

Smith *et al.* [72] solved this problem by suggesting an algorithm to retrieve effective electromagnetic parameters in an *inhomogeneous* material. The [9, 88, 14, 12, 17, 8] papers quoted above, however, do not refer to this method and insist on wrongly using Chen *et al.*'s algorithm.

One more algorithmic challenge, to which Smith *et al.* haven't brought an answer, is that of what we will henceforth refer to as the *m-branch index jump*. In the above algorithms, the expression of the refractive index contains an inverse cosine, and is therefore dependent on an associated m-branch, as can be seen in equation (4.11):

$$n = \frac{1}{kd}\cos^{-1}\left[\frac{1}{2S_{21}}\left(1 - S_{11}^2 + S_{21}^2\right)\right] + \frac{2\pi m}{kd} \tag{1.2}$$

The determination of such m-branch index is usually done using physical requirements on the system or by a requirement that the real part of the refractive index be continuous. Some metamaterials [17, 49, 8], however, have been reported to display a discontinuous refractive index, jumping from positive to negative, *i.e.* with the m-branch index jumping from one value to another. No consideration of this case seems to have been done when developing the above algorithms, leaving the decision of the frequency at which the m-branch index jump occur up to the arbiter of the researchers, such as in [17]. Some papers [49] do acknowledge the limits of the algorithm and the impossibility to decide where the jump occurs.

1.5 Thesis outline

In this thesis, we will present an overview of the mechanics of metamaterials from which negative refraction emerges. We will discuss in details the fishnet design and its electromagnetic dynamics, as well as the NRW algorithm and the Chen and Hsieh algorithms widely used to retrieve effective electromagnetic parameters from data of the transmission and reflection of a plane wave incident upon a tested metamaterial. In addition, we will present a novel

design for metamaterials and explain, with proof of numerical simulations, how this design achieves lower refractive index and lower loss than the fishnet. Finally, we will investigate three metamaterials which have reported the aforementioned m-branch index jump leading to a discontinuous refractive index, and offer a tool to tackle this problem as well as an analysis of the origin of this phenomenon.

Chapter 1 serves as an introduction, presenting quickly the history of metamaterial research and the fundamental concepts investigated in this thesis.

Chapter 2 takes a look at metamaterials, its definition and the challenges researchers are facing when striving to develop them. The two tenets of negative refraction, negative permittivity and negative permeability, are introduced, and Veselago's historical idea of negative refraction, as well as its consequences for effects such as ray optics, are presented. We then introduce the first realized metamaterial, the split ring resonator, and discuss its electromagnetic dynamic. We conclude this chapter with exposes of the two main possible applications of metamaterials: sub-wavelength optical systems, and invisibility cloaking.

Chapter 3 introduces the fishnet, the simplest and most widespread metamaterial. After discussion of its electromagnetic dynamics, we present the results of a numerical simulation of an example of fishnet, allowing us to illustrate the previously discussed dynamics. This dynamics is also investigated using a RLC circuit analogy. Finally, the impact of the dimensions of the fishnet on this dynamics is numerically investigated.

Chapter 4 explores the algorithms that have been developed to determine the effective parameters (permittivity, permeability, impedance, refractive index and boundaries) of metamaterials from the S-parameters retrieved experimentally or numerically. After developing the assumptions and deriving the basis of the algorithm, these algorithms are implemented as an example on the fishnet numerically simulated in Chapter 3.

Chapter 5 presents a novel metamaterial that we term the "bd design." The characteristics of the designs are explained in detail, and a thorough numerical analysis is performed in demonstrate the superior properties of this design. An analysis of the origin of these properties is finally performed.

Chapter 6 investigates three designs reported to demonstrate discontinuous refractive index. The details of those structures are reported and our numerical simulation is compared to that of the literature research. A geometrical approach is introduced in order to resolve the discontinuity observed, and this approach is carried out for the three designs. Finally, a discussion of the theoretical and numerical origins of this discontinuity and the effect on the propagating waves is carried out.

Chapter 7 concludes the thesis with an overview of the results presented and a discussion of future directions for this research.

Chapter 2
METAMATERIALS

In this chapter we present the concept of metamaterials. We begin with a definition of the term, then describe the two components that characterize the negative refraction distinctive to these materials: negative permittivity and negative permeability. In each case we present structures that have been devised to achieve negativity of those parameters, then merge those two characteristics in a description of Veselago's negative refraction formalism. Phenomena emerging with negative refraction, such as negative Doppler effect, negative Cherenkov radiation and negative refraction in geometrical optics, are detailed. An example of experimental realization of a metamaterial, the Split Ring Resonator, is introduced, and a few practical applications, such as invisibility systems and superlenses, are presented.

2.1 Introduction

Meta, in Greek, means "with, across, after." In the English language it is a multipurpose prefix used to denote a change in condition (metamorphosis), the fact that the object is located beyond a certain point (metacarpus) or that the object is of a higher order (metalanguage).

Although the history of metamaterials predates the word itself by many decades, this word was first coined and defined in 2001 by Rodger Walser to describe:

> "[...] unique composites with artificially narrowed distributions of heterogeneity. This narrowing can be exploited to generate a wide variety of interesting new materials, such as artificial magnetodielectrics, exchange spring magnets, ferroelectric and semiconductor superlattices, photonic crystals, etc. Heterogeneity is always introduced in these composites to localize excitations. Localization can either, selectively create (or annihilate) states that did not (or did) exist in the

constituent materials.[79]"

Over time, the term came to be debated, so that there doesn't seem to be an established definition within the scientific community [66]. Some researchers include photonic crystals into the metamaterial category. Others restrict the term to materials that are considered homogeneous on a scale of the light wavelength for which the material exhibits its metaproperties (defined thereafter), and therefore can be characterized at such wavelengths (see Chapter 4). Regardless, in the present thesis we will consider as metamaterials composite media characterized by:

- An internal man-made structure with typical dimensions of scale higher than the chemical structure's but lower than the wavelength of light at which the metaproperties emerge.

- Electromagnetic properties that are not found in materials unprocessed by the hand of man, typically negative permittivity and/or negative permeability (this will be referred thereafter as *metaproperties*).

Such structures are typically based on a repetitive pattern[1], consisting of identical unit cells that can be stacked so as to create a desired volume.

Ever since the first laboratory conception, such structures have been presenting challenges, especially in light of the potential applications postulated for metamaterials. The most important of those limitations are:

- **anisotropy**: many metamaterials are not isotropic media, so that the electric and displacement fields $\mathbf{E}$ and $\mathbf{D}$ do not find themselves parallel to one another and that the permittivity ε becomes a tensor. This means that the emergence of the metaproperties

[1]One could imagine a random structure with no definite regularity and typical structure dimensions much lower than the wavelegth of light at which the structure happens to exhibit metaproperties, for instance silica aerogels who would display metaproperties. Nonetheless the author hasn't heard of any metamaterial of this kind.

is dependent on the polarization and direction of propagation of the incoming wave. This puts limits on the applications of metamaterials to cloaking (see Section 2.6.1).

- **loss**: most electromagnetic materials, meta or not, dissipate electromagnetic energy, *e.g.* through heat radiation. Most of the applications considered for metamaterials require ideal transmission of the electromagnetic wave through the metamaterial, which motivates the pursuit of low-loss metamaterials. In non-meta materials the loss is quantified by the electric and magnetic loss tangents, *i.e.* the ratio of the imaginary part of, respectively, the permittivity or permeability, to their real part. In the case of metamaterials, a FOM is drawn, that can be understood as an "inverse of loss," and defined as the ratio of the real part of the effective refractive index to its imaginary part. Unfortunately, for most metamaterials, due to the mechanisms leading to the emergence of metaproperties, the span of frequencies of incident wave that causes metaproperties to emerge coincides with the span of frequency that causes single unit resonance in the structure, where a peak of loss is usually observed. This tantalizing fact notwithstanding, over the span of twenty years the effort for the research of a loss-less metamaterial have led to a hard-earned increase in FOM of three orders of magnitude, with FOM values sometimes extending beyond the thousand [40], although the typical FOM remains less than 10.

- **metaproperties emergence wave frequency**: as mentioned above, metamaterials are of interest for their electromagnetic properties. Such effective properties can only be calculated when the material is considered homogeneous to the eye of the indicent wave (see Chapter 4), *i.e.* only when the wavelength of the indicent wave is large compared to the structural dimensions of the metamaterial. This puts a first limit on the operational frequency of metamaterials. A second, stricter limit is the span of frequency at which the metamaterial displays its metaproperties. The first experimental realization of metamterial was operational at microwave frequency [70]; a broader range of frequencies have since been explored, extending, in the recent years, down to the optical range [16].

However, such materials, due to the first size constraint, require technology of higher precision to be conceived, so that more efforts have been dedicated to frequencies from infrared to radio.

- **industrial production**: following on the previous point, one challenge regarding the application of metamaterials such as cloaking or superlens is the capacity to mass-produce them. While milimiter-sized cloaking has been experimentally produced [61], such cloaking is restrained by its anisotropy and microwave frequency range of operation. 3D metamaterials, characterized by their isotropy, have yet to be produced large scale, as the unit cells need to be built manually one by one, rendering these metamaterials impractical for industrial production. That problem is even more so present in metamaterials operating with visible light, where the unit cells are even smaller.

As mentioned above, negative permittivity ε and negative permeability μ are two of the metaproperties of interest in metamaterials. Permittivity and permeability indicate how the material responds to, respectively, an incident electric field $\mathbf{E}$ and magnetic field $\mathbf{B}$, according to Maxwell's equations:

$$\nabla \cdot \mathbf{E} = \frac{\rho_v}{\varepsilon} \tag{2.1}$$

$$\nabla \cdot \mathbf{B} = 0 \tag{2.2}$$

$$\nabla \times \mathbf{E} = -\frac{\partial \mathbf{B}}{\partial t} \tag{2.3}$$

$$\nabla \times \mathbf{B} = \mu \mathbf{J} + \frac{1}{c^2}\frac{\partial \mathbf{E}}{\partial t} \tag{2.4}$$

In the following sections, I will detail the nature and specificity of metamaterials displaying, first, negative permittivity, then, negative permeability. I will then do the same

for Veselago media, *i.e.* metamaterials displaying both negative permittivity *and* negative permeability.

2.2 Negative permittivity

When negative permittivity occurs in a given media, the electric displacement vector **D** and the electric field vector **E** point in opposite directions, as permittivity is the constant of proportionality between one and the other. Such effect occurs in high-density ion gases as well as in ion-electron interactions at the surface of noble metals [56, 3]. In such media, n electrons of charge e and effective mass m_{eff} are collectively displaced from their original position respective to heavy, positive ions; the restoring force that goes against this displacement generates a simple harmonic oscillation at frequency [35]:

$$\omega_p = \sqrt{\frac{ne^2}{\varepsilon_0 m_{eff}}} \tag{2.5}$$

In such media the permittivity takes on the following form:

$$\varepsilon(\omega) = 1 - \frac{\omega_p^2}{\omega(\omega + i\gamma)} \tag{2.6}$$

From Eq. 2.6 one should note that, below plasma frequency ω_p, the real part of the permittivity becomes negative. Equally worthwile to note is the variable γ, a damping term associated with the dissipation of plasmonic energy into the system, which leads to an imaginary term for the permittivity whose ratio with respect to the real part of the permittivity gives an estimate of the importance of the dielectric loss occuring in the material. This shows there is only a given window of frequency below the plasma frequency for which we can have a negative permittivity medium that is not tainted by overwhelming loss.

While plasma in gases or at the surface of metals are not enough to make a material qualify as meta, if the conducting properties of a metallic structure can be changed to ressemble those of a dielectric, or, in the case of the rodded media presented in the next paragraph, a metallic structure can present *within itself* (*i.e.* not just at its surface) a plasmonic behavior,

the term metamaterial is applicable as there is transgression of the nature of the constituting elements.

Rotman [60] first developed, along with many other designs that would be used, 40 years later, as base for NIMs, the idea of the *rodded media* (see Fig. 2.1 for an example of anisotropic rodded media) as a way to generate plasmonic activity, basing his work on the research by Brown [5] on "artificial dielectrics."[2] Pendry [51] independently rediscovered that design in 1996 (not citing Rotman's work), with the added idea that "very thin wires are critical to applying the concept of plasmons to these structures" since plasmonic analogy of these structures rely on a very low electron density in the material, therefore on the structure being largely occupied by vacuum. Infrared negative permittivity can thus be reached, and extending the theoretical anlysis of its plasmonic behavior.

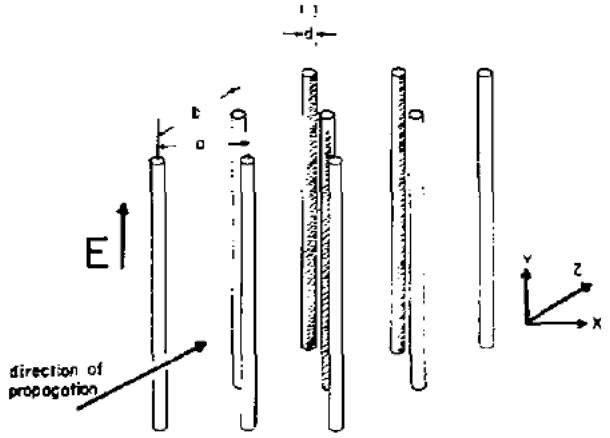

Figure 2.1: Rodded media: two-dimensional lattice with electric field propagating toward the z, polarized along the y. (reproduced from [60]).

The rodded media consists in variations of metallic wires arranged in a square array, the array being either unidirectional (as in Fig. 2.1), bidirectional or 3D, with consequences on the requirements of the direction of propagation and polarization of incident electromagnetic

[2]To note, Brown seems to only have focused on sub-unity permittivity, not negative permittivity.

waves. When excited by such an incident electromagnetic wave, the electrons at the surface of those wires start oscillating as surface plasmons; however, given the porous nature of the structure[3], consituted majoritarily of vacuum, the media as a whole behaves like a gaseous plasma. The effect of self-inductance $A(r)$ caused by the motion of the electrons along the wire, while not present in a regular gaseous plasma, does not modify the expression of the plasma frequency (Eq. 2.5) but instead is incorporated in the effective mass term m_{eff}:

$$m_{eff} = \frac{eA(r)}{v} = \frac{\mu_0 \pi r^2 e^2 n}{2\pi} \ln\left(\frac{a}{r}\right) \tag{2.7}$$

with v the electron velocity.

2.3 Negative permeability

The pursuit of negative permeability was a much harder task than that of negative permittivity, due to the reduction of variety of observed magnetic phenomena in nature compared to that of electric phenomena. Thompson [73] pointed out that ferromagnetic media display "apparent" negative permeability at resonance, from the fact that the magnetic flux density **B** and magnetic field strength **H** being related not by a scalar permeability but by Polder's tensor [57]:

$$\mathbf{B} = \begin{bmatrix} \mu & -i\kappa & 0 \\ i\kappa & \mu & 0 \\ 0 & 0 & \mu_0 \end{bmatrix} \mathbf{H} \tag{2.8}$$

This leads, in the case of z-propagated plane waves with circular polarization, to a transverse permeability:

---

[3]The density of electrons in the whole structure is $n_{eff} = n\frac{\pi r^2}{a^2}$ with n the electron density within the wires, r the wires radius and a the wires spacing. Following his own recommendation that wires be extremely thin, Pendry uses an example of $r = 1\mu m$ and $a = 5mm$ with aluminum wires ($n = 1.806 \cdot 10^{29}\mathrm{m}^{-3}$) to get $n_{eff} \sim 10^{22}\mathrm{m}^{-3}$, a value much closer to the electron density in gaseous plasma than to metals.

$$B_t = (\mu \pm \kappa) H_t \tag{2.9}$$

where, beyond a cutoff frequency, the κ term dominates, leading to an effective negative permeability.

Pendry [52] noted that the drawbacks of using ferrite to generate negative permeability were its heavy weight and brittleness, rendering it tedious to use. Instead, he suggested two microstructures displaying negative permeability: a capacitative arrays of metallic sheets wound on cylinders, and a "swiss roll" capacitor (Fig. 2.2, respectively b) and c)).

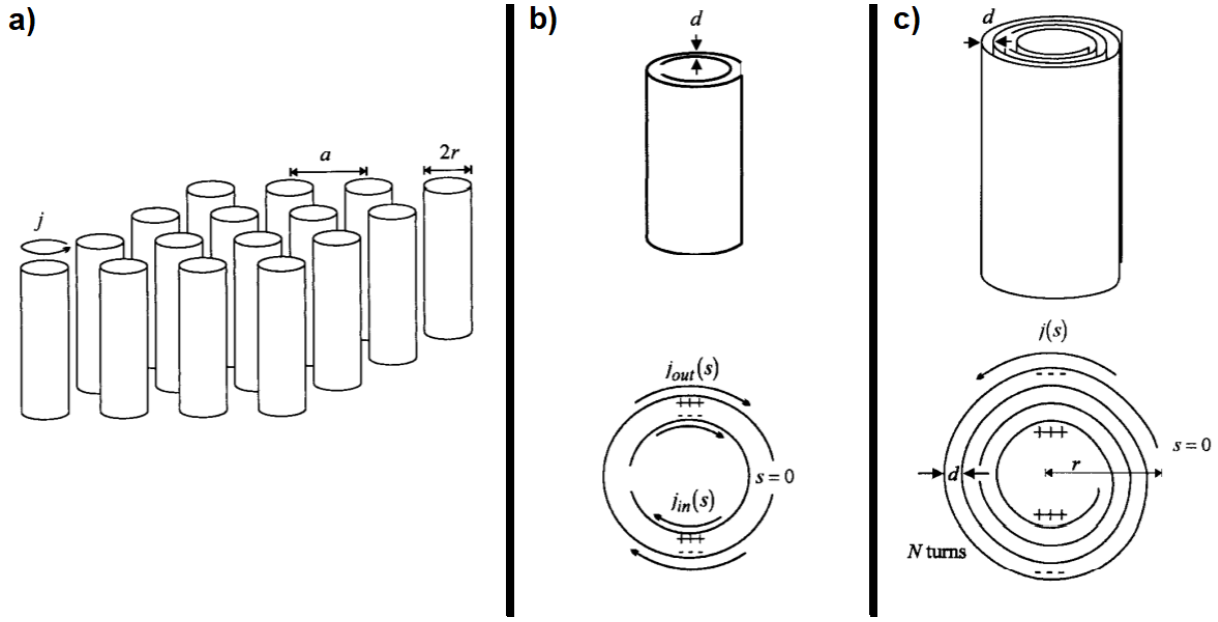

Figure 2.2: Microstructures proposed by Pendry: a) array of cylinders; b) capacitative arrays of sheets wound on cylinders; c) "swiss roll" capacitor (reproduced from [52]).

When an external magnetic field strength H_0 is applied onto these microstructures, aligned with the direction of the various metallic cylinders constituting the structures, this magnetic field strength generates an internal magnetic field strength H within the cylinders, leading to an expression for the effective permeability of[4]:

[4]Derivations and variables are made explicit in Appendix A.1

$$\mu_{\text{eff}}^{\text{cyl}} = \frac{\overline{B}}{\mu_0 \overline{H}_{ext}} = 1 - \frac{F}{1 + i\frac{2\sigma}{\omega r \mu_0}} \tag{2.10}$$

for the cylinder array, which itself does not display negative permeability but is an intermediate step toward that goal.

The capacitative arrays of sheets wound on cylinders, or split cylinders resonator (SCR) for short, however, does. This microsystem consists in a square array of concentric metallic cylinders with longitudinal gap running along in opposite sides of the cylinders, the gap acting as a capacitor that introduces a capacitance term in the permeability:

$$\mu_{\text{eff}}^{\text{SCR}} = \frac{\overline{B}}{\mu_0 \overline{H}_{ext}} = 1 - \frac{F}{1 + i\frac{2\sigma}{\omega r \mu_0} - \frac{3}{\pi^2 \mu_0 \omega^2 C r^3}} \tag{2.11}$$

When the frequency is such that the capacitance term $\frac{3}{\pi^2 \mu_0 \omega^2 C r^3}$ equals 1, the real part of the denominator goes to zero and the permeability becomes undefined. This happens at resonant frequency:

$$\omega_0 = \sqrt{\frac{3dc_0^2}{\pi^2 r^3}} \tag{2.12}$$

To be noted that over a short span beyond this frequency, determined by the coefficient $1-F$, the permeability *does become negative*, until the magnetic plasma frequency is reached:

$$\omega_{\text{mp}} = \sqrt{\frac{3dc_0^2}{\pi^2 r^3 (1 - F)}} \tag{2.13}$$

For typical values of $r = 2\text{mm}$, $a = 5\text{mm}$ and $d = 0.1\text{mm}$, that negative-permeability window extends from 2.94 GHz to 4.17 GHz.

In the case of the "swiss roll" capacitor, a single sheet of metal is rolled up on itself a number N of times, and similar sheets are arranged in a square array. A similar capacitative term, with this time $C = \frac{\varepsilon_0}{d(N-1)}$ with N the number of cylinder's rolling, is added to the emf calculation, making the permeability:

$$\mu_{\text{eff}}^{\text{swiss}} = \frac{\overline{B}}{\mu_0 \overline{H}_{ext}} = 1 - \frac{F}{1 + i\frac{2\sigma}{\omega r \mu_0 (N-1)} - \frac{dc_0^2}{2\pi^2 \mu_0 \omega^2 C (N-1) r^3}} \tag{2.14}$$

The diverging and plasma frequencies become:

$$\omega_0 = \frac{1}{\sqrt{2\pi^2 r^3 \mu_0 C (N-1)^2}} \tag{2.15}$$

$$\omega_{\text{mp}} = \frac{1}{\sqrt{F 2\pi^2 r^3 \mu_0 C (N-1)^2}} \tag{2.16}$$

For comparison, this leads, for similar r, a and d as above and the rolling number $N = 11$, the negative permeability window runs from 0.38 GHz to 0.539 GHz.

2.4 Veselago's negative refraction

One drawback of materials with either only the permittivity or only the permeability being negative is that the refractive index becomes evidently purely imaginary (Eq. 1.1), ruling out the possibility of any propagating wave. This is not the case in materials where *both* permittivity *and* permeability are negative.

In that special case, as in everything-positive materials, the Maxwell relation has two solutions, one positive and one negative. Considering a monochromatic wave with every quantity in Maxwell's equations (Eq. 2.1, 2.2, 2.3, 2.4) being proportional to $e^{i(kz-\omega t)}$, these equations become:

$$\mathbf{k} \times \mathbf{E} = \frac{\omega}{c} \mu \mathbf{H} \tag{2.17}$$

$$\mathbf{k} \times \mathbf{H} = -\frac{\omega}{c} \varepsilon \mathbf{E} \tag{2.18}$$

Negative parameters ε and μ force the trio $\mathbf{E}$, $\mathbf{H}$ and the phase vector $\mathbf{k}$ to become left-handed, unlike positive materials where they are right-handed. Considering along this fact the expression of the Poynting vector

$$\mathbf{S} = \mathbf{E} \times \mathbf{H} \tag{2.19}$$

and of the phase vector $\mathbf{k}$:

$$\mathbf{k} = \frac{n\omega}{c}\mathbf{e_S} \tag{2.20}$$

with $\mathbf{e_S}$ the direction of the Poynting vector, it is apparent that the phase vector and the Poynting vector are opposite in direction. The only term in Eq. 2.20 that could allow that opposition is the refractive index n that *has to be* negative [78].

This arrangement of $\mathbf{E}$, $\mathbf{H}$, $\mathbf{k}$ and $\mathbf{S}$ leads to curious consequences, three of which are thereafter presented.

The Doppler shift is an effect anybody is familiar with from the experience of the pitch drop heard when the hurling siren of an emergency car passes by. A similar effect happens with the frequency of electromagnetic waves. This drop in frequency is due to the fact that the received frequency of a wave is augmented, due to the relative motion, when the emitting object comes toward the receiver, while it is lowered in the opposite situation. But this effect assumes that the wave's phase velocity travels in the same direction as the wave's group velocity. As explained above, in the case of a NIM, this is exactly the contrary happening: the group velocity's direction $\mathbf{e_S}$ and the phase velocity's direction $\mathbf{e_k}$ are opposite, leading, in the case of a Doppler shift, to an *increase* of the received frequency when the emitting object goes from coming toward the receiver to going away from it.

Cherenkov radiations refer to electromagnetic radiations generated by a charged particle passing through a dielectric medium with a speed greater than the phase velocity k of that medium. Such radiations compounded along the trajectory of the particle lead to an "electromagnetic wake" reminding one of the supersonic boom shock wave. The angle between the particle's trajectory (assuming a straight one) and the wave vector of the Cherenkov radiation is:

$$\cos\theta = \frac{v_{\text{Cher}}}{v_{\text{p}}} = \frac{c}{n v_{\text{p}}} \tag{2.21}$$

with v_{Cher} the phase velocity of the Cherenkov radiation and v_{p} the phase velocity of the particle. One readily notes that, for positive values of the refractive index n, the radiation wake angle is always limited to positive values less than $\frac{\pi}{2}$. If, however, the refractive index were to change from a positive to a negative value, the sign of the left-hand-side of the equation would correspondingly change, shifting the radiation wake angle from θ to $\pi - \theta$. That is to say, in a NIM, where the phase velocity goes against the wave's group velocity, the Cherenkov radiation wake does not look like a cone pointing in the particle's direction of motion, but rather like a cone pointing *away* from it.

Lastly, a negative refractive index will have consequences in the framework of geometrical optics, where the law of refraction plays a significant role: as an electromagnetic wave transitions from a medium with refractive index n_1 to a medium with refractive index n_2, the wave's trajectory is refracted, passing from making an angle to the normal θ_1 when it crosses the interface, to exiting with an angle to the normal of θ_2, this according to Snell-Descartes law:

$$n_1 \sin\theta_1 = n_2 \sin\theta_2 \tag{2.22}$$

It is straightforward to see from this law that a change of sign in n_2 will cause a change of sign in θ_2, making the electromagnetic wave refract *on the same side of the normal* as the incoming wave (see Fig. 2.3).

Common effects due to refraction include the apparent discontinuity of a straw sitting in a glass of water, or the apparent proximity of fish to the surface of a river, an effect fishermen have been aware of long before the mathematical formalism was established [6].

In the case of NIM, the straw in the glass would appear flipped vertically: if the straw is resting on the upper left corner of the glass and ending on the lower right corner, the part of the straw in the water would, due to negative refraction, appear to start at the upper right

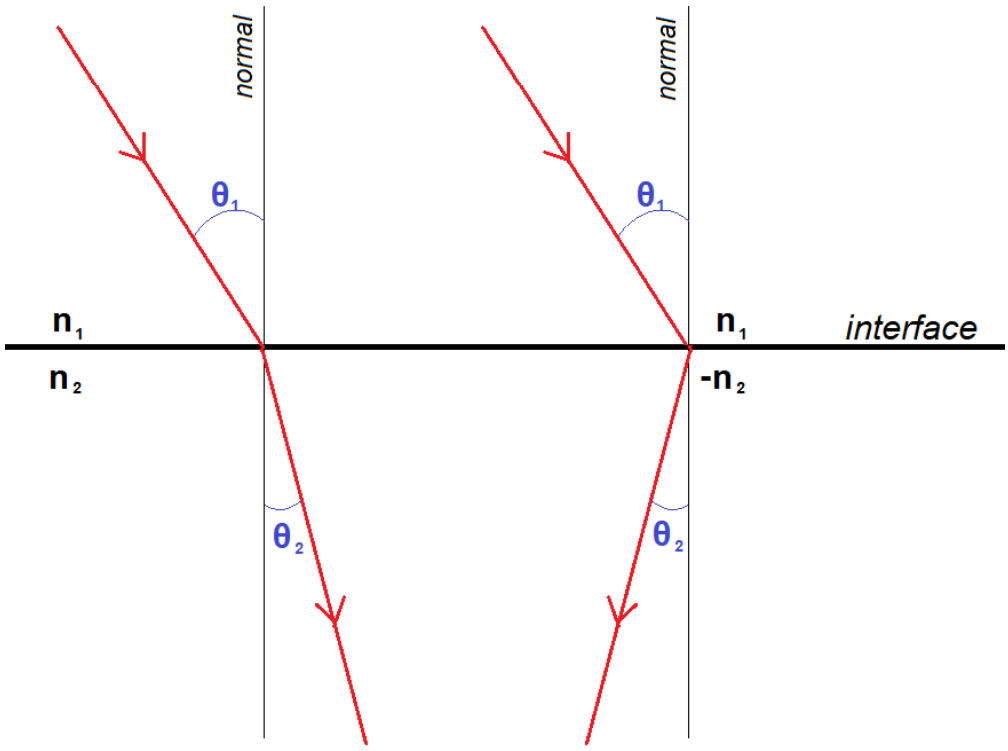

Figure 2.3: Trajectory of light in a positive-refractive-index medium (left) and a negative-refractive-index medium (right).

corner of the water volume and appear to end at the lower left corner of the glass. In both cases however, the straw would appear to be closer to the observer than it actually is.

Similarly, in the case of the fish in the river, the fish would actually appear to swim *above* the water; if the fish is facing away and swimming away, it would appear to be facing us, upside down, in a deformation that makes its convex face look concave, still appearing to swim away.

Negative refraction also have effect on the evolution of evanescent waves; this will be discussed in more details in Section 2.6.2.

2.5 The Split Ring Resonator and the first left-handed material

The anisotropy of the SCR poses two problems when considered for applications: it can only display negative permeability when the magnetic field strength is aligned with the cylinder's direction, and, if that is not the case, the component of the electric field parallel to the cylinders generate longitudinal surface currents that make the system behave as an effective metal.

A mofidication of the SCR allows to overcome these demerits: the array of split cylinders is replaced by a cubic array with each cubic surface covered with a slice of split cylinder (Fig. 2.4). Such material is readily realizable by printing metallic ink onto cubic units of intert material and stacking these cubic units as desired to form any shape. This configuration deals with the two problems above by 1) introducing an isotropy so that the material behaves in equal fashion regardless of the angle of approach of the incident wave, and by 2) reducing the height of the cylinders to a minimum, so that no longitudinal surface current take place.

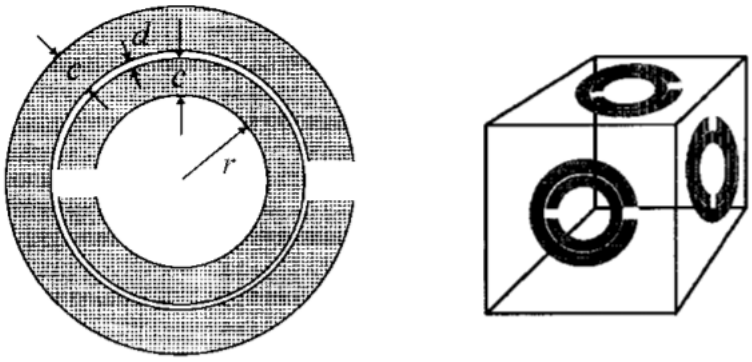

Figure 2.4: Split Ring Resonator (reproduced from [52]).

These modifications lead to a capacitance term of:

$$C_{\mathrm{SRR}} = \frac{\varepsilon_0}{\pi}\ln\frac{2c}{d} \tag{2.23}$$

with c and d defined in Fig. 2.4. A calculation similar to that which led to Eq. 2.14

returns a permeability of:

$$\mu_{\text{eff}}^{\text{SRR}} = 1 - \frac{F}{1 + i\frac{2a\sigma}{\omega r \mu_0} - \frac{3a}{\pi^2 \mu_0 \omega^2 C_{\text{SRR}} r^3}} \tag{2.24}$$

Incidentally, this structure allows for an additional benefit: it can be coupled with a wire array structure without the magnetic effect of the SRR and the plasmonic effect of the wire array significantly interfering with each other [70, 62, 71]. Obviously the laws of physics are not as simple as to allow two structures with particular characteristics to superimpose so that the resulting structure inherits of the characteristics of its composing structures. However, the SRR array has "blind spots" in between the SRR locations, where the inhomogeneities of the magnetic field generated by the SRR are absent; and similarly the wire arrays have magnetic "blind spots" in between each wires, where their own magnetic fields are minimal [38]. To be sure: interferences *do* occur to an extent, showing notably through a shift in resonant frequency from that of the wire array [68] and higher loss than in either component structures [69]; but not to the extent that negative permittivity and negative permeability effects are lost.

2.6 NIM applications

Beyond the purely fundamental interest, applications have been devised and tested regarding the use of NIMs. The most widely-known of these applications are presented thereafter: invisibility cloaking, and perfect lenses. To keep in mind, while the most discussed in the field those are by all means not the *only* one, other applications being found in electromagnetic wormholes [20], spontaneous emission control [45], photonic density of state engineering [26] or electromagnetic energy tunnelling [67].

2.6.1 Invisibility cloaks

Uses of metamaterials to invisibility cloaking have been postulated simultaneously by Ulf [36] and Pendry [53]. The idea is to use the engineerability of the refractive index to create

a matrix where light can be directed as desired, preventing the detection of an object placed inside a cavity within this matrix. Based on this principle, two effects of interest can be achieved:

- Effective invisibility, whereby the electromagnetic waves are bent around the cavity and emerge from the matrix with no discernable alteration (Fig. 2.5, left). Such configuration is effective for systems where an assumption is made regarding the background of the cloaked object (*e.g.* visible light observation), although its invisibility characteristics are not only limited theoretically [83, 42], but also practically due to inherent losses found in metamaterials, so that even if the contained object becomes undetectable the matrix itself would be. Recent progresses in low-loss metamaterials are nontheless encouraging [15, 85, 4]. Another issue is the reflectance which would similarily allow for detection of the matrix; similarly to loss, efforts have been taken to develop low-reflectance metamaterials [43].

- Blackbody invisibility, whereby the electromagnetic waves are captured by the matrix and none emerge, in the fashion of a black hole (Fig. 2.5, right). Such configuration is effective for systems that use a "pinging" mechanism, sending a signal and requiring a return signal to detect an object (*e.g.* radar detection). In that case, reflectance more than absorptance would become problematic, as the very idea behind this system is to prevent any rebound of incident wave.

2.6.2 Perfect lenses

NIM have been suggested to be a material of choice to be used for the realization of *perfect lenses* [54], although the idea initially stirred controversy [18, 58, 23]. Perfect lenses are lenses that allow an optical system to produce images with a resolution below the wavelength of the light used for observation, that wavelength being considered a "diffraction limit" when regular materials are used.

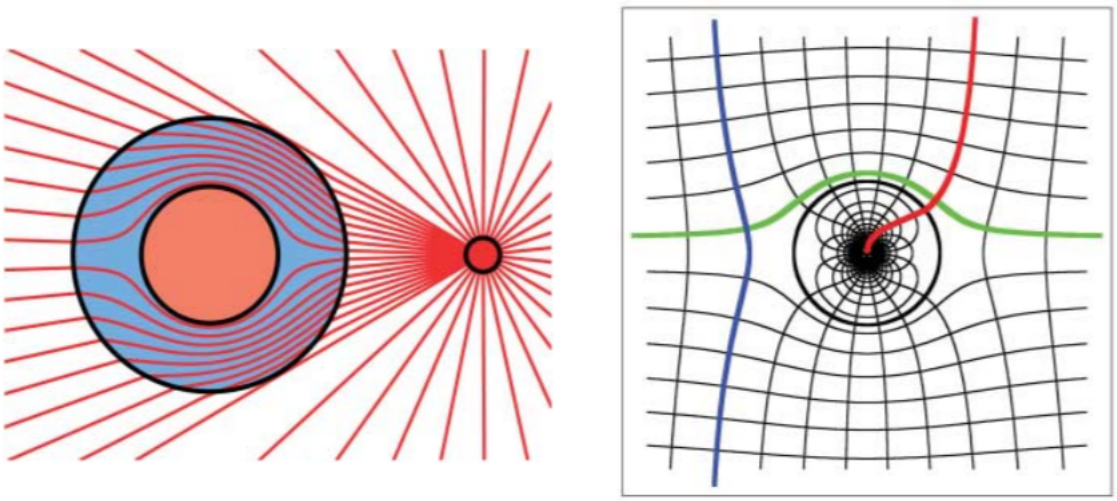

Figure 2.5: Two configurations of invisibility cloaking: effective invisibility (left, reproduced from [53]) and blackbody invisibility (right, reproduced from [36]).

The diffraction limit originates in the fact that, considering a propagating wave with constituting fields proportional to $e^{i(\mathbf{k}\cdot\mathbf{r}-\omega t)}$, the Maxwell equations require the following equality to be true:

$$k_0^2 = k_x^2 + k_y^2 + k_z^2 = \varepsilon_0\mu_0\frac{\omega^2}{c^2} \tag{2.25}$$

with $k_i = \frac{2\pi}{d_i}$ the Fourier components of the spatial variation (of typical dimensions d_i) in the source in the i direction. Assumming without loss of generality that a given wave propagates in the z direction, small spatial variations in the source will result in large $k_{x,y}$. When $k_x^2 + k_y^2 > k_0^2$, a negativity requirement falls upon k_z^2, making k_z imaginary. This k_z component then switches from the phase of each constituting field to become part of the magnitude term as a decaying exponential, what is refered to as an *evanescent wave*: the waves quickly decay to nil as it propagates away from the source.

For an object whose emerging light is incident upon a NIM, however, the expression of the transmission across the NIM-made optical system of thickness d results in an *amplification*

of the evanescent waves[5]:

$$T = \mathrm{e}^{-ik_z d} = \mathrm{e}^{+|k_z|d} \tag{2.26}$$

This way, even the smalled components of the object can be resolved by an optical system. Focus of the emerging light is easily secured by having the NIM's interface be flat and the thickness of the NIM be large enough so that the rays emerging from the first interface (NIM entry) reach a focal point within the NIM, then hit the second interface (NIM exit) before being negatively refracted to be focused again (see Fig. 2.6).

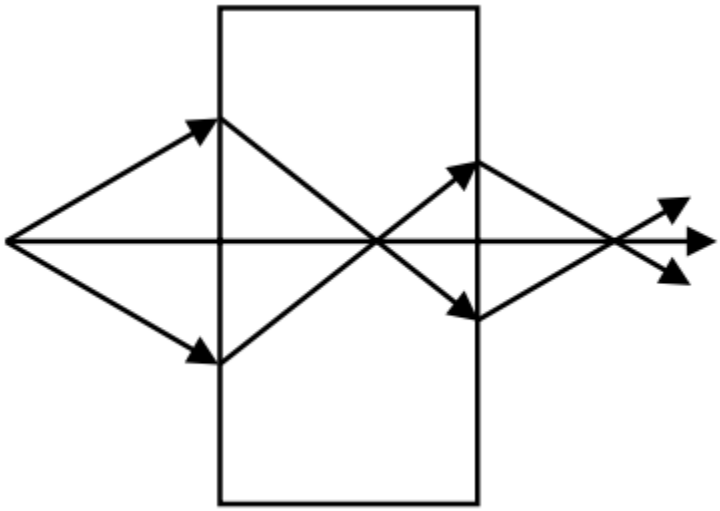

Figure 2.6: Trajectory of raylights when entering and exiting a NIM (reproduced from [54]).

This arrangement is however constrained by a few conditions:

- The object and the image will be placed in the near proximity of the NIM, otherwise the evanescent waves emerging from the object will exponentially decay to nil before having had the opportunity to reach the NIM and be enhanced.

[5]See Appendix A.2 for detailed calculation

- The analysis relies on the fact that the absolute values of the environment's parameters (permittivity and permeability) and the NIM's parameters be equal, *i.e.* $\varepsilon_{\text{env}} = -\varepsilon_{\text{NIM}}$ and $\mu_{\text{ext}} = -\mu_{\text{NIM}}$. This is obviously a very limiting constraint, but one that can be circumvented by having a system in the quasistatic limit, *i.e.* with the considered length scales much smaller than the wavelength, which is exactly the realm of application of the NIM. In this limit, the Fresnel coefficients become independent of the parameters.

2.7 Conclusion

In this chapter we have presented the concept of metamaterials. We began with a definition of the term, then described the two components that characterize the negative refraction distinctive to these materials: negative permittivity and negative permeability. In each case we presented structures that have been devised to achieve negativity of those parameters, then merged those two characteristics in a description of Veselago's negative refraction formalism. Phenomena emerging with negative refraction, such as negative Doppler effect, negative Cherenkov radiation and negative refraction in geometrical optics, were detailed. An example of experimental realization of a metamaterial, the Split Ring Resonator, was introduced, and a few practical applications, such as invisibility systems and superlenses, were presented.

Chapter 3

THE FISHNET

The fishnet is a powerful simplification of the SRR presented in Section 2.5. The fishnet is the metamaterial design that has led, since its creation by Zhang *et al.* in 2005 [88], to possibly the greatest number of variations, making metamaterial experimentation much more accessible to laboratories.

In this chapter, we present the fishnet design. We first describe the various components of this structure and explain what role they play in the emergence of metamaterial properties. We give a RLC circuit analogy through which we detail the effect of the fishnet's dimensions on its properties. Finally, we list the merits of the fishnet and some of its variations.

3.1 Introduction

The fishnet is structured as follows: a layer of dielectric (such as benzocyclobutene [14], gallium arsenide [17] or quartz [86]) is sandwiched between two layers of metal (such as gold [14], copper [49] or silver [15]), and this sandwich is punctured with rectangular holes arranged in a square array (Fig. 3.1, c). As for any metamaterial, the dimensions of the layers and the holes needs to be a few times less than the wavelength one wishes to use on the metamaterial.

In order to understand more easily the way the metaproperties emerge in the fishnet, one should consider it as an array of metallic wires (Fig. 3.1, a) blended with larger square tiles made of a dielectric layer sandwiched between two metal layers (Fig. 3.1, b).

The **negative permittivity** is obtained through the array of metallic wires. As Pendry *et al.* [51] demonstrated, such an array behaves as a low-frequency plasma, displaying a negative permittivity under a so-called plasmonic frequency (see Section 2.2). It is worth

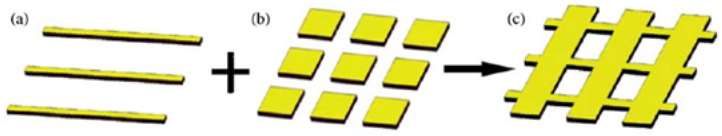

Figure 3.1: Deconstruction of one fishnet layer into its effective components (reproduced from [14]).

pointing out that, although Pendry *et al.* studied a cubic array of wires, they suggested the exact structure didn't matter, so that the same results can be applied to the parallelepipedal array of wires one finds in the fishnet structure.

The **negative permeability** is obtained thanks to the slab of dielectric material sandwiched between the metallic slabs. The plasmonic oscillation of the wires drives surface currents oscillating in opposite direction in the front and back metallic layer. The constantly accelerating and decelerating charged particles at the metallic surfaces create an oscillating magnetic field within the dielectric, leading, above resonance frequency, to negative permittivity, as demonstrated by Pendry *et al.* [52] (see Section 2.3).

In summary, the fishnet consists in an array of metallic wires simulating a plasma with a plasmonic frequency high enough to be superior to the magnetic resonance frequency of the dielectric.

The merits of the fishnet design are many. Its geometry allows for planar isotropy. It is much less complex than the SRR and therefore easily manufactured. Its simplicity also allows for manufacturing at a variety of dimensions and materials, from which follows the possibility of obtaining resonance at a variety of frequencies, from microwave to optical. Because its structure is so simple, it serves as a great basis for the development of more complex designs with a variety of properties.

3.2 Numerical analysis of the fishnet dynamics

The dynamics of an electromagnetic wave passing through the fishnet, while being approximated to equal that of an electromagnetic wave passing a homogeneous material, is actually more complex that its approximation. The negative refraction emerges from resonances of magnetic fields and surface currents, which we explain in detail in this section.

Because the fishnet can be molded in a variety of dimensions and using a variety of materials, we had to select a set of parameters to stick with in order to carry this numerical analysis. We opted for the following dimensions and materials, adapted from the work by Ding *et al.* [14]:

- For the dielectric, benzocyclobuten (BCB) was chosen, considering its properties of low loss and small dielectric constant in the terahertz range; for the metalic layer, gold was chosen;

- The dimensions were as follows: the wire in the magnetic field direction is 115μm wide, the wire in the electric field direction is 10μm wide, the unit cell is 150 by 150μm; the material's thickness were 0.4μm for the gold and 9μm for the BCB (see Fig. 3.2).

The simulation was carried applying the Frequency Domain Solver (using Finite Element Method) of the commercial software CST Microwave, with tetrahedral meshing of accuracy 1e-6 (resulting in 5,062 tetrahedrons over a single unit cell). The materials properties at terahertz range were determined following a Drude dispersion with plasma frequency $\omega_p = 1.37 \cdot 10^{16}$Hz and scattering frequency $\gamma = 4.05 \cdot 10^{13}$Hz for the gold metallic layer, and a dielectric constant of $\varepsilon = 2.56 + 0.015$i for the BCB. The simulation's frequency range was 0.6THz to 1.2 THz, with resonance achieved at 0.87THz.

We simulate a wave normally incident to the surface of the fishnet, polarized along the Y axis and travelling along the Z axis. The S ports are placed at the Z limits of the unit cell. Background medium is set to vacuum. Boundaries are defined as the limits of the unit cell for the X and Y boundaries, and to open boundaries for the Z boundaries.

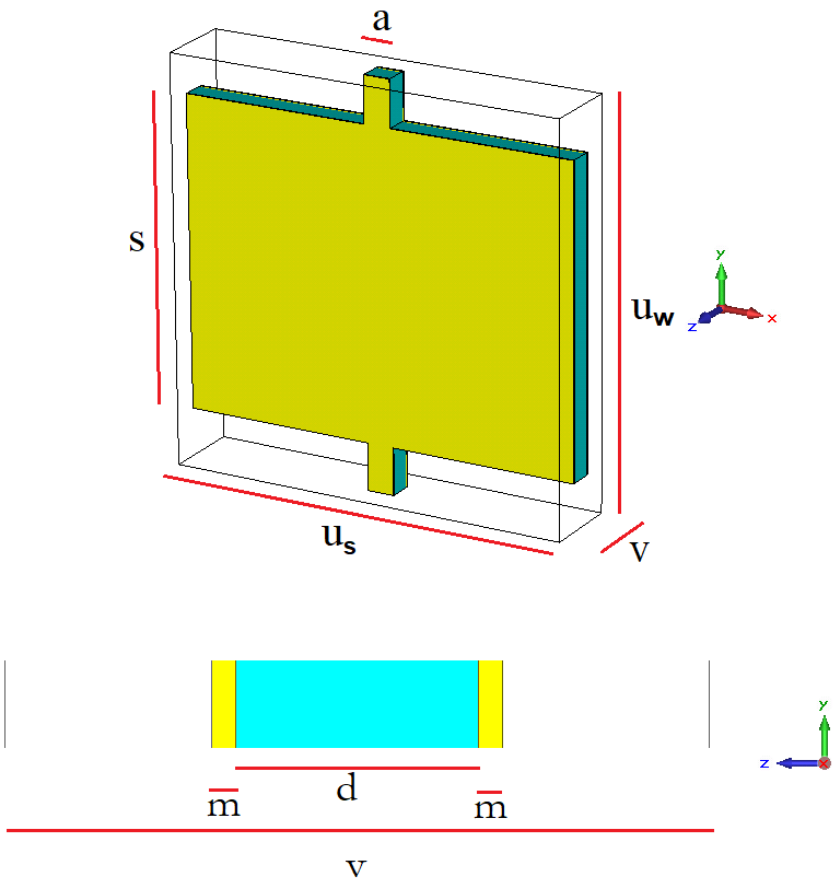

Figure 3.2: Design of the simulated fishnet for the purpose of the fishnet's typical behavior analysis. Dimensions are as follow: $a = 10\mu$m, $s = 115\mu$m, $u_s = u_w = 150\mu$m, $v = 30\mu$m, $m = 0.4\mu$m and $d = 9\mu$m.

The S-parameters obtained through the simulation are presented in Fig. 3.3. We observe a transmission shoulder starting at 0.9THz and expanding up to the limit of our simulation (1.2THz), culminating in an almost losless regime at around 1.1THz. The study of the negative refraction spectrum will be pursued in chapter 4. For now, it is worth noting that such S-parameter profile is qualitatively similar to other variations of the fishnet [28].

In the following two sections we will be analyzing the surface currents and inner magnetic fields generated by an incident electromagnetic wave at resonance.

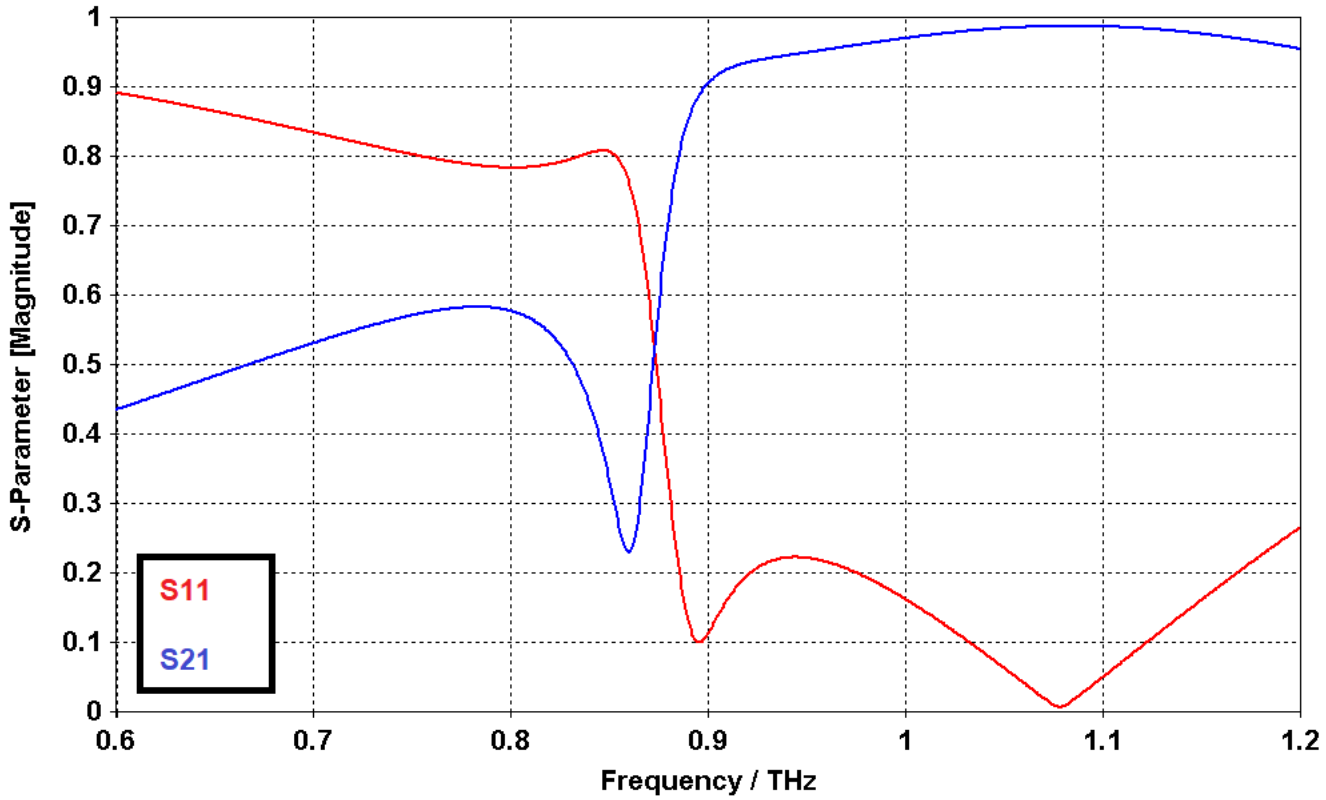

Figure 3.3: S-parameters of the simulated fishnet.

3.2.1 Surface currents

Fig. 3.4 depicts the surface current at the front surface of the fishnet, at resonance frequency (0.87THz, as determined from the effective parameters calculations carried in Chapter 4).

The surface charges oscillate between two points situated at the upper and lower extremities of the central slab on the lateral X boundaries. This oscillation of charges lead to surface currents that peak in two areas: the center of the central slab, and the fishnet's arm on the transversal Y boundaries.

It is noteworthy that the motion of the charges lead to currents in opposite directions in the arm and in the central slab: when one current goes towards the positive Y, the other goes towards the negative Y. Additionally, the surface currents in the front slab and the posterior

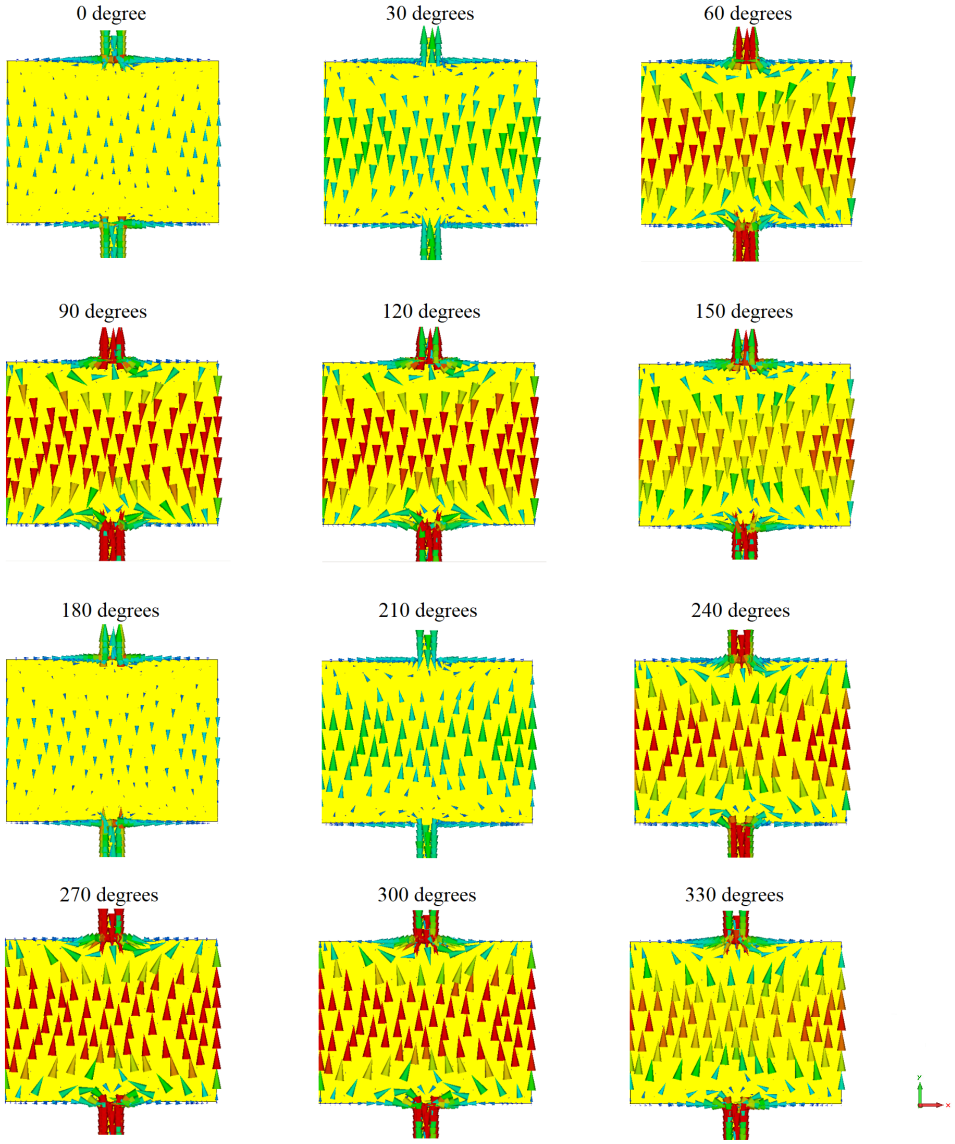

Figure 3.4: Intensity and direction of surface currents on the front surface (upon which the incoming wave is incident) at resonance, for various phase of the exciting electromagnetic wave.

slab are also opposite in direction, so that, along the Y boundary, charges accumulate in opposite upper/lower edges of the fishnet at a given instant.

3.2.2 Magnetic fields

Fig. 3.5 depicts the magnetic field on the surface within the dielectric slab equidistant to the front and back metallic slabs, at resonance frequency. As explained in Section 3.1, this magnetic field is driven by the surface currents on the metallic slabs, following Ampere's law. Noting the dynamics of the surface currents described in Section 3.2.1, we observe accordingly two oscillating magnetic fields: on the center of the central slab, a strong lateral oscillation occurs, driven by the up-and-down surface currents on the nearby metallic surfaces; on the arms however, a magnetic field of same order of magnitude oscillates *opposite* to the direction of the central slab's magnetic field oscillation. This is expected from the surface current that, on the arms, runs counter to the direction of the surface current on the arms. Another point of attention is that, due to these magnetic field oscillating in opposite directions, the central slab experiences its strongest magnetic field on the lateral X boundaries, with the arm's magnetic field "eating into" the central magnetic field along the Y axis. Supposedly, being able to attenuate or remove the arm's counter-magnetic field would allow for resonance in the central slab of higher intensity, leading to a more magnetically reactive material. This will be considered in Chapter 5.

3.3 RLC circuit analogy of the fishnet

The fishnet's properties, and the effect of the fishnet's dimensions on these properties, can be understood using a RLC circuit analogy. This analogy will be useful to get insight into the fishnet's electromagnetic dynamics.

The RLC model for the fishnet can be drawn from the decomposition presented in Fig. 3.1. We take as a starting point a model describing short slab pairs contiguous along the **H** direction, as described by Zhou *et al.* [90]. To this model we add the effect of additional inductance from the wires along the **E** direction, in order to obtain a representation of the

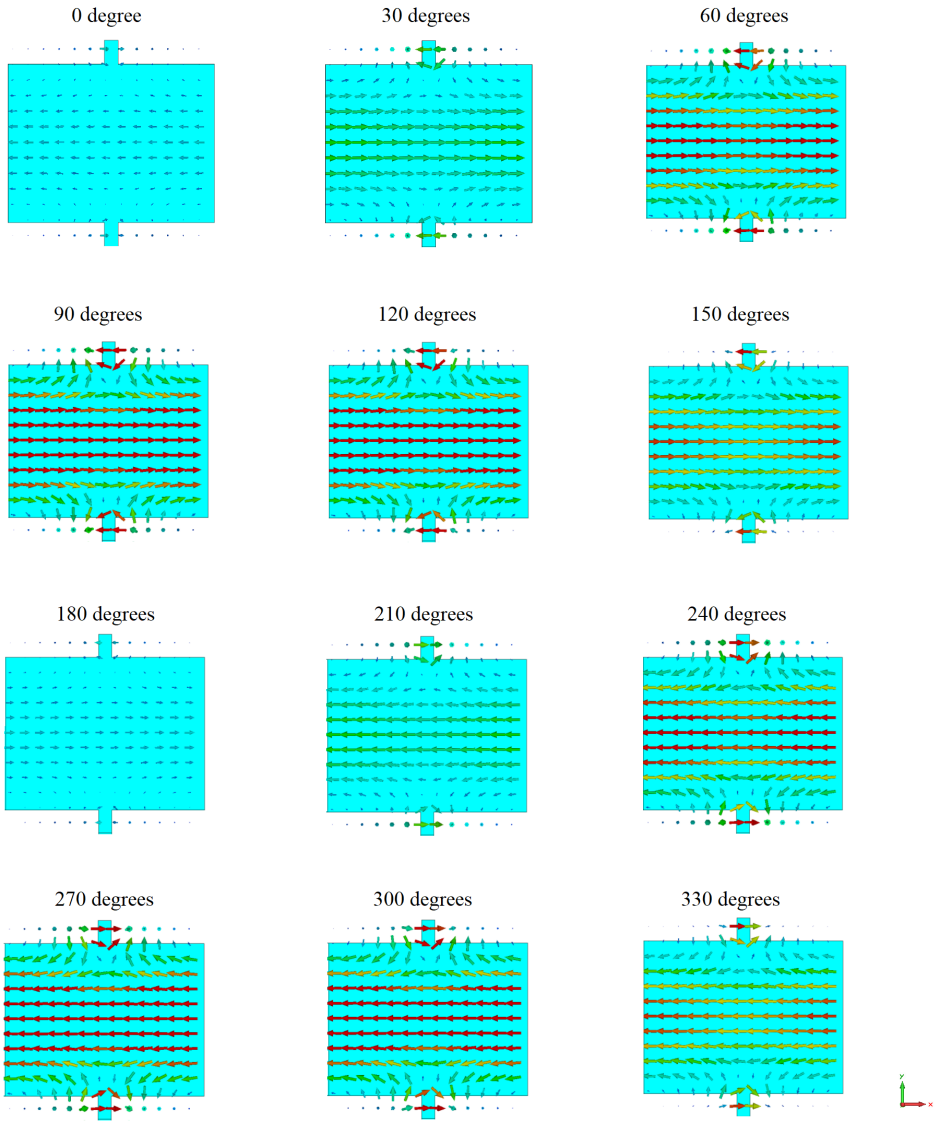

Figure 3.5: Intensity and direction of magnetic field within the dielectric slab at resonance, for various phase of the exciting electromagnetic wave.

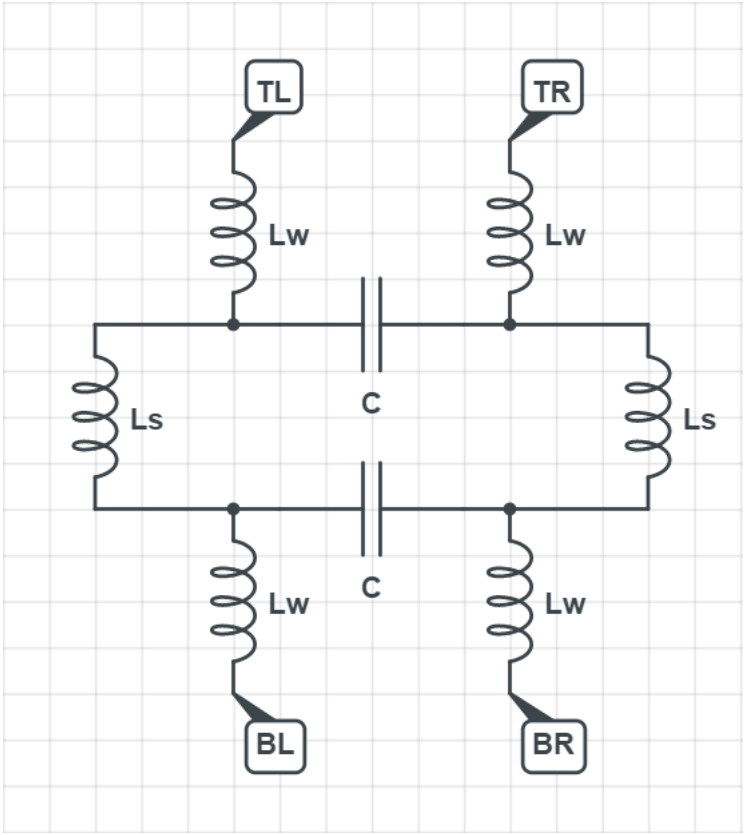

Figure 3.6: RLC model of the fishnet. C is the capacitance between the two central slabs, L_s the inductance associated with the central slab, and L_w the inductance associated with the wires. TL, TR, BL and BR and the connection points that allow for an extension of the system to a neighboring unit cell.

fishnet. Such a combination results in a RLC system as presented in Fig. 3.6.

This representation is equivalent to one unit cell of fishnet, and as such is an open circuit, with the top left (TL) and top right (TR) points being connected respectively to the bottom left (BL) and bottom right (BR) points of the adjacent unit cell. The inductance L_s is that associated with the central slab, while L_w is the inductance associated with the wires, while the capacitance of the central slabs is described by C. It is useful pointing out that those values depend on the design's dimensions as follows (refer to Fig. 3.2 for the definition of the dimension variables):

- the capacitance C is proportional to the central slab's surface $s \cdot u_s$ and inversely proportional to the separation of the central slabs (*i.e.* the thickness d of the sandwiched dielectric);

- the inductances L_w and L_s are both proportional to the length of circulation of the currents (respectively u_w for the wire and s for the central slab) and to the metallic plates separation (*i.e.* the thickness d of the sandwiched dielectric), and inversely proportional to the width of circulation of the currents (respectively a for the wire and u_s for the central slab).

Using the continuity between the TL/BL and TR/BR points, we can consider this as a closed circuit, which allows for an easier understanding of the circuit dynamics. In this frame of work, the opposite currents occuring in the central slab and the wires observed in Fig. 3.4 correspond to parallel currents along the inductances L_s and L_w.

The magnetic resonant frequency can be computed as:

$$\omega^2_{\text{fishnet}} = \frac{1}{LC} = \frac{1}{L_s C} + \frac{1}{L_w C} \tag{3.1}$$

Taking into account the relations of proportionality stated previously between the RLC variables and the fishnet's dimensions, we are able to express the dependence of the magnetic resonant frequency to the dimensions as:

$$\omega^2_{\text{fishnet}} \sim \frac{1}{s^2} + \frac{a}{s \cdot u_{\text{s}} \cdot u_{\text{w}}} \tag{3.2}$$

3.4 Fishnet dimensions impact on the transmission profile

We will now proceed to numerically investigate the impact of the various dimensions of the fishnet.

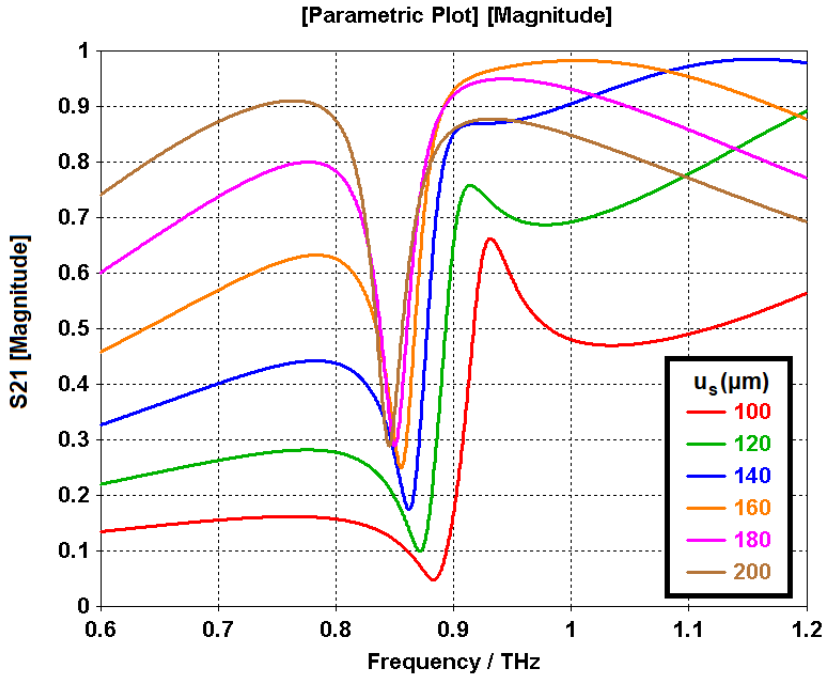

Figure 3.7: Transmission versus frequency for numerical simulations of the fishnet, varying the central slab's width u_s while maintaining all other dimensions constant.

3.4.1 The central slab's width u_s

Fig. 3.7 presents the transmission spectra of simulated fishnets with varying central slab width.

Eq. 3.2 indicates a larger u_s would lead to a lower resonant frequency. This is verified in Fig. 3.7, where we observe a shift to lower frequencies of the transmission profile as the parameter u_s is increased.

We also observe the reduction in magnitude of resonance as the parameter u_s decrease. In the limit where u_s tends to a, the fishnet becomes a simple arrangement of wires (in a sandwich arrangement akin to that of the fishnet). The reduction of the dielectric's dimensions leads to less material being available for magnetic resonance, leading to a weakening of the resonant effect.

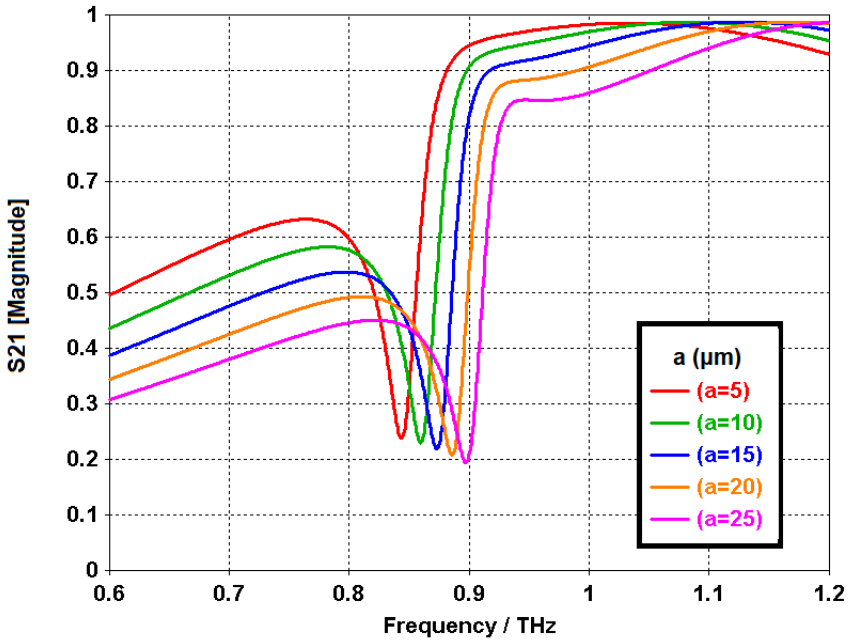

Figure 3.8: Transmission versus frequency for numerical simulations of the fishnet, varying the wire's width a while maintaining all other dimensions constant.

3.4.2 The wire's width a

Fig. 3.8 presents the transmission spectra of simulated fishnets with varying wire width.

From Eq. 3.2 we expect an increase of resonant frequency to follow from the increase of the wire's width. This comes from the decrease in wire-associated inductance, and is confirmed in Fig. 3.8. As understood from the analysis of the negative permittivity presented in Section 2.2, reducing the wire's width leads to a reduction of electron density in space, thereby reducing the plasma frequency (see Eq. 2.5).

3.4.3 The wire's length u_w

Fig. 3.9 presents the transmission spectra of simulated fishnets with varying wire width.

Following Eq. 3.2 we expect a regression in resonant wavelength to accompany an increase

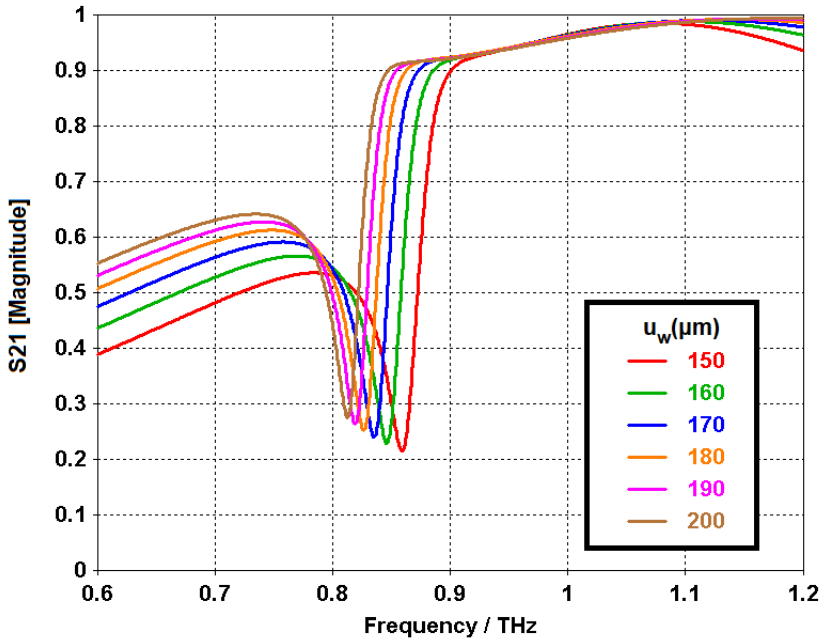

Figure 3.9: Transmission versus frequency for numerical simulations of the fishnet, varying the wire's length u_w while maintaining all other dimensions constant.

in the wire's length. This is verified in Fig. 3.9. Increasing the wire length leads to a decrease of the arm-induced inductance.

As discussed in Section 3.2.2, the magnetic field caused by the fishnet's wires runs counter to the magnetic field occuring in the central dielectric slab, weakening its effect. It is therefore expected that lengthening the fishnet's arms would put space between the antiparallelly oscillating magnetic fields in the wires and the central slab, thereby reducing the weakening effect of the wire's magnetic response on the central slab's response.

3.5 Electric dynamics of the fishnet

The fishnet's electric dynamics, leading to the emergence of negative permittivity, can be split, similarly to the magnetic dynamics, between the contribution of the wire array and that of the central slab. The former brings in a plasmonic, Drude-like contribution, while

the latter brings in a dipole-like contribution [90]. The fishnet's permittivity can be obtained by addition of the respective permittivities of those components [30], leading to a steeper dispersion relation and a lower plasma frequency that that of those individual components. Additionally, the lower the plasma frequency of the central slab, the greater the difference between the plasma frequency of the fishnet and that of the wire array. Because of this, the plasma frequency of the central slab needs to be kept as high as possible. This can be achieved by either wide central slabs, or by connecting the slabs to wires, the fishnet applying both of those methods [28].

Similarly to the RLC analogy for the magnetic dynamic of the fishnet, we can develop a RLC analogy for the electric dynamic of the fishnet, allowing to express the plasma frequency of the fishnet as:

$$\omega_e^2 = \frac{1}{L^e C^e} = \frac{1}{L_s^e C^e} + \frac{1}{L_w^e C^e} \tag{3.3}$$

with L_s^e the inductance of the central slab, L_w^e the inductance of the wires and C^e the capacitance of the central slabs.

The dependence of those variables on the dimensions of the fishnet is as follows [63]:

$$C^e \sim u_s \tag{3.4}$$

$$L_s^e \sim \ln\left(\frac{s}{u_s}\right) \tag{3.5}$$

$$L_w^e \sim \ln\left(\frac{u_w - s}{a}\right) \tag{3.6}$$

From this we can note that the central slab term's contribution to the plasma frequency (Eq. 3.3) actually increases with u_s.

For most of the fishnet variations, including the prototype considered in this chapter, the central slab's contribution to the plasma frequency is much larger than the magnetic resonant frequency, so that it does not affect the low-frequency electric dynamics of the wire array.

Plugging these relations into Eq. 3.3 we find that the plasma frequency is proportional to [28]:

$$\omega_e^2 \sim \frac{A}{u_s \ln\left(\frac{s}{u_s}\right)} + \frac{B}{u_s \ln\left(\frac{u_w - s}{a}\right)} \tag{3.7}$$

with A and B constants. This shows the fishnet's electric dynamics is essentially described by the Drude-like contribution of the wire array. This comes as an advantage for the fishnet, as a Drude-like permittivity changes more slowly than a permittivity generated by electric resonance, and leads to a broader span of frequencies where impedance can match free space and high transmittances can be achieved.

3.6 Conclusion

In this chapter we presented an overview of the fishnet, one of the most widespread designs of metamaterials. After a discussion of the emergence of the negative permittivity and negative permeability in the fishnet that lead to negative refraction, we conducted a numerical analysis of the fishnet's electromagnetic dynamics when excited by an electromagnetic plane wave normally incident to its surface. In particular, we discussed the dynamics of the fishnet's surface currents at resonance and of its internal magnetic field. Further, we developed a RLC analogy to the fishnet, allowing us to postulate dependence of the fishnet's dynamics on its dimensions. Finally, we numerically confirmed these dependences by means of simulations.

Chapter 4

EFFECTIVE PARAMETERS RETRIEVAL METHOD

In this chapter we present two methods used in the retrieval of effective parameters of metamaterials: the NRW method and the effective boundary retrieval method. For the former, we present the requirements for applicability of this method: homogeneity and passivity. We then explicit the mathematical formalism of this method. Finally, we present two variations of the effective parameters retrieval method: the Chen method, and the Hsieh method. We conclude by an application of these methods to the fishnet described in the previous chapter.

4.1 Introduction

By definition, metamaterials are composite materials that are considered as homogeneous for the purpose of their application. This entails the attribution to each metamaterial of *effective parameters* (permittivity, permeability, impedance, refractive index and spatial boundaries) that can be used when building systems involving metamaterials, as if the metamaterial were replaced by homogeneous materials with *characteristic parameters* of equal values.

It is important to note that, similarly to homogeneous materials which can display different characteristic parameters for various axes of propagation (*e.g.* birefringence), composite materials also have a propagative axis dependence on their effective properties, and few are the metamaterials that are completely isotropic. One should also keep in mind that flat metamaterials (called metasurfaces or metafilms) are refered to as isotropic, although the isotropy is only effective in a 2D plane corresponding to the material's plane [14, 55, 21]; a distinction is often made between 2D isotropy and 3D isotropy [65, 77, 33], the latter being what we refer to as "completely isotropic".

Methods to retrieve the characteristic parameters of materials are well-researched [1, 41, 64, 82] and typically involve measuring either standing electromagnetic waves within the material, waves reflected off the material, waves transmitted through the material, or investigating the material's electromagnetic resonance.

Clearly for metamaterial it is not expected that the electromagnetic waves within the metamaterial will behave as if in a homogeneous material, as the complex structure of the metamaterial will lead to a variety of surface currents and internal resonances that wouldn't be possible in a homogeneous material. This rules out any method that would investigate the propagation of electromagnetic waves within the metamaterial. Methods considering the reflected and transmitted waves are, however, expected to hold the same results, as these methods only rely on the waves that reach the limit ports around the material, the latter be homogeneous or composite.

The most popular of these methods is the Nicolson-Ross-Weir (NWR) method [44, 80], which allows to retrieve the permittivity and permeability of a material (meta or not) over a wide band of frequency, based solely on the transmission and reflection signal of a plane wave incident upon the material. We begin this chapter by describing the set of assumptions this method relies on.

4.2 NWR algorithm assumptions

4.2.1 Homogeneity

Considering that the metamaterial has effective parameters requires to assume that it can be treated as homogeneous, and therefore that the electromagnetic fields within the material are not responding to the components of the composite metamaterial but to the unit cell as a whole. In practice this demands an averaging of the electromagnetic fields over one unit cell, which can be established provided [52]:

- the unit cell's characteristic dimension be much smaller than that of the wavelength of the electromagnetic wave propagating within the metamaterial; otherwise, phenomena

such as internal diffraction and refraction would occur that would be impossible in an actually homogeneous medium;

- the unit cell be defined in such a way so that no component of the metamaterial's structure intersects with its boundaries; violation of this continuation leads to discontinuity of the averaged fields across the unit cell's boundaries;

4.2.2 Passivity

The metamaterials to which the NWR algorithm is applied are usually considered passive (although active metamaterials do exist [37, 10, 48]), meaning they do not generate power themselves, but instead act as dissipative, storing and/or transmittive media. Dissipation leads to a complex function of effective parameters, with the imaginary part of permittivity and permeability being related to the real parts through the Kramers-Kronig relations [25]. Passivity dictates that the total absorbed energy in a volume V of the medium be positive definite:

$$\frac{1}{2\pi}\int_V \mathrm{d}^3 r \int_{-\infty}^{\infty} \left[\mathrm{Im}(\varepsilon)\left|\mathbf{E}\right|^2 + \mathrm{Im}(\mu)\left|\mathbf{H}\right|^2\right] \omega \mathrm{d}\omega > 0 \tag{4.1}$$

which can be interpreted as the following requirement for imaginary parts of the permittivity and permeability [29]:

$$\mathrm{Im}(\varepsilon) \geq 0 \tag{4.2}$$

$$\mathrm{Im}(\mu) \geq 0 \tag{4.3}$$

the violation thereof would go in contradiction with the second law of thermodynamics.

Another, less constraining requirement, can be expressed using impedance and refractive index:

$$\mathrm{Re}(z) \geq 0 \tag{4.4}$$

$$\mathrm{Im}(n) \geq 0 \tag{4.5}$$

Nonetheless, this requirement is in practice observed only outside of the magnetic resonance window. Indeed, it has been numerically observed that some metamaterials display negative imaginary permittivity and/or negative imaginary permeability [32, 46], and the author witnessed how blind enforcement of those passivity requirements in those cases lead to discontinuous effective parameters (the impedance in particular) through sudden change of their sign, see Eq. 4.10 thereafter. Debate is ongoing regarding the origins of this phenomenon, some claiming it to be a result of low (but non-zero) losses [2], of the finiteness of the unit cell [32], of magnetoelectric coupling [87] or of simulation's numerical errors [84].

4.3 The NWR algorithm

As introduced in this chapter, the NWR algorithm relies on the analysis of the transmission and reflection coefficients (complex values respectively denoted T and R) of the metamaterial, as measured when an plane wave is incident upon the material. Given a slab of material of thickness d upon which is incident a plane wave of wave number k_0, these coefficients allow the calculation of the S-parameters:

$$S_{21} = Te^{ik_0 d} \tag{4.6}$$

$$S_{11} = R \tag{4.7}$$

These S-parameters can be expressed as functions of both the refractive index n and the impedance z of the material. Defining the gamma coefficient as $\Gamma = \frac{z-1}{z+1}$, the S-parameters become:

$$S_{21} = \frac{\Gamma\left(1 - e^{i2nk_0 d}\right)}{1 - \Gamma^2 e^{i2nk_0 d}} \tag{4.8}$$

$$S_{11} = \frac{\left(1 - \Gamma^2\right)e^{ink_0 d}}{1 - \Gamma^2 e^{i2nk_0 d}} \tag{4.9}$$

The inversion of these equation leads to:

$$z^2 = \frac{\left(1 + S_{11}\right)^2 - S_{21}^2}{\left(1 - S_{11}\right)^2 - S_{21}^2} \tag{4.10}$$

$$n = \frac{1}{k_0 d}\Big\{\big[\mathrm{Im}(\ln\Delta) + 2m\pi\big] - i\mathrm{Re}(\ln\Delta)\Big\} \tag{4.11}$$

with the coefficients $\Delta = e^{ink_0d} = \Theta \pm i\sqrt{1-\Theta^2}$ and $\Theta = \frac{1-S_{11}^2+S_{21}^2}{2S_{21}}$ and the variable m the branch index of the coefficient Δ.

One notices that, due to the square terms in Eq. 4.8 and 4.9, the expression of the impedance z and refractive index n are affected on a sign uncertainty. The usual method to lift this uncertainty is to follow the passivity requirements (Eq. 4.2-4.5), which holds outside of the spectral window of magnetic resonance, and apply a condition of continuity of the effective parameters when the passivity requirements fail around the window of magnetic resonance [24]. The m branch index is usually determined in a similar fashion. We will however see in Chapter 6 how the identification of the m branch index around magnetic resonance can sometimes be unclear due to a violation of the continuity of the refractive index.

4.4 Effective dimensions of the metamaterial

Due to the possibly highly scattering nature of metamaterial caused by the distribution of its metallic components, the physical boundaries of the unit cell do not always correspond to the locus where the incident plane wave loses its planarity (unlike the case of a homogeneous material). The incident wave can therefore appear to be incident upon an effective material ahead of the physical boundary of the metamaterial. It is therefore necessary to determine the effective thickness of the metamaterial's unit cell.

Several methods [11, 24] have been proposed to identify this effective boundary, relying on the assumption that that boundary would be such that variations of the metamaterial conglomerate's thickness (constituted of several unit cells) would have no, or little, effect on the numerically calculated impedance (as is the case in homogeneous materials). Empirically, a non-zero difference in impedance is observed between two metamaterial conglomerates of varying thickness. It is therefore suggested to find the effective boundary that minimizes that difference.

Impedance is, however a complex function of the frequency of the incident wave, and as such, the value of the difference between two complex impedances is ambiguous. Chen *et al.* [11] have suggested minimizing the sum of the scaled absolute differences of the complex impedances over all frequencies of interest:

$$x_{\text{eff}} = \arg\min_{x} \sum_{f_i} \frac{\left|z_1(f_i,x) - z_2(f_i,x)\right|}{\max\left[\left|z_1(f_i,x)\right|, \left|z_2(f_i,x)\right|\right]} \tag{4.12}$$

Here, x is the possible effective boundaries, and $z_{1,2}$ are the impedances calculated from two conglomereates thick by a different amount of unit cells.

Hsieh *et al.* [24] have suggested an additional requirements, based on a rearrangement of the components of the complex impedance:

$$x_{\text{eff}} = \arg\min_{x} \sum_{f_i} \frac{\left|\left|z_1(f_i,x)\right| - \left|z_2(f_i,x)\right|\right|}{\max\left[\left|z_1(f_i,x)\right|, \left|z_2(f_i,x)\right|\right]} + \frac{\left|\arg\left[z_1(f_i,x)\right] - \arg\left[z_2(f_i,x)\right]\right|}{\max\left\{\left|\arg\left[z_1(f_i,x)\right]\right|, \left|\arg\left[z_2(f_i,x)\right]\right|\right\}} \tag{4.13}$$

$$x_{\text{eff}} = \arg\min_{x} \sum_{f_i} \frac{\left|\text{Re}\left[z_1(f_i,x) - z_2(f_i,x)\right]\right|}{\max\left\{\left|\text{Re}\left[z_1(f_i,x)\right]\right|, \left|\text{Re}\left[z_2(f_i,x)\right]\right|\right\}} + \frac{\left|\text{Im}\left[z_1(f_i,x) - z_2(f_i,x)\right]\right|}{\max\left\{\left|\text{Im}\left[z_1(f_i,x)\right]\right|, \left|\text{Im}\left[z_2(f_i,x)\right]\right|\right\}} \tag{4.14}$$

Considering a unit cell of a metamaterial with initially hypothesized thickness d, Hsieh's algorithm prescribes of exploring a range of effective boundary shift $L1$ and $L2$ such that the metamaterial's effective thickness be $d_{\text{eff}} = d + L1a + L2a$. Notice how the variables $L1$ and $L2$ are signed: negative values lead to an effective thickness smaller than the one initially hypothesized.

One can then compute the values of the impedances of a 1-unit-cell-thick metamaterial layer and a 2-unit-cell-thick layer using the expression of the impedance calculated from the effective ABCD matrix [24]:

$$z_{\text{eff}} = \pm j\sqrt{\frac{-j(S_{11}^2 - S_{21}^2 - 1)\sigma(L) + (S_{11}^2 - S_{21}^2 + 1)\gamma_1(L) + 2S_{11}\gamma_2(L)}{j(S_{11}^2 - S_{21}^2 - 1)\sigma(L) + (-S_{11}^2 + S_{21}^2 - 1)\gamma_1(L) + 2S_{11}\gamma_2(L)}} \tag{4.15}$$

with the accesory functions $\sigma(L) = \sin\left[k_0(L1 + L2 + d)\right]$, $\gamma_1(L) = \cos\left[k_0(L1 + L2 + d)\right]$ and $\gamma_2(L) = \cos\left[k_0(L1 - L2)\right]$. One should be mindful to replace d by $2d$ when computing the effective impedance of the 2-unit-cell-thick layer.

Once the $(L1, L2)$ space has been explored, the values leading to a minimum mismatch in impedance can be retrieved and the effective thickness be used in the NRW algorithm.

4.5 Example: analysis of the fishnet

We take the example of the fishnet described in Section 3.2 in order to demonstrate the application of the NRW algorithm and the boundary retrieval algorithm.

The software we use for the simulation of the fishnet, CST Microwave, allows to export the magnitude and phase of the S-parameters of the simulation as tables listing these values for each increment of the frequency spectrum over which the simulation is undertaken.

4.5.1 Hsieh's boundary retrieval algorithm applied to the fishnet

Hsieh's boundary retrieval algorithm was coded in Python to process the S-parameters files produced by CST Microwave and return a schematic of the two cost functions (Eq. 4.13, 4.14) and .csv files of the numerical values of these cost functions as functions of the effective boundary shifts.

Initially, the unit cell was conservatively set with a thickness $v = 30\mu m$, leaving a large layer of air before and after the fishnet. Computation of the effective boundary using Hsieh's algorithm led to the results presented in Fig. 4.1.

The two cost functions hold consistent results, indicating that the effective boundaries of the fishnet are situated at $L1 = L2 = -5.35\mu m$ for the both cost functions. The effective thickness of the fishnet under study is therefore $v_{\text{eff}} = 19.3\mu m$.

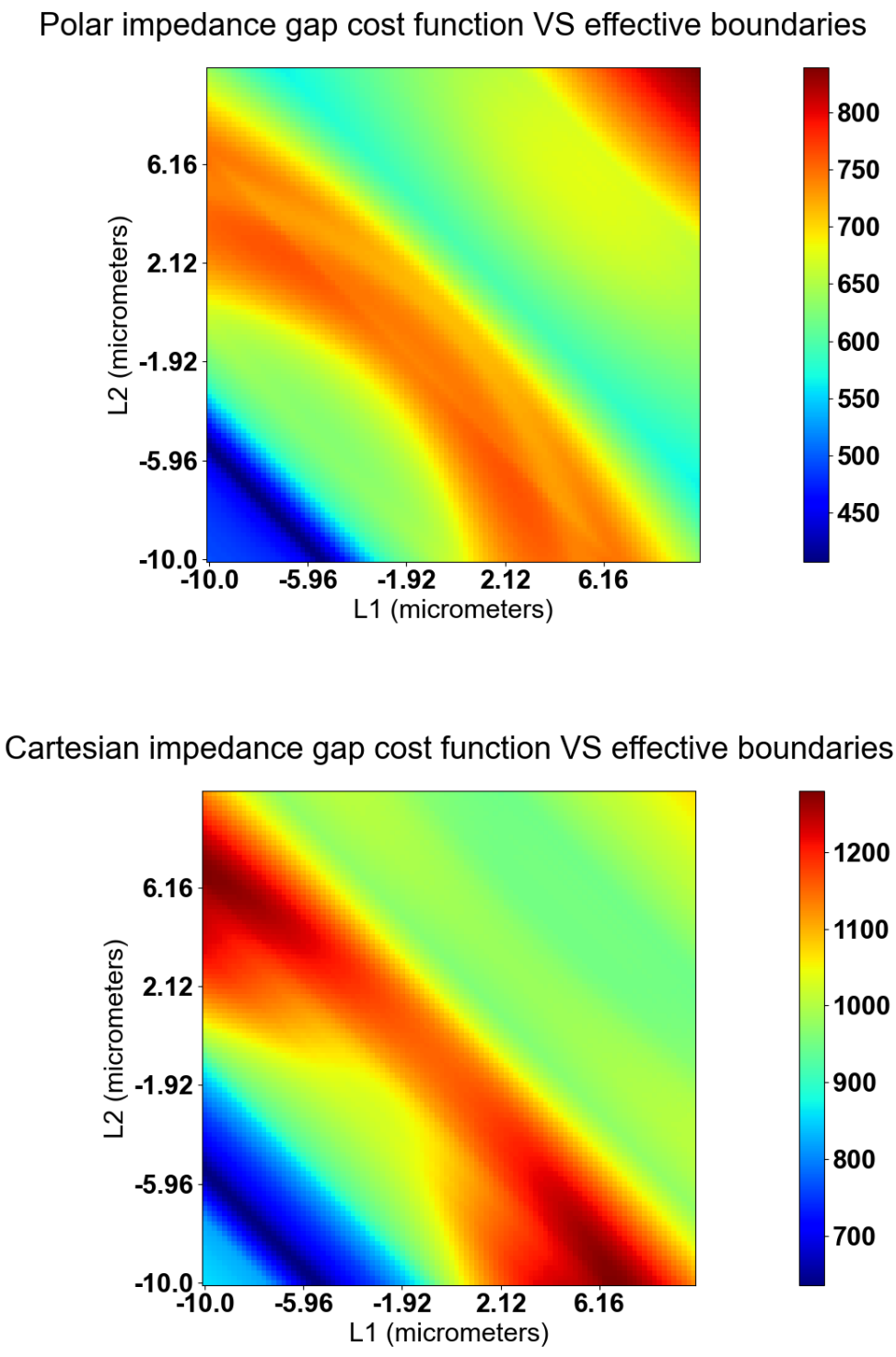

Figure 4.1: Value of cost functions (Eq. 4.13, 4.14; respectively, top and bottom) as functions of effective boundary displacement $L1$ and $L2$, for $v = 30\mu m$. A minimum is observed at $L1 = L2 = -5.35\mu m$.

4.5.2 NRW algorithm applied to the fishnet

The NRW algorithm was coded in Python to process the S-parameters files mentioned in the previous paragraph and return a file listing, over the same frequency increments, the complex values of the effective permittivity, permeability, impedance, refractive index and FOM based on the S-parameters input. The program takes several parameters in consideration, including the simulated fishnet's thickness and the effective boundary shifts. The effective parameters are presented in Fig. 4.2 and 4.3.

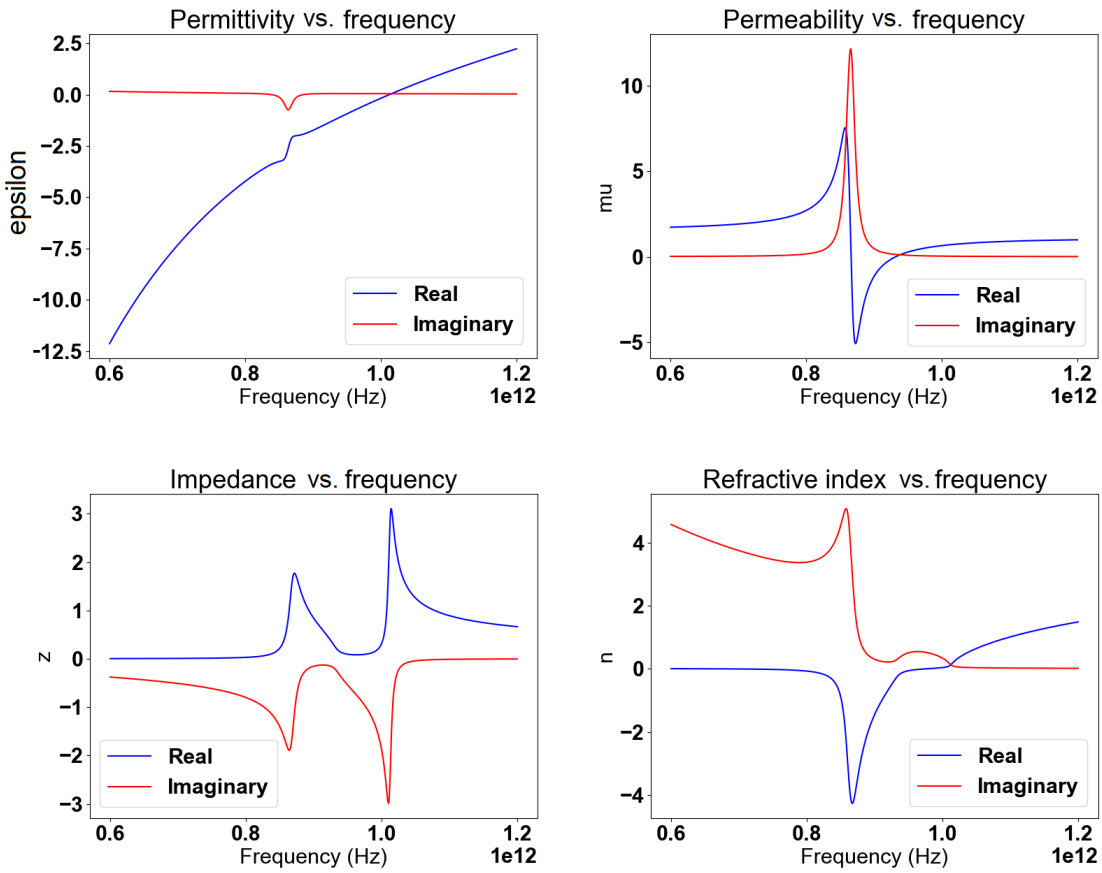

Figure 4.2: Effective parameters of the fishnet described in Section 3.2, numerically computed by application of the NRW algorithm based on S-parameters generated by simulation.

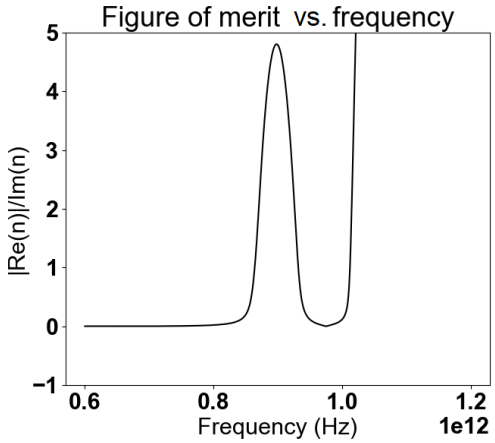

Figure 4.3: Figure of merit of the fishnet described in Section 3.2, numerically computed by application of the NRW algorithm based on S-parameters generated by simulation. The y-axis span has been scaled to emphasize the FOM at frequencies of negative refraction; the skyrocketting FOM past 1.0THz corresponds to frequencies of positive refraction.

Magnetic resonance is observed in the window 0.87-0.93THz, with permeability reaching a minimum of -5.09 at 0.87THz. Plasma frequency of this fishnet is found to be 1.01THz, much above that of magnetic resonance, leading to the whole spectral window of that magnetic resonance to be the span of frequencies where the fishnet has both negative permittivity and negative permeability. This is confirmed by observation of negative refractive index, which reaches a minimum of -4.27 at frequency 0.87THz. As described in Section 4.2.2, negative imaginary permeability, although apparently violating assumption of passivity, is observed around magnetic resonance. In the region of negative refraction, FOM reaches a value of 4.8 at frequency 0.90THz, corresponding to a refractive index of -1.54. Two peaks of impedance are observed, corresponding to the spectral window of negative refraction and the window of positive refraction starting at 0.98THz.

4.6 Conclusion

In this chapter we have presented two methods used in the retrieval of effective parameters of metamaterials: the NRW method and the effective boundary retrieval method. For the

former, we presented the requirements for applicability of this method: homogeneity and passivity. We then explicited the mathematical formalism of this method. Finally, we presented two variations of the effective parameters retrieval method: the Chen method, and the Hsieh method. We concluded by an application of these methods to the fishnet described in the previous chapter.

Chapter 5

THE BD DESIGN

In this chapter, we propose a modification to the negative-refractive index fishnet design and demonstrate numerically that this modification leads to an even lower refractive index resonance peak and higher gains compared to the fishnet design, this effect being sustained for design dimensions ranging from the nanometer up to the milimeter and for various materials. This modification, called "bd design", consists in a shift of the metallic arms to the extremities of the metallic slab, the structure remaining otherwise identical. We discuss the numerical comparison between the use of the fishnet design and the bd design, simulating three fishnet-based metamaterials presented in the literature and showing how a modification of these metamaterials to the bd design leads to improved performances. Finally, we present an explanation for the superior characteristics of the bd design.

5.1 Introduction

The fishnet design (Fig. 5.1(a)), investigated in details in chapter 3, has served for basis to more complex designs [28] with improved performances, such as lower loss, isotropy or lower refractive index. One of such improved designs is the so-called modified fishnet design (Fig. 5.1(b)), which has been used in a variety of scales and materials to create NIMs operating at various frequencies[14, 88, 15].

The bd design we propose in this chapter is a modification of this modified fishnet design. Instead of having the metallic wires crossing the metallic slabs at their center, we place those wires at the extremity of the slab, in a rotational symmetry fashion (Fig. 5.1 (c)), conserving otherwise all dimensions and materials of the originally suggested fishnet. As will be shown in the following sections, such a modification will have positive effects on both the frequency

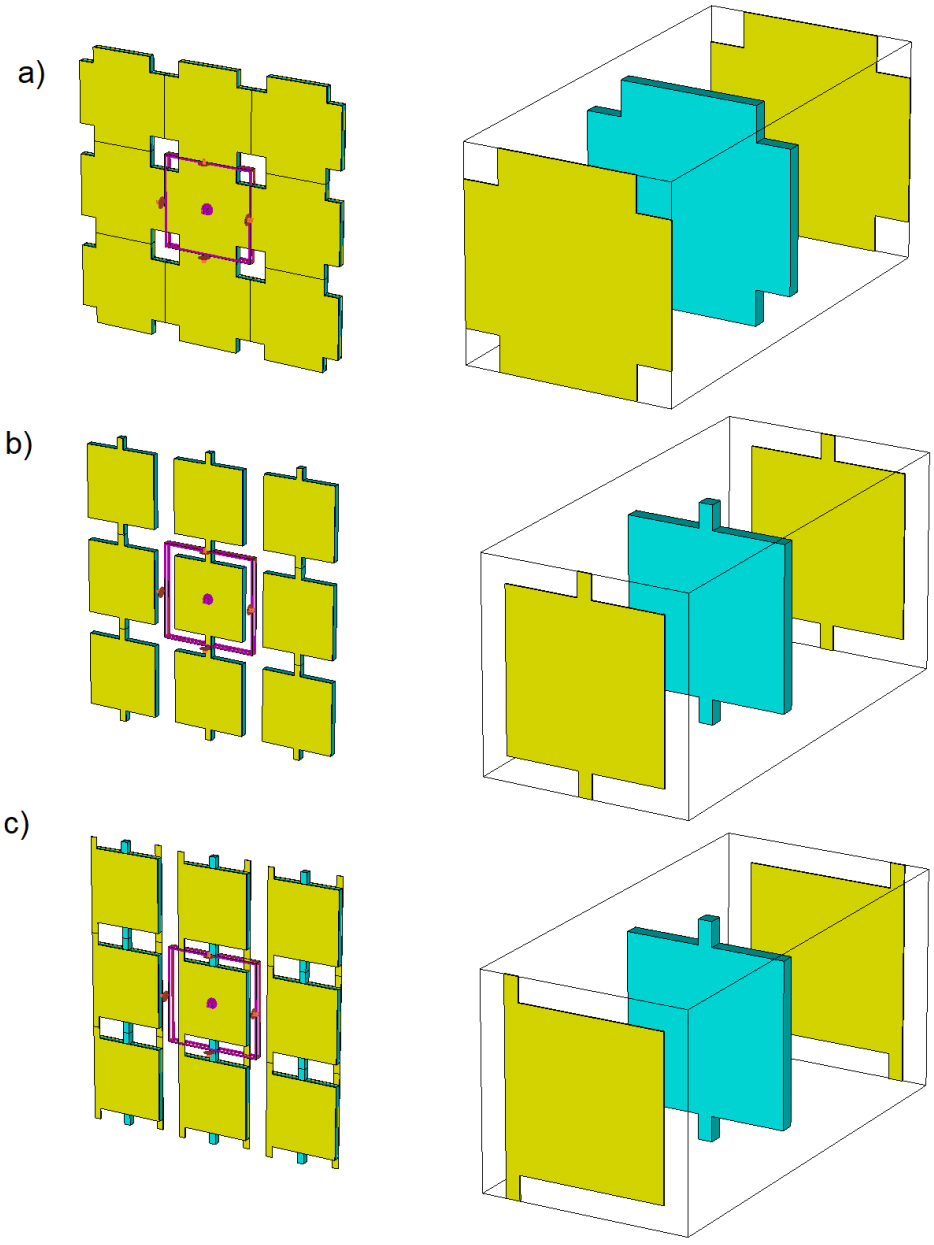

Figure 5.1: Three versions of the fishnet. From top to bottom, showing an array of 9 contiguous unit cells (the central unit cell being delimited in purple) and an exploded view of: (a) the original fishnet design; (b) the modified fishnet design; (c) the bd design.

span where negative refraction occurs, the resonant refractive index minimum as well as the gain of the material.

5.2 Numerical analysis

We compared the refractive indexes and FOMs of three variations of the NIM based on the modified fishnet design and their corresponding bd design modification. We chose the following three designs in literature: Zhang *et al.*'s original fishnet design [88], Kafesaki *et al.*'s modified fishnet [28], and Ding *et al.*'s fishnet structure [14]. These choices allow us to test the bd design over a variety of dimensions (from nanometer to millimeter), materials and resonant frequencies (from GHz to PHz).

Zhang *et al.*'s design consists in two layers of gold sandwiching one layer of undefined dielectric with refractive index of 1.5. We'll use Al_2O_3 as a reference, since it is the material used in the experimental study they reference in their article.

Kafesaki *et al.*'s design is built from two layers of copper and one layer of FR4 dielectric substrate.

Finally, Ding *et al.*'s fishnet structure is made of two layers of gold with, in between, one layer of benzocyclobutene.

As the bd design is more easily related to the modified fishnet suggested by Kafesaki *et al.*, we modify the designs suggested by Zhang *et al.* and Ding *et al.*, adding a space between two adjacent unit cells in the former and losing the isotropy of the latter by removing the

Fishnet	Dimensions (μm)					
	u	v	a	s	m	d
Zhang	0.801	0.11	0.1	0.5	0.03	0.06
Kafesaki	9500	4500	1500	7000	30	1600
Ding	150	30	10	115	0.4	9

Table 5.1: Dimensions of the three fishnets studied.

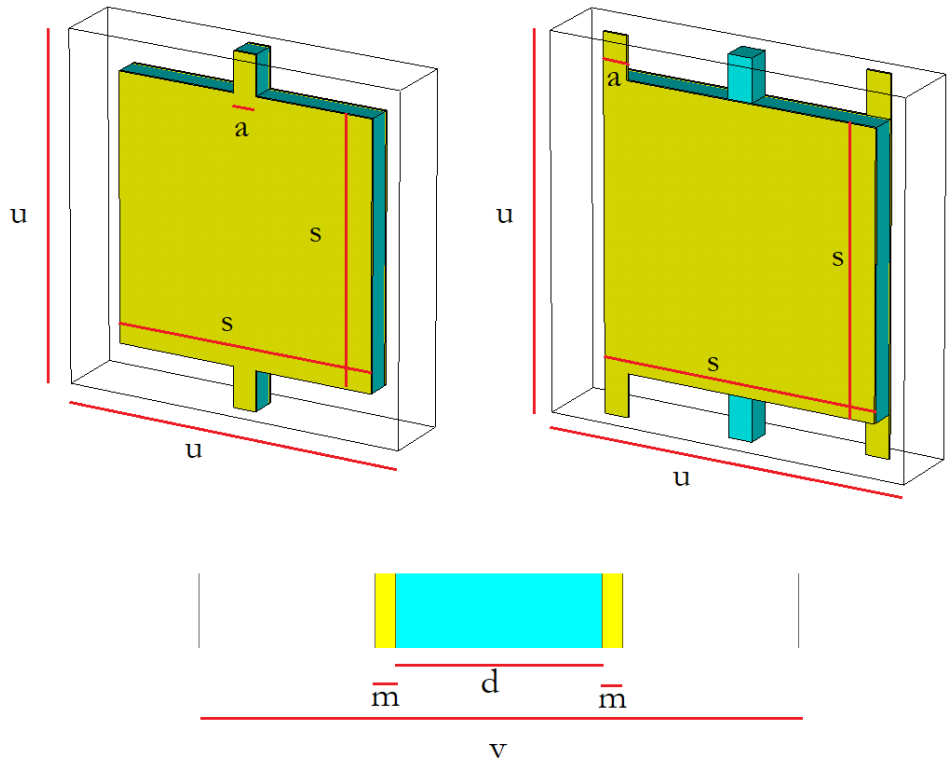

Figure 5.2: Dimension definitions used in Tab. 5.2: u is the side length of the unit cell, s the side length of the metallic and dielectric slab, a the width of the arm, v the thickness of the unit cell, m the thickness of the metal layers and d the thickness of the dielectric layer.

horizontal wires, so as to have uniform comparisons between the modified fishnet and the bd design. Respective dimensions of the three designs are presented in Tab. 5.2, with dimension definitions in Fig. 5.2.

To the exception of the unit cell's width v, all the dimensions are described in the respective articles. In the case of the unit cell's width, this dimension were either unspecified in the article, or inconsistent with Hsieh *et al.*'s unit cell boundary determination procedure introduced in Section 4.4, so that in each case we produced or corrected the unit cell's width using the above procedure. We thereafter noticed small discrepancies between our numerical values and those of the referred articles, as expected since a different value for the effective

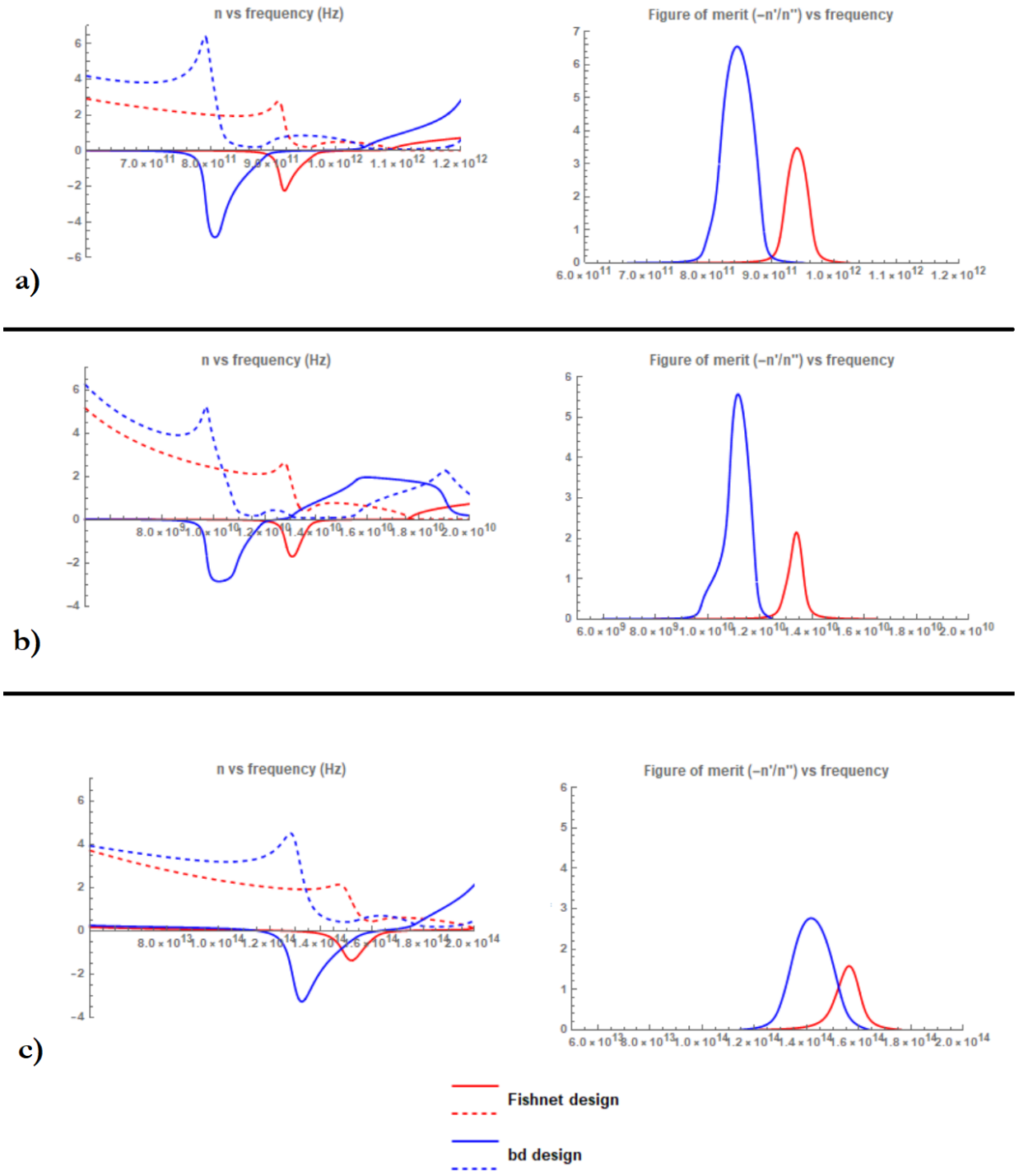

Figure 5.3: Comparison between the effective material parameters of the fishnet design (red) and the bd design (blue). Real parts are indicated by solid lines, imaginary parts by dashed lines. The comparison is done using the dimensions and materials presented by a) Ding, b) Kafesaki and c) Zhang.

Fishnet	Resonant frequency		Min. refractive index		Max. FOM	
	Fishnet	bd	Fishnet	bd	Fishnet	bd
Zhang	151THz	132THz	-1.38	-3.29	1.58	2.74
Kafesaki	13.2GHz	10.8GHz	-1.73	-2.83	1.58	5.52
Ding	0.918THz	0.814THz	-2.25	-4.86	3.47	6.54

Table 5.2: Numerical results of the comparison between the effective material parameters of the fishnet design and bd design.

boundaries of the fishnet could drastically affect the value of the effective refractive index. Still, we were able to retrieve a similar trend in terms of effective parameters between the articles results and ours, so that we can consider the discrepancy between our results and those of the articles to be entirely due to a difference in effective boundary value. Furthermore, this discrepancy between our results of those of the articles matter less than the difference we observe, using the same software, algorithm implementations and material specifications, between the modified fishnet and the bd design.

The numerical values of the S-parameters are retrieved using the commercial software CST Microwave Studio, and from these the NRW algorithm is applied in order to produce the effective refractive index, permeability, permittivity and FOM.

The results are presented in Fig. 5.3. The effective parameters for the fishnet design are drawn in Fig. 5.3 in red, those for the bd design in blue. The real values are represented by solid lines, the imaginary values in dashed lines.

In all of the examined design we observe a recession of the resonant frequency of about 10%. The refractive minimum index becomes lower by approximately a factor of two, while the FOM is itself multiplied by two, meaning a corresponding increase of gain. The numerical results are summed up in Tab. 5.2.

5.3 Mechanisms behind the improved performances

The mechanisms behind the improved performances of the bd design can be explained by considering the impact of the change in structure on the magnetic resonance within the dielectric layer. We will also consider the impact on the the negative permittivity mechanism, as the related component of the fishnet, *i.e.* the array of metallic wires, is the sole modification that separates the fishnet from the bd design.

5.3.1 Magnetic resonance within the dielectric layer

Fig. 5.4 shows a comparison of the surface currents on the front and back face of one unit cell of fishnet at resonance frequency in the fishnet design and the bd design. As described by Kafesaki *et al.*, we observe a combination of two current modes, in which the current flows in both faces either in the same topological direction or in opposite topological direction. The first mode is associated with the plasma-like behavior of the metallic wires array, the second with the magnetic resonance in the dielectric layer. The combination of these modes lead to a periodic accumulation and depletion of charges in two precise areas of the metallic surface.

In the fishnet design, the strongest surface currents are observed in the metallic arms part of the structure. In contrast, the bd design shows a maximum current happening on the side of the metallic slab opposed to the metallic arm. This is an important change, as the strongest surface currents lead to the strongest magnetic currents within the dielectric. Since those surface currents are closer to the dielectric slab, we expect a magnetic resonance of larger amplitude in the case of the bd design, which is clearly observed in part c) of Fig. 4. In addition, we notice that this reduction of intensity in the arm's surface currents leads to a reduction of the magnetic field in the dielectric layer's arms, which, running counter to the resonant magnetic field, hinders the latter. This allows, in the case of the bd design, a larger area where the magnetic resonance occurs.

The idea that the bd design experiences a stronger magnetic resonance than the fishnet

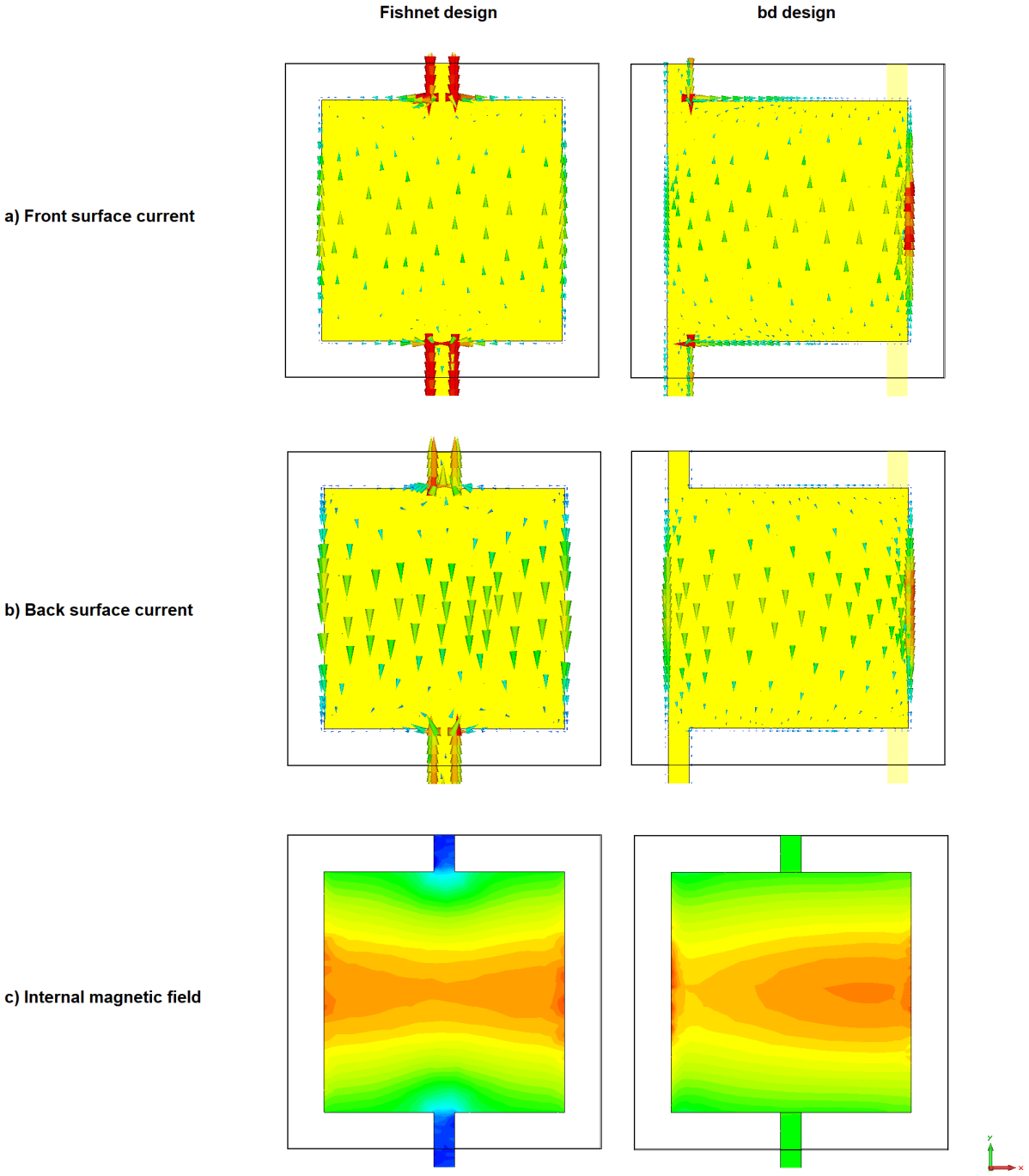

Figure 5.4: Electromagnetic response measured in the metamaterial described by Ding *et al.* using the fishnet and the bd design. a) and b): Front and back surface current (arbitrary units). c) Magnetic field (arbitrary unit) in the dielectric layer.

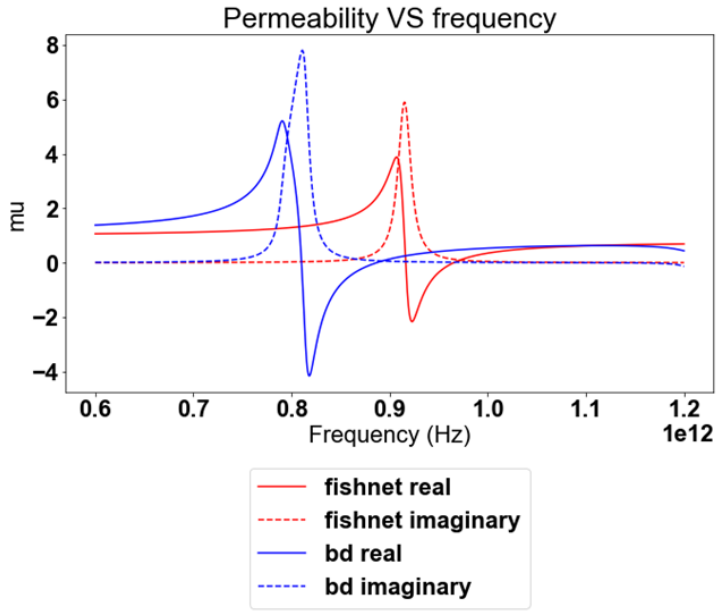

Figure 5.5: Comparison of numerically retrieved complex permeabilities of the fishnet design (red) and bd design (blue) for dimensions specified by Ding *et al.*.

can be verified by comparing the two metamaterials permability spectrum. This is done in Fig. 5.5 for the dimensions of Ding *et al*'s fishnet. Passing from the fishnet to the bd design, a downshift in resonance frequency is observed, confirming previous comparisons of the refractive index in either case. Additionally, the magnitude of the permability is greater in the bd design than in the fishnet, for both real and imaginary parts, and for both positive and negative values. This is a strong indicator that the effect of magnetic resonance is greater in the bd design as in the fishnet, confirming the previous observations of surface currents and internal magnetic field magnitude.

5.3.2 Electric resonance through the metallic wires

Another possible cause we considered for the increased performances of the bd design was the metallic wire arrays component of this design. As a reminder, this part of the fishnet design is responsible for the electric resonance and negative permeability of the fishnet. Pendry *et*

al. originally demonstrated how a square array of wires leads to a plasma-like behavior [50]. In their investigation Pendry *et al.* mention how the exact geometry of the array does not matter for the plasmonic behavior to occur; indeed, the original fishnet material is composed not of metallic wires per se but of metallic bands, arranged what is more into a rectangular array instead of a square one.

One could question, however, what happens when a lateral translation is applied to the geometry of the metallic array described by Pendry *et al.*, the same translation that leads to the transformation from the fishnet design to the bd design.

In Fig. 5.6 we show the difference of numerically retrieved real permittivity between an array with wires arranged face-to-face and an array with wires shifted from one another. This figure shows how shifting the wires pushes the resonant frequency of the plasmon to higher frequencies, leading, for a given plasmonic frequency, to a lower negative permittivity. This lower negative permittivity could contribute to the reduced negative refractive index in the bd design.

However, as explained in Section 2.5, it is naive to assume that the fishnet's metaproperties emerge by straight inheritance of the properties of its components. Rather, the fishnet is an exceptional case in which the mechanisms giving rise to negative permittivity and negative permeability coexist while interfering only minimally with each other. In the present case, this can be illustrated by comparing the numerically calculated permittivity of the fishnet and the bd design. While, when considering the wires alone, the plasma frequency shifts upward when passing from a square array to a diamond array (Fig. 5.6), when considering the metamaterial as a whole, we actually observe a *downshift* in plasma frequency (Fig. 5.7). It is worth noting, however, that the bd design's permittivity changes much faster as a function of the frequency than the fishnet's permittivity, hinting at an effect of the arm's translation on the negative permittivity mechanism. Further research is therefore warranted to investigate the bd design's permittivity.

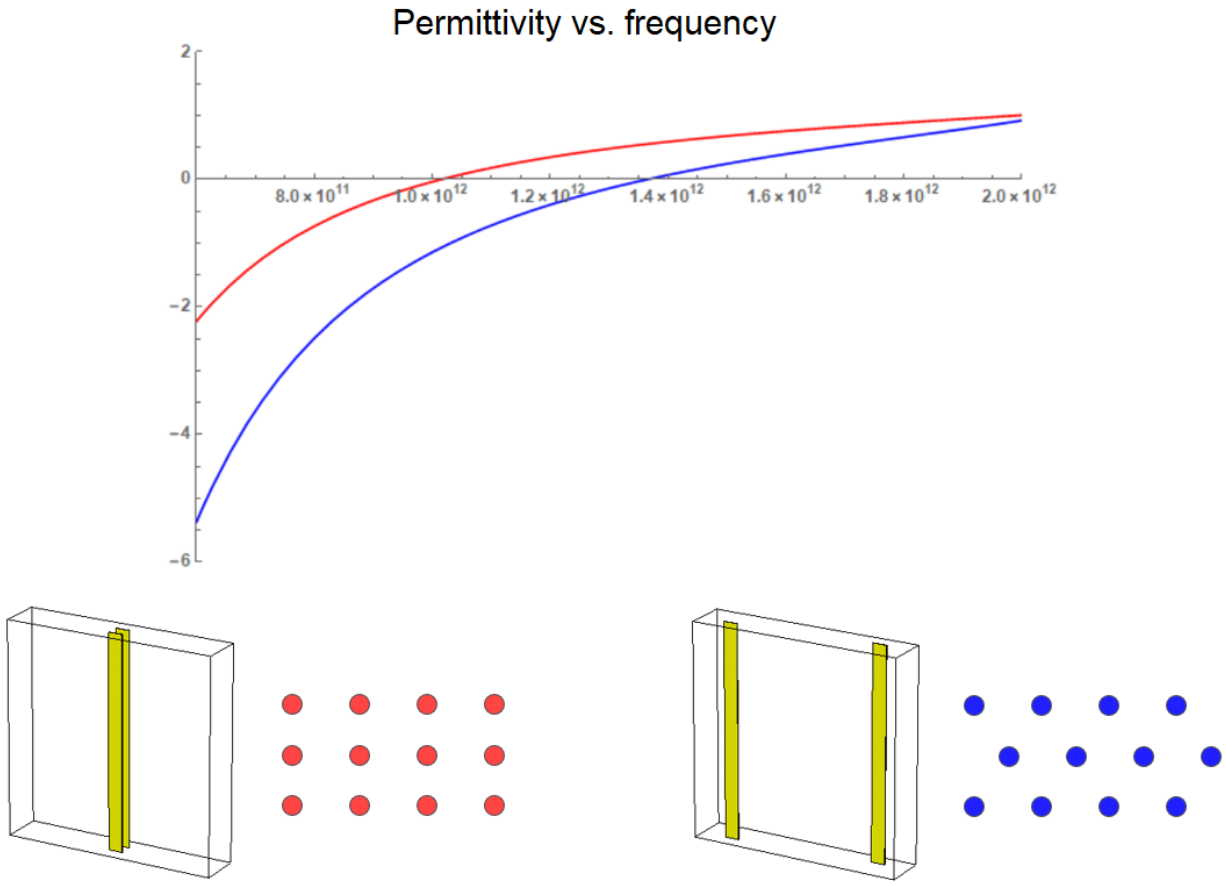

Figure 5.6: Comparison of numerically retrieved real part of the permittivity between face-to-face wire arrangement (red) and laterally shifted wire arrangement (blue). Diagrams of the arrangement for each configuration is explicited at the bottom.

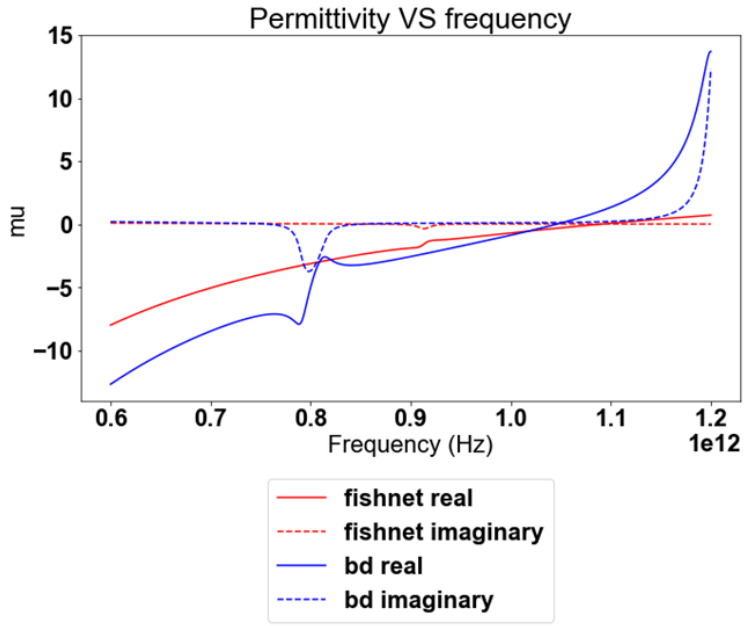

Figure 5.7: Comparison of numerically retrieved complex permittivities of the fishnet design (red) and bd design (blue) for dimensions specified by Ding *et al.*.

5.4 Conclusion

In this chapter we have presented a novel general design of metamaterial termed the bd design, adapted from the fishnet structure.

Numerical simulations show the bd design demonstrates lower loss (lower FOM), lower refractive index and negative refraction over a larger span of frequencies than that of the fishnet design. Improved performances are determined to be due to a larger portion of the dielectric made able to take part in magnetic resonance. Different plasma-like dynamic from the wires could have an effect, but while wire structure alone sees a plasma frequency shift to higher frequencies, the bd design as a whole results in a lower plasma frequency than the fishnet. Considering both the negative permeability and negative permittivity effects are impacted by the modifications on the fishnet design resulting in the bd design, further research is expected to investigate the impact of those modifications on the interference

between the mechanisms leading to the emergence of, respectively, negative permittivity and negative permeability. Further research is also expected to investigate in more depth the impact of the arm's translational shift on the dynamics of emergence of the negative permittivity.

Chapter 6

THREE CASES OF DISCONTINUOUS REFRACTIVE INDEX

In this chapter we investigate what appears to be an anomaly of the effective parameter retrieval process presented in Chapter 4: the discontinuity of the refractive index in some materials. We will first consider three designs presented in the literature, presenting their characteristic in details. We will then offer an alternative way to measure the refractive index of metamaterials, and suggest a possible explanation for the emergence of the discontinuity.

6.1 Introduction

We have identified three designs reported in the literature which present discontinuous refractive index.

6.1.1 Chan et al.*'s arrays of upright split-ring pairs*

Chan *et al.* [8] proposed a metamaterial operating in near-infrared frequency, consisting in split-ring pairs arranged back to back. The split-ring pair is made of gold (Drude permittivity of $\epsilon = 9 - \frac{\omega_p^2}{\omega(\omega+i\Gamma)}$ with $\omega_p = 1.37 \times 10^{16}$Hz and $\Gamma = 1.0027 \times 10^{14}$Hz), while the encasing unit cell is in glass (n=1.458; in our own simulations we will consider this to be fused quartz, as it fits the definition of glass and its refractive index matches that indicated by Chan *et al.* at near-infrared frequency [59]). A unit cell is represented in Fig. 6.1. Dimensions are as follows: $L_x = L_y = 200$nm, $L_z = 300$nm, W_1 =40 nm, W_2 =60 nm, H_1 =50 nm, H_2 =40 nm, D =50 nm, and δ =30 nm.

Chan *et al.* report a negative refractive index achieved between wavelengths of 1.008μm and 1.260μm (238 to 297THz). Our own simulation, based on Chan *et al.*'s parameters, conforms in Chan *et al.*'s response spectral profile, albeit differing by the span of frequency

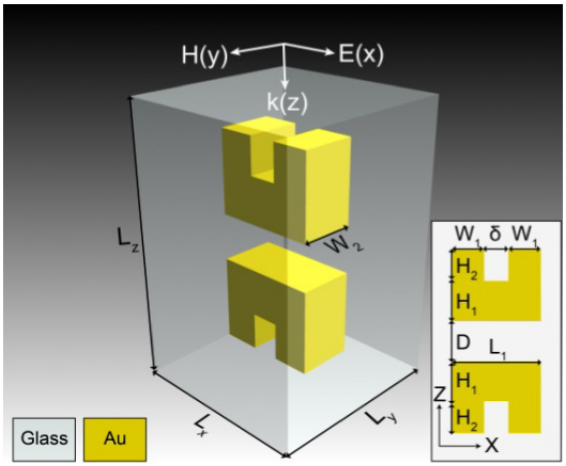

Figure 6.1: Unit cell of Chan *et al.*'s upright split-ring pair metamaterial. Dimensions are as follows: $L_x = L_y = 200$nm, $L_z = 300$nm, W_1 =40 nm, W_2 =60 nm, H_1 =50 nm, H_2 =40 nm, D =50 nm, and δ =30 nm. Reproduced from [8].

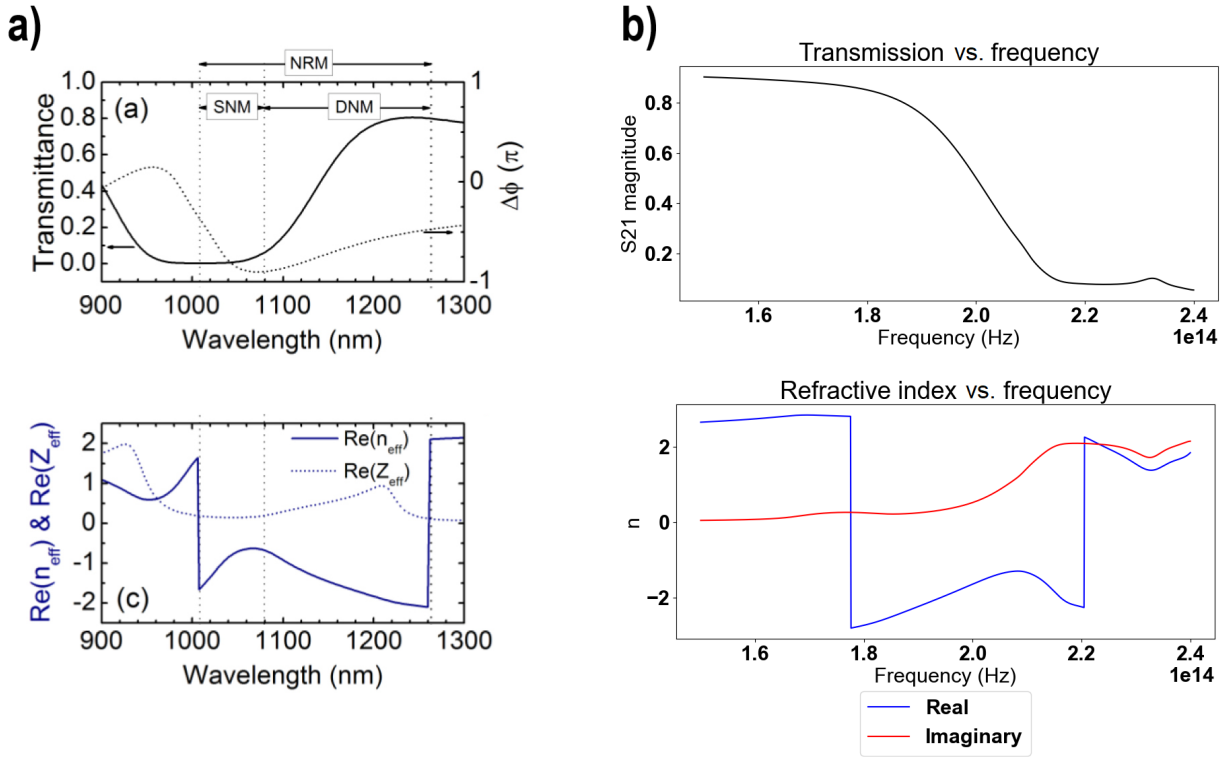

Figure 6.2: Comparison between Chan *et al.*'s simulation results (a), reproduced from [8]) of the upright split-ring pair metamaterial and our own results (b)).

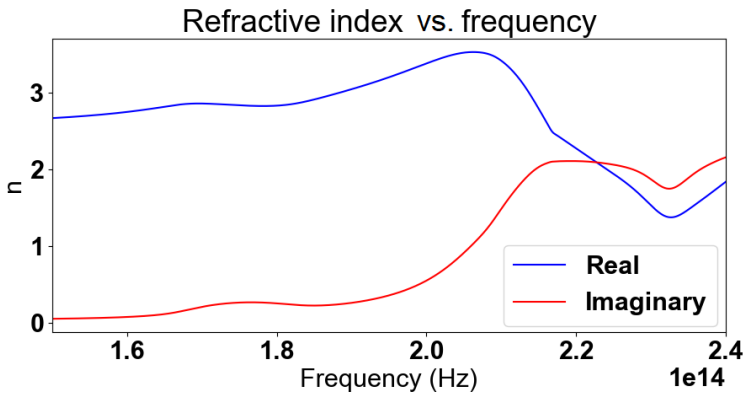

Figure 6.3: Numerically calculated refractive index of Chan *et al.*'s metamaterial after correction of the discontinuity.

over which negative refraction is observed: we observe negative refraction from 177THz to 220THz. The result can be observed in Fig. 6.2. This resonance shift might be a result of the assumption of fused quartz as glass material presented in the previous paragraph, or other parametric differences between our simulation and that of Chan *et al.*.

Chan *et al.* demonstrate the negative refraction of their material by both analysis of the S-parameters using the effective parameter retrieval method, by geometrical analysis of the incident rays and by analysis of the dispersion relation of their material. Nowhere in their report do they, however, mention the refractive index jump that occurs at 238THz (from positive to negative value) and 297THz (back from negative to positive value).

Chan *et al.*'s results are the only one among the three we will discuss in this chapter where continuity *can* be enforced: refraining from changing the m-branch index of Eq. 4.11 at the frequencies of discontinuity would make the retrieved refractive index continuous across the spectrum of frequencies we're considering here. We chose to disregard this change in m-branch index in Fig. 6.2 to make the similarity of our numerical simulation to that of Chan *et al.*'s apparent. When the NRW algorithm is thoroughly applied and continuity of the refractive index is enforced, the refractive index becomes as represented in Fig. 6.3, and is positive for all frequency values of the considered spectrum.

6.1.2 Du et al.*'s fishnet three-dimensional metamaterial*

Du *et al.* [17] proposed a metamaterial operating at low terahertz frequency. Their design consists in a refinement of the isotropic fishnet design [14] where the central slab is reshaped into a cross (see Fig. 6.4). As for the original fishnet, the structure is made of layers of gold (Drude model with plasma frequency $\omega_p = 1.367 \times 10^{16}$Hz and collision frequency $\gamma = 4.084 \times 10^{13}$Hz) shaped into a cross design. Instead of sandwiching a dielectric layer, however, these metallic layers lie within a unit cell that is entirely filled by the dielectric, chosen to be gallium arsenide (GaAs). Dimensions of the unit cell are as follows: $a_x = a_y = 90\mu$m, $a_z = 62\mu$m, $l_p = 81\mu$m, $w_p = 41\mu_m$ and $w_n = 12\mu$m.

Du *et al.* report negative refraction in the range 0.72 to 0.97THz (Fig. 6.5 a)). While the results of our simulation are in good agreement with Du *et al.*'s when comparing the S-parameters on Fig. 6.5, the application of the effective parameter retrieval procedure holds seemingly very different results: our application of the procedure leads to a negative refraction appearing only starting at 0.92THz. A closer inspection reveals however that this is only due to the refractive index jump from positive to negative values, which occurs at an earlier frequency in Du *et al.*'s analysis. This discrepancy notwithstanding, the profile of the

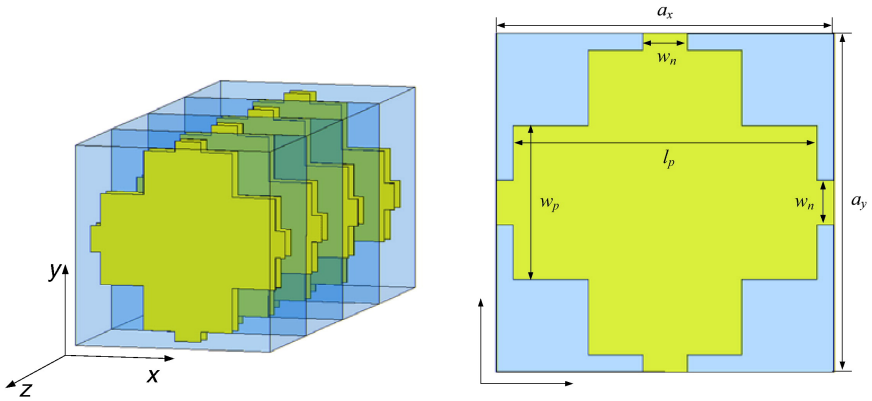

Figure 6.4: Du *et al.*'s fishnet three-dimensional metamaterial. Dimensions are as follows: $a_x = a_y = 90\mu$m, $a_z = 62\mu$m, $l_p = 81\mu$m, $w_p = 41\mu_m$ and $w_n = 12\mu$m. Reproduced from [17].

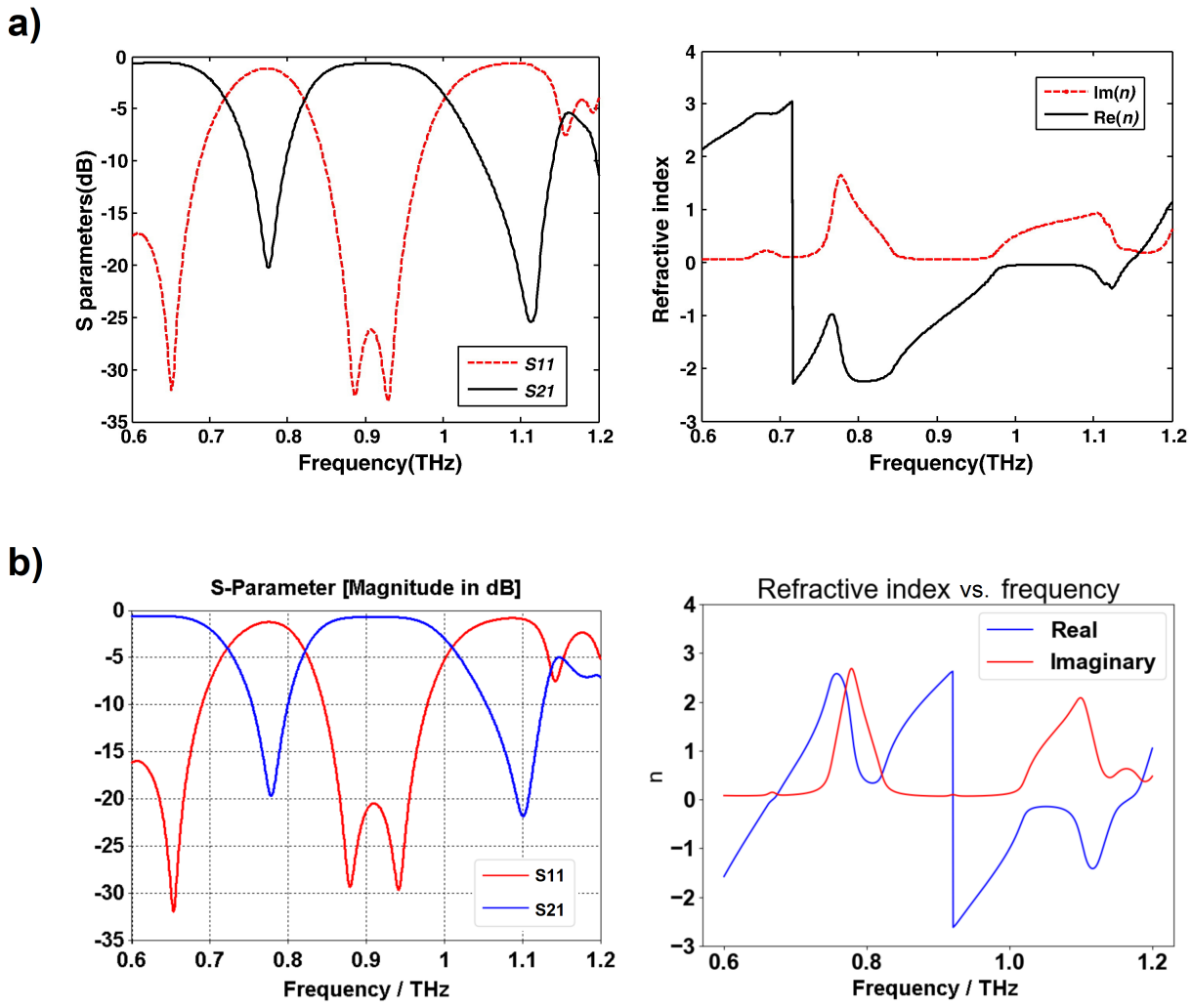

Figure 6.5: Comparison between Du *et al.*'s simulation results (a), reproduced from [17]) of the fishnet three-dimensional metamaterial and our own results (b)).

refractive index is very similar if one ignores the discontinuity and only considers the rate of change of the refractive index with respect to the frequency: this rate of change is positive from 0.6THz to 0.76THz, reaches a zero (refractive index local maximum) at 0.76THz, then turns negative until reaching another zero (refractive index local minimum) at 0.81THz, and then being positive again. This discrepancy in results highlights the importance of the phenomenon of refractive index discontinuity: Du *et al.* is able to report a window of negative refraction about five times greater than that one would conclude from our own results. No acknowledgment is made of the refractive index discontinuity.

6.1.3 Paul et al.*'s bulk metamaterial*

Paul *et al.* [49] present a fishnet-like, cross-shaped metamaterial operating at low terahertz frequency. This design is similar to Du *et al.*'s, save for the presence of arms, which interestingly makes it the only "disconnected" fishnet considered in this thesis (see Fig. 6.6). The metallic layers are set to be copper, with Drude permittivity (the Drude characteristic of copper at terahertz frequencies are not specified in Paul *et al.*'s report; for our own simulation we set those characteristics to $\omega_p = 1.914 \times 10^{15}$Hz for the plasma frequency and $\gamma = 8.34 \times 10^{12}$Hz for the collision frequency [47]). Same as with Du *et al.*'s fishnet, the whole

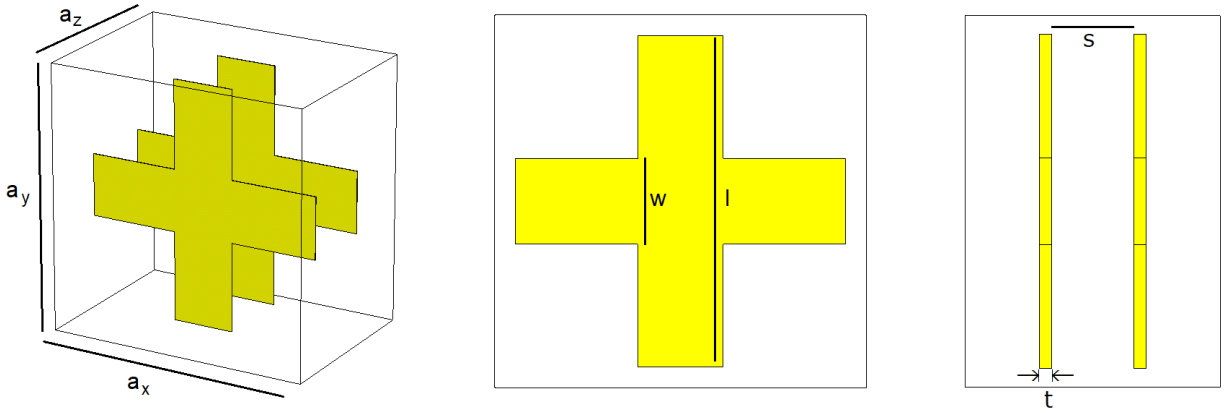

Figure 6.6: Paul *et al.* bulk metamaterial. Dimensions are as follows: $a_x = a_y = 90\mu$m, $a_z = 62\mu$m, $l = 81\mu$m, $w = 21\mu_m$, $s = 9.5\mu$m and $t = 0.2\mu$m.

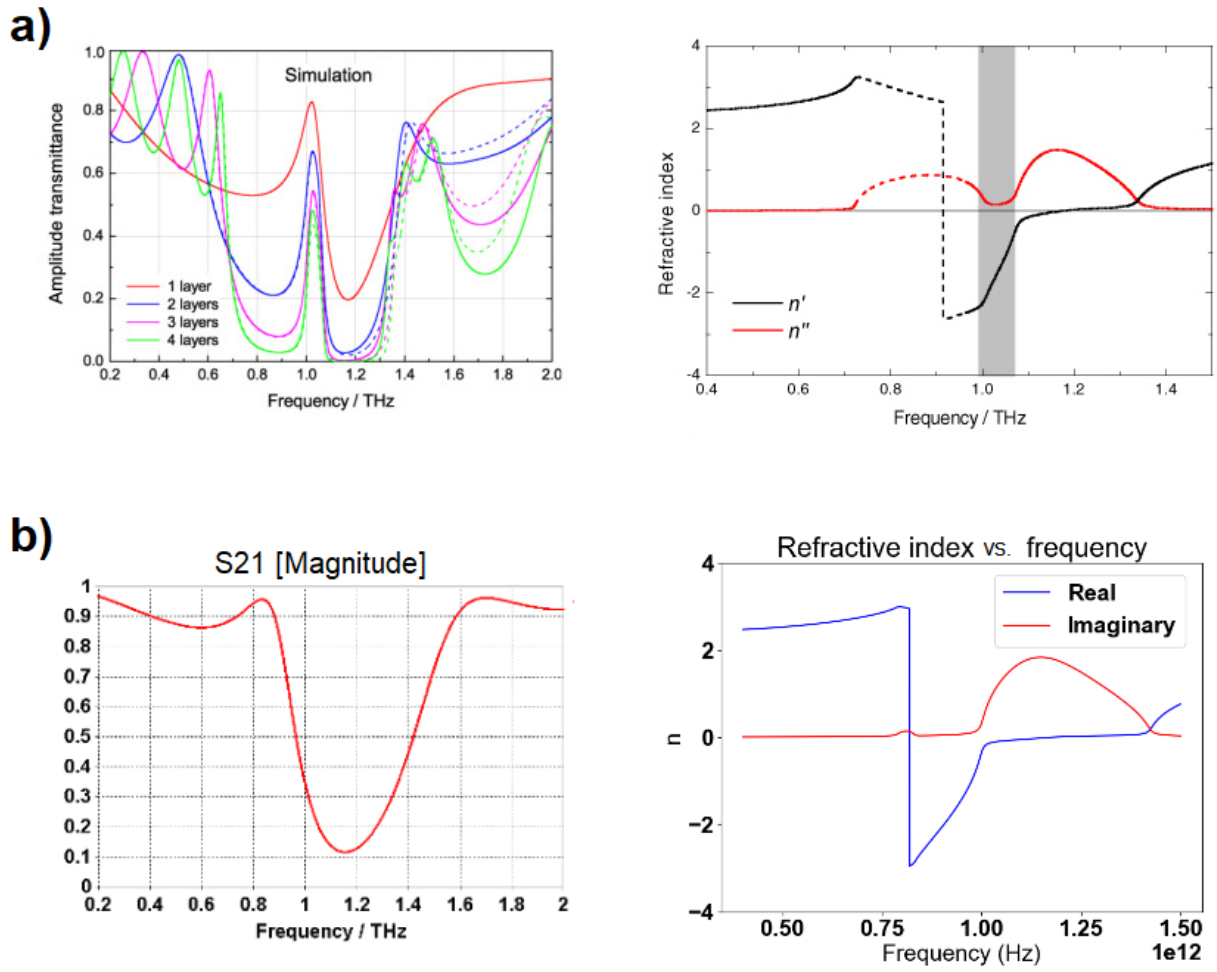

Figure 6.7: Comparison between Paul *et al.*'s simulation results (a), reproduced from [49]) of the bulk metamaterial and our own results (b)).

unit cell is permeated with the dielectric, chosen by Paul *et al.* to be BCB (permittivity of $\varepsilon = 2.67$ and loss parameter $\tan\delta = 0.012$ at frequency of interest).

Paul *et al.* reports negative refraction in the frequency window from 0.96 to 1.17 THz. Our own simulation qualitatively agrees with those results, as can be seen in Fig. 6.7, albeit with a negative refraction starting at the refractive index discontinuity located at 0.82THz. The reason why Paul *et al.* do not measure negative refraction from the discontinuity is as follows: of the three reports we consider in this chapter, Paul *et al.* is the only one to actually acknowledge the discontinuity in their results, stating:

> "The dashed parts of the curves[1] mark the regions where the half-wavelength inside the medium is smaller than the lattice constant a_z and the calculated effective parameters are not expected to be reliable." [49]

6.2 Geometrical study of simulated electromagnetic dynamics as a test for negative refraction

In this section we propose a benchmark that can be used to investigate the negative refraction (or lack thereof) in metamaterials. This benchmark rely on the geometrical ray formalism of electromagnetic waves, using observations of the behavior of those waves as they are transmitted through objects of determined shapes (mainly, a prism), and comparing those observations to what would be epxected should the material be homogeneous and have the claimed refractive index.

The numerical tools at our disposal for the simulation of plane waves as a way to observe the reaction of transmitted waves through the media. This brings a challenge to the analysis of the refractive index using this benchmark: diffraction patterns occur, that, while still allowing an interpretation of the sign of the refractive index, limit the precision of an exact computation of that index. Fortunately, in this analysis we are less concerned by the exact value of the index, than we are about its sign, and the frequency at which the jump from positive to negative refractive index occurs.

---

[1] Observable in Fig. 6.7 a).

The prism configuration is a benchmark that allows to geometrically determine the refractive index of the metamaterial. A 2D prism is numerically designed using unit cells of the metamaterial one wishes to study, and a plane wave is sent onto a surface of the prism. The direction of the transmitted wave allows the determination of the sign of the refractive index of the metamaterial at that wavelength. Typically, the prism is designed so that the interface of incidence of the plane wave is parallel to the wave front, and the prism is elongated enough to contain the principal front of the wave.

A standard prism is depicted in Fig. 6.8. The unit cells (cyan) are stacked in a half-pyramid, creating a prism in the XZ plane. A plane wave (wave fronts depicted in black) polarized in the Y direction and propagating towards the Z direction is incident upon the lower interface of the prism, and emerges refracted from the upper interface of the prism. Direction of refraction indicates the sign of the prism's material refractive index: refraction to the left (blue wave fronts) signifies a negative refractive index, while refraction to the right (red wave fronts) signifies a positive refractive index. The ideal upper interface is pictured in green.

One readily notes a first challenge with this configuration: virtually all metamaterials are constrained by the dimensions of their unit cell, and the development of complex geometrical objects using those metamaterials must take these dimensions into account. For the examples considered in this thesis, it is impossible to design a prism with an upper surface that can be considered nanoscopically or even microscopically planar, and that can therefore match the ideal upper interface; the best one can do is to design staircase-shaped prisms in dimensions such that a negligible amount of scattering occuring due to the local non-uniformities of the upper surface. However, practically speaking this staircase shape does not lead to significant scattering if we constrain the slope by an increment of one unit cell's depth as we move laterally towards the positive X. An example demonstrating this can be found in Fig. 6.9, representing a prism with similar geometry as that of Fig. 6.8, made of $\frac{15(15+1)}{2}$ homogeneous blocs of Teflon with dimensions $150 \times 150 \times 30\mu$m. An electromagnetic wave of frequency 1THz, polarized along the Y axis and propagating towards the posivite Z, is sent upon the

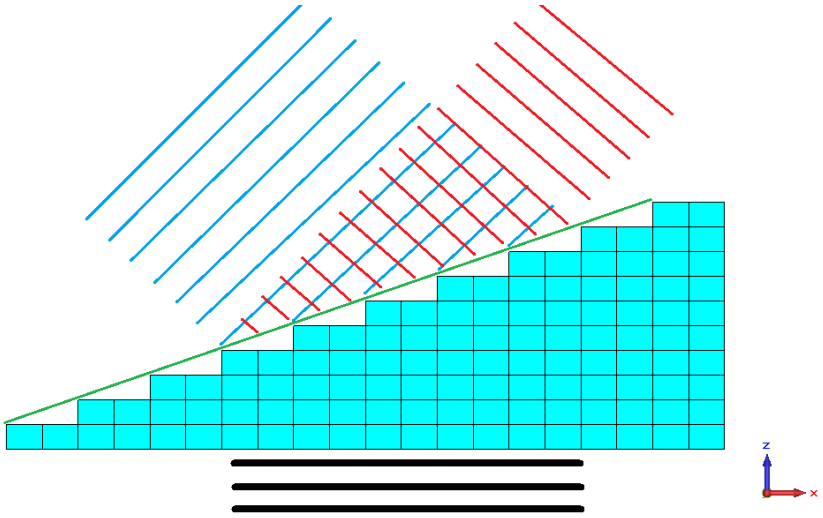

Figure 6.8: Typical simulation set-up for the prism configuration. Incoming plane wave is symbolized by the black lines. Outgoing plane wave positively refracted is symbolized by the red lines, while the negatively refracted plane wave is symbolized by the blue lines. The green line delineates the idealized upper interface.

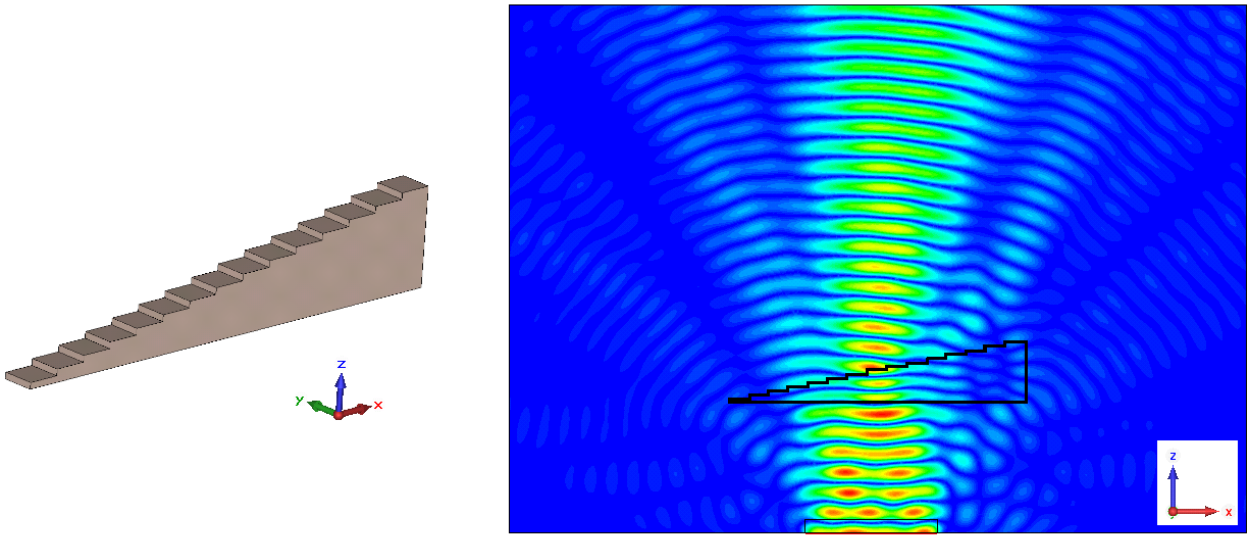

Figure 6.9: Simulation of the refraction of a plane wave by a Teflon prism. On the left: representation of the simulated Teflon prism, made of $\frac{15(15+1)}{2}$ blocs of Teflon with dimensions $150 \times 150 \times 30\mu$m. On the right: XZ plane section of the absolute value of the electric field generated by a plane wave incident upon the lower interface of the prism.

inferior interface of the prism. One clearly distinguishes the main refracted wave leaving the upper interface of the prism towards the right (as expected from a positive refraction), as well as secondary waves of lower intensities refracted right and left of the main wave, due to diffraction effects of the input port.

Analysis of Chan et al.*'s metamaterial*

Fig. 6.10 shows a simulation of a plane wave incident upon a prism made of unit cells of Chan *et al.*'s metamaterial. The absolute value of the electric field is represented within and around the prism (the shape of which is explicited in black for the first frequency).

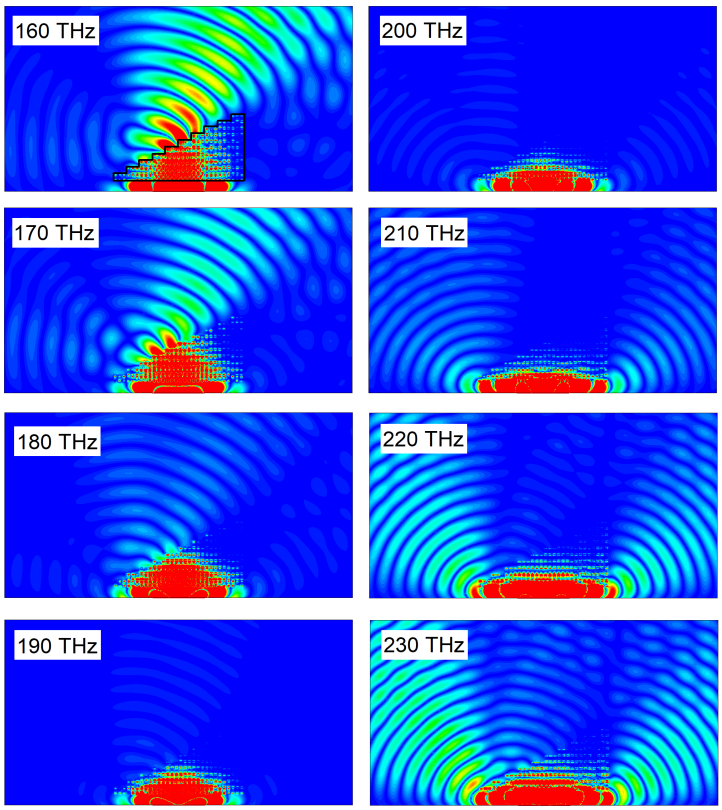

Figure 6.10: Absolute value of the electric field within and around a prism made of Chan *et al.*'s metamaterial for various frequencies when a plane wave is incident upon it, based on a numerical simulation. The shape of the prism is delineated for clarity for the first frequency.

Comparing those results to those obtained by (mis-)use of the NRW algorithm, no negative refraction is observed at frequencies where expected from Fig. 6.2, b). Instead, positive refraction is observed at frequencies 160-180THz. Past those frequencies, transmission drops to levels that prevent any analysis of the refracted plane wave. Between frequencies of 210THz to 230THz, strong reflection, confirmed to happen at those frequencies by numerical simulation of a single unit cell, causes the incident plane wave to "escape" laterally from the lower interface of the prism. These results confort the necessity of enforcing continuity of the refractive index whenever possible. In the last two cases however, discontinuity *has* to occur, as we will show.

Analysis of Du et al.*'s fishnet three-dimensional metamaterial*

Fig. 6.11 shows a simulation of a plane wave incident upon a prism made of unit cells of Du *et al.*'s metamaterial. The absolute value of the electric field is represented within and around the prism.

Positive refraction is observed from 0.6THz to 0.72THz, after which a drop in transmission is observed (and confirmed in the numerical results presented in Fig. 6.5, with a transmission's amplitude under 0.60 in the span 0.73THz to 0.82THz and a minimum of 0.10 reached at frequency 0.78THz), rendering any observation impossible. At 0.86THz transmission rebounds and negative refraction is observed. Enhancement of the electric field observation by rescaling of the color gradient was considered, but because of the high loss of the material only the part of the plane wave that crosses a small thickness of prism emerges from the upper interface, skewing the results (see Fig. 6.12 for an illustration of the effect; the white star is the desired center of the wave emerging from the upper interface, and the black star the observed center). Thus, this analysis does not allow for an exact determination of the frequency at which the refractive index passes from positive to negative, but allows to determine a region of uncertainty.

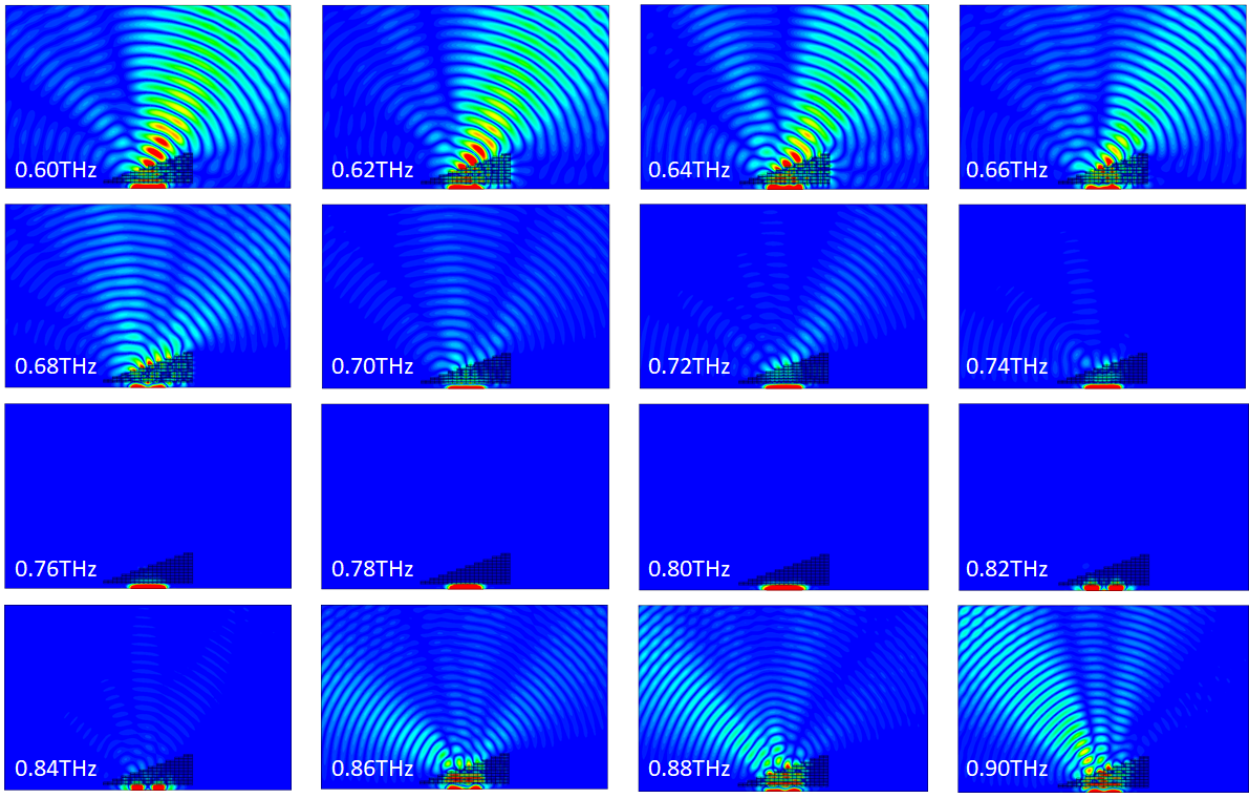

Figure 6.11: Absolute value of the electric field within and around a prism made of Du *et al.*'s metamaterial for various frequencies when a plane wave is incident upon it, based on a numerical simulation.

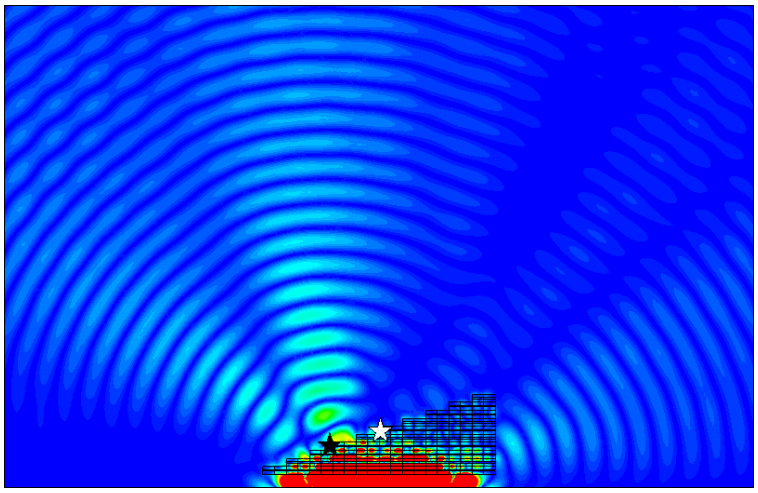

Figure 6.12: Absolute value of the electric field within and around a prism made of Du *et al.*'s metamaterial when a plane wave of frequency 0.8THz is incident upon it, based on a numerical simulation. The white star indicates the center of the expected emerging plane wave, and the black star the position of the actual center of the emerging plane wave.

Analysis of Paul et al.*'s fishnet three-dimensional metamaterial*

Fig. 6.13 shows a simulation of a plane wave incident upon a prism made of unit cells of Paul *et al.*'s metamaterial. The absolute value of the electric field is represented within and around the prism.

Positive refraction is observed from 0.6THz to 0.74THz. Starting 0.86THz, a clear negative refraction is observed. Between 0.74THz and 0.86THz, an interesting phenomenon occurs: the emerging positively refracted wave front gradually diminishes in intensity while a negatively refracted wave front gradually increases in intensity, with a seemingly equal wave intensity observed at frequencies 0.80-0.82THz, where the plane wave seems to split at

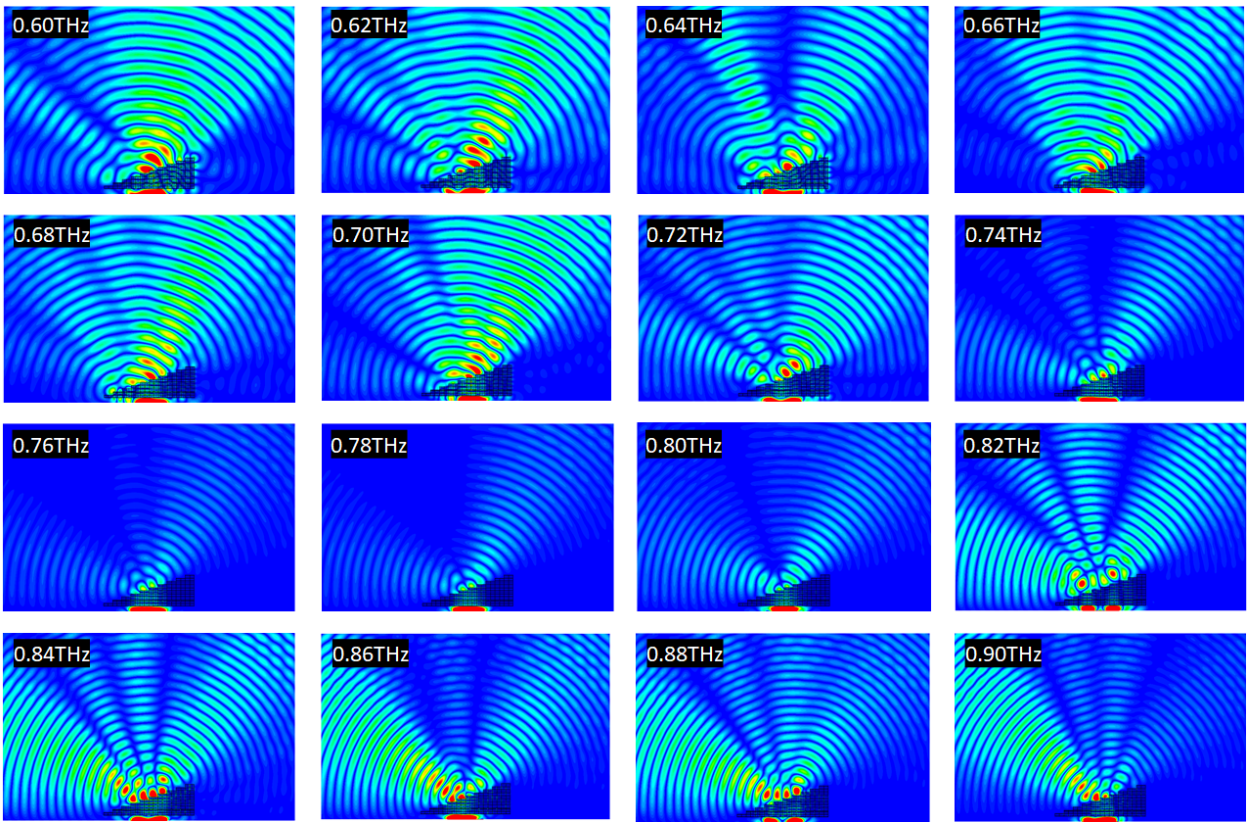

Figure 6.13: Absolute value of the electric field within and around a prism made of Paul *et al.*'s metamaterial for various frequencies when a plane wave is incident upon it, based on a numerical simulation.

the upper interface. This result will be investigated further in the next section.

Regardless of the ambiguity observed between frequencies 0.74-0.86THz, our observation allows us to extend the reported frequency spectrum over which negative refraction occurs (the grey zone in Fig. 6.7, a)) from starting at 0.96THz to starting at 0.86THz.

6.3 Numerical and theoretical investigation of the refractive index discontinuity

6.3.1 Modulo-2π transmission phase jump as a cause for refractive index discontinuity

So far, we have observed two cases of discontinuity: one that turned out to be a misapplication of the NRW algorithm (*i.e.* Chan *et al.*'s metamaterial), and one that turned out to be a shift in refractive index verified by numerical simulation (*i.e.* Paul *et al.*'s and Du *et al.*'s metamaterials).

Let us first investigate the case of Chan *et al.*'s metamaterial. Fig. 6.14 shows, side by side, the numerically retrieved transmission phase of the metamaterials, as well as the numerically retrieved refractive index with, in the case of Chan *et al.*, misuse of the NRW algorithm (*i.e.* non enforcement of the continuity requirement). One readily notices that refractive index discontinuities occur at the exact same frequencies as a "modulo jump" of the transmission phases: the latter discontinuities are expected from our numerical simulation software, which constrains the value of phase to the range $[-180deg; +180deg]$.

This phase discontinuity directly affects the NRW algorithm. Indeed, if one follows the dependence of n on S_{21} (see Eq. 4.11 and the definition of Θ in Section 4.3), an expression of the following form can be established for the real part of n:

$$\mathrm{Re}(n) = \frac{1}{k_0 d}\big[\mathrm{Im}(\ln \Delta) + 2\pi m\big] \tag{6.1}$$

with the full expression of Δ as:

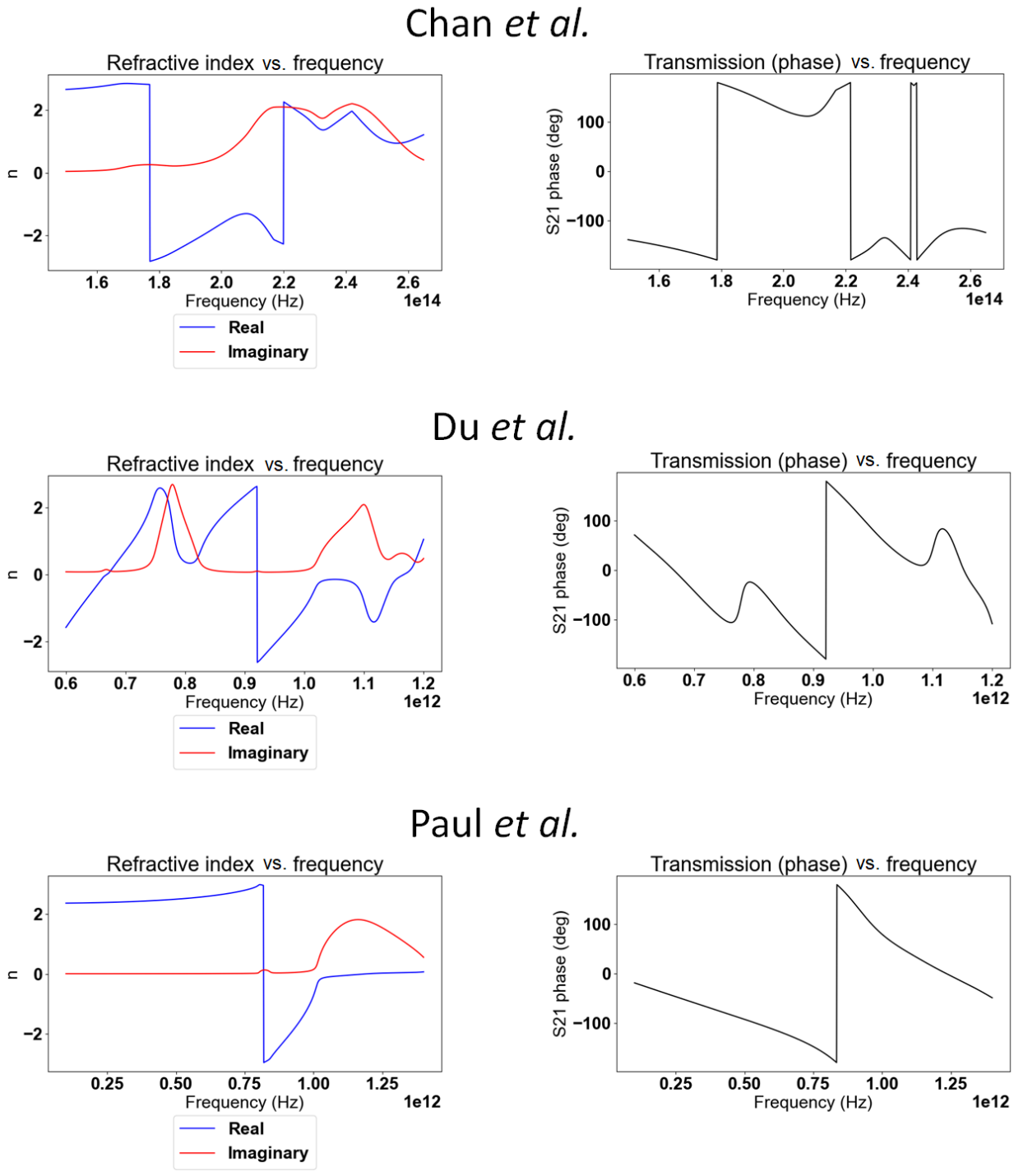

Figure 6.14: Comparison of numerical results of, from top to bottom, Chan *et al.*'s, Du *et al.*'s and Paul *et al.*'s metamaterials refractive index (left) and transmission phase (right). To note, Chan *et al.*'s refractive index is represented as obtained by misuse of the NRW algorithm.

$$\Delta = \frac{1 - S_{11}^2 + S_{21}^2}{2S_{21}} \pm i\sqrt{1 - \left(\frac{1 - S_{11}^2 + S_{21}^2}{2S_{21}}\right)^2}$$
$$= \frac{1}{2S_{21}}\left\{1 - S_{11}^2 + S_{21}^2 \pm \sqrt{\left[(S_{11} - S_{21})^2 - 1\right]\left[(S_{11} + S_{21})^2 - 1\right]}\right\} = \frac{\Lambda}{2S_{21}} \quad (6.2)$$

Replacing this expression in Eq. 6.1, we obtain:

$$\mathrm{Re}(n) = \frac{1}{k_0 d}\left[\mathrm{Im}\left(\ln\frac{\Lambda}{2S_{21}}\right) + 2\pi m\right] = \frac{1}{k_0 d}\left[\mathrm{Im}\left(\ln\frac{\Lambda}{2|S_{21}|}\right) - \arg[S_{21}] + 2\pi m\right] \quad (6.3)$$

In other words, the real part of the refractive index possesses a term that is directly proportional to the transmission phase. One notices a correspondance between this result and Fig. 6.14: the jumps in transmission phase and refractive index are opposite in direction, one going up when the other goes down, justified by the negative sign of the $\arg[S_{21}]$ term in Eq. 6.3. Furthermore, these phase jumps correspond *exactly* to a m-branch jump, since incrementing the m-branch index by one is equivalent to dropping the transmission phase by 360 degrees (2π). This is therefore proof that close monitoring of the m-branch index is able to solve mistaken discontinuities in the application of the NRW algorithm, such as with Chan *et al.*'s.

One would be tempted to formulate a rule to always accompany a transmission phase jump by a corresponding change in m-branch index, thereby always enforcing continuity. This, however, works only in the case where enforced continuity is validated by numerical simulations such as tests carried by prism refraction. In the cases of the metamaterials presented by Du *et al.* or Paul *et al.*, we have observed that a refractive index jump is necessary to justify the observed transition from positive to negative refraction.

6.3.2 Impact of refractive index discontinuity on the propagating wave

As seen in Eq. 6.3, a m-branch index jump leads to a decrement of $\frac{2\pi}{k_0 d}$. This impacts several variables related to the propagation of waves within the medium.

Assumming the metamaterial has interfaces with vacuum, where a plane wave propagates with wavelength λ_0, the wavelength within the metamaterial becomes $\lambda_{\text{meta}} = \frac{\lambda_0}{\text{Re}(n)}$. The substraction of a $\frac{2\pi}{k_0 d}$ term leads to a new wavelength within the metamaterial:

$$\lambda'_{\text{meta}} = \frac{\lambda_0}{\text{Re}(n) - \frac{2\pi}{k_0 d}} = \frac{1}{\frac{1}{\lambda_{\text{meta}}} - \frac{1}{d}} \tag{6.4}$$

This affects the propagating wave phase Φ, which becomes (assumming propagation in the z direction):

$$kz - \omega t = \frac{2\pi(z - \frac{ct}{n})}{\lambda_{\text{meta}}} \longrightarrow 2\pi \left(z - \frac{ct}{n - \frac{\lambda_0}{d}} \right) \left(\frac{1}{\lambda_{\text{meta}}} - \frac{1}{d} \right) = z \left(k - \frac{2\pi}{d} \right) - \omega t \tag{6.5}$$

One notices the term associated with spatial propagation has become negative (bearing in mind that $d \ll \lambda_{\text{meta}}$), as expected from the flip in wave vector $\mathbf{k}$ direction presented in section 2.3 (*i. e.* the wave vector $\mathbf{k}$ goes in the same direction as the Poynting vector in regular materials, but in the opposite direction in metamaterials).

Eq. 6.5 reveals that the phases at any boundary of a stack of unit cells remain unchanged after a refractive index jump, specifically being incremented by a multiple of 2π: considering a stack of thickness md with m a signed integer (including 0) and d the thickness of a single unit cell, the phase at $z = md$ passes, as the refractive index jumps to a lower m-branch index, from $mdk - \omega t$ to $mdk - 2\pi m - \omega t$. However, the sine wave within the metamaterial has been "flipped," as shown in Fig. 6.15. The angular frequency ω changes neither in value nor in sign, so that the wave internal to the metamaterial has now a negative phase velocity.

These considerations show that, while the topology of the effective wave has changed within the metamaterial, the dynamics of the phases remain unchanged at any time at the metamaterial's boundaries. Bearing in mind that the effective wave described by the effective parameters resolved by application of the NRW algorithm is just a convenient model of the metamaterial's properties, and not and actual description of the electromagnetic dynamic within, so that no actual "wave filp" occurs, the refractive index discontinuity is therefore

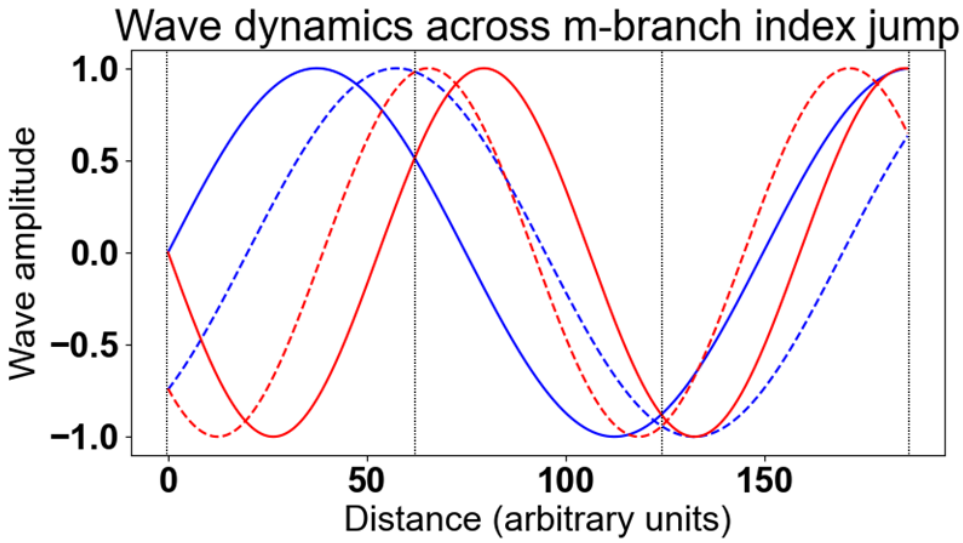

Figure 6.15: Example of the dynamics of waves across a m-branch index jump. Wave propagation is represented as, for a given color, solid line for the wave position at an instant t and dashed line for the wave position at an instant $t+\epsilon$. Blue wave represents propagation in a medium with positive refractive index (*i. e.* wave fronts moving towards the positive z), red wave represents propagation in a medium with negative refractive index after m-branch index jump (*i. e.* wave fronts moving towards the negative z). Vertical dashed black lines indicate the boundaries of each unit cell, where the phase of blue and red waves match at any time.

entirely compatible with the configuration of a layer of unit cells of thickness md upon which a plane wave is incident.

6.4 Conclusion

In this chapter, we have analyzed three instances of metamaterials reported in the literature who display a discontinuity on the frequency spectrum. We performed a numerical simulations of metamaterial unit cells with similar parameters as those described in those reports to ascertain a faithful reproduction of the report's research, and compared the results of our numerical simulations with those of those reports. We then performed a numerical simulation of a prism constituted of the aforementioned metamaterials, upon which was incident a

plane wave of frequency of resonance of the metamaterial. We were thus able to identify one metamaterial which did not display negative refraction, and two which were. In particular, we were able to identify that Paul *et al*'s metamaterial displays a beam-splitting phenomenon that warrants further research.

We identified further the cause leading to the emergence of the refractive index discontinuity, and developed a mathematical formalism to justify the connection between this discontinuity and the 2π modulo correction of the transmission phase. We finally demontrated that while this discontinuity leads to a change of the behavior of the effective electromagnetic wave within the metamaterial, the behavior of the electromagnetic wave external to the metamaterial remains unchanged, as this discontinuity does not affect the phase of the wave at the metamaterial's boundaries.

Chapter 7

CONCLUSION

In this thesis, we presented an overview of the history of the research on metamaterials, from its conceptual imagination by Veselago to a detailed analyzis of the currently most common designs. We discussed in details the NRW algorithm and two effective boundary retrieval algorithms. We proposed a novel design, the bd design, and demonstrated its superior characteristics, for various ranges of frequencies and scales, compared to mainstream metamaterial: lower loss, lower negative refractive index and larger span of frequencies during which negative refraction occurs. Finally, we presented an additional challenge observed in the literature: reports of discontinuity in the refractive index. We analyzed those reports and offer explanations for this phenomenon, as well as a numerical method to overcome this challenge.

The bd design discussed in Chapter 5 is a variation of the fishnet design that displays lower negative refractive index, lower loss and larger span of negative refraction frequencies than the modified fishnet it is inspired by. We demonstrated numerically, using three comparisons with scales ranging from nanometer to milimeter and wavelenghts ranging from GHz to PHz, that this novel design consistently lowers the refractive index, with a smallest progress of 63% for the Kafesaki design (-1.73 to -2.83) to a largest progress of 138% for the Zhang design (-1.38 to -3.29); that this design also consistently leads to a higher FOM, *i.e.* lower losses, with a smallest progress of 73% for the Zhang design (1.58 to 2.74) and a largest progress of 249% for the Kafesaki design (1.58 to 5.52). These improved performances are due to the displacement of the metallic arms, which prevents a magnetic oscillation in the dielectric arms countering the magnetic oscillation in the dielectric slab. Also, we demonstrated that a shear shift of the arms within the fishnet structure leads to a higher plasma frequency in

the wire array component of the fishnet, explaining the lower refractive index.

In Chapter 6 we reproduced numerical results of metamaterials by Chan, Du and Paul, to work of which claimed that the refractive index is discontinuous for their metamaterial. We introduced the idea of using a prism made of metamaterials and computing a numerical simulation of a frequency sweep of a plane wave incident upon this prism. This method demonstrated that no negative refraction is observed in the metamaterial suggested by Chan, but that a positive-to-negative refraction is observed in the case of Du and Paul's metamaterials. From the NRW algorithm derived the origin of this refractive index discontinuity, mainly a modulo jump in transmission phase, and demonstrated that this resolves the erroneous refractive index discontinuity of Chan. This modulo jump not being acknowledged by the NRW algorithm, it is therefore essential that a geometrical analysis, using a prism or any other shape, be carried whenever a discontinuous refractive index is observed. We further demonstrated that this discontinuity affects in no way the wave propagating beyond the unit cell, as the wave's phase remain identical on both sides of the discontinuity.

BIBLIOGRAPHY

[1] Mohammed Nurul Afsar, James R Birch, RN Clarke, and GW Chantry. The measurement of the properties of materials. *Proceedings of the IEEE*, 74(1):183–199, 1986.

[2] Andrea Alù. Restoring the physical meaning of metamaterial constitutive parameters. *Physical Review B*, 83(8):081102, 2011.

[3] David Bohm and David Pines. A collective description of electron interactions: Iii. coulomb interactions in a degenerate electron gas. *Physical Review*, 92(3):609, 1953.

[4] Alexandra Boltasseva and Harry A Atwater. Low-loss plasmonic metamaterials. *Science*, 331(6015):290–291, 2011.

[5] John Brown. Artificial dielectrics having refractive indices less than unity. *Proceedings of the IEE-Part IV: Institution Monographs*, 100(5):51–62, 1953.

[6] Robert Brown. The origin of the eskimo. *The Archaeological Review*, 1(4):237–253, 1888.

[7] D Bruce Burckel, Joel R Wendt, Gregory A Ten Eyck, James C Ginn, A Robert Ellis, Igal Brener, and Michael B Sinclair. Micrometer-scale cubic unit cell 3d metamaterial layers. *Advanced Materials*, 22(44):5053–5057, 2010.

[8] Hsun-Chi Chan, Shulin Sun, and Guang-Yu Guo. Near-infrared left-handed metamaterials made of arrays of upright split-ring pairs. *Journal of Physics D: Applied Physics*, 51(26):265103, 2018.

[9] Hongsheng Chen, Lixin Ran, Jiangtao Huangfu, Xianmin Zhang, Kangsheng Chen, Tomasz M Grzegorczyk, and Jin Au Kong. Left-handed materials composed of only s-shaped resonators. *Physical Review E*, 70(5):057605, 2004.

[10] Hou-Tong Chen, Willie J Padilla, Joshua MO Zide, Arthur C Gossard, Antoinette J Taylor, and Richard D Averitt. Active terahertz metamaterial devices. *Nature*, 444(7119):597–600, 2006.

[11] Xudong Chen, Tomasz M Grzegorczyk, Bae-Ian Wu, Joe Pacheco Jr, and Jin Au Kong. Robust method to retrieve the constitutive effective parameters of metamaterials. *Physical review E*, 70(1):016608, 2004.

[12] Muhan Choi, Seung Hoon Lee, Yushin Kim, Seung Beom Kang, Jonghwa Shin, Min Hwan Kwak, Kwang-Young Kang, Yong-Hee Lee, Namkyoo Park, and Bumki Min. A terahertz metamaterial with unnaturally high refractive index. *Nature*, 470(7334):369–373, 2011.

[13] Filippo Costa, Michele Borgese, Marco Degiorgi, and Agostino Monorchio. Electromagnetic characterisation of materials by using transmission/reflection (t/r) devices. *Electronics*, 6(4):95, 2017.

[14] P Ding, EJ Liang, WQ Hu, L Zhang, Q Zhou, and QZ Xue. Numerical simulations of terahertz double-negative metamaterial with isotropic-like fishnet structure. *Photonics and Nanostructures-Fundamentals and Applications*, 7(2):92–100, 2009.

[15] Gunnar Dolling, Christian Enkrich, Martin Wegener, Costas M Soukoulis, and Stefan Linden. Low-loss negative-index metamaterial at telecommunication wavelengths. *Optics letters*, 31(12):1800–1802, 2006.

[16] Gunnar Dolling, Martin Wegener, Costas M Soukoulis, and Stefan Linden. Negative-index metamaterial at 780 nm wavelength. *Optics letters*, 32(1):53–55, 2007.

[17] Qiujiao Du, Hongwu Yang, Xicheng Wang, and Tao Lv. An improved fishnet three-dimensional metamaterial with multiband left-handed characteristics at terahertz frequencies. *Optics Communications*, 285(6):980–985, 2012.

[18] N Garcia and M Nieto-Vesperinas. Left-handed materials do not make a perfect lens. *Physical review letters*, 88(20):207403, 2002.

[19] Anthony Grbic and George V Eleftheriades. Overcoming the diffraction limit with a planar left-handed transmission-line lens. *Physical review letters*, 92(11):117403, 2004.

[20] Allan Greenleaf, Yaroslav Kurylev, Matti Lassas, and Gunther Uhlmann. Electromagnetic wormholes and virtual magnetic monopoles from metamaterials. *Physical Review Letters*, 99(18):183901, 2007.

[21] Shuai Gu, Bin Su, and Xiaopeng Zhao. Planar isotropic broadband metamaterial absorber. *Journal of Applied Physics*, 114(16):163702, 2013.

[22] Christopher L Holloway, Edward F Kuester, Joshua A Gordon, John O'Hara, Jim Booth, and David R Smith. An overview of the theory and applications of metasurfaces: The two-dimensional equivalents of metamaterials. *IEEE Antennas and Propagation Magazine*, 54(2):10–35, 2012.

[23] GW't Hooft. Comment on "negative refraction makes a perfect lens". *Physical review letters*, 87(24):249701, 2001.

[24] Feng-Ju Hsieh and Wei-Chih Wang. Full extraction methods to retrieve effective refractive index and parameters of a bianisotropic metamaterial based on material dispersion models. *Journal of Applied Physics*, 112(6):064907, 2012.

[25] John David Jackson. *Classical electrodynamics*. John Wiley & Sons, 2007.

[26] Zubin Jacob, J-Y Kim, Gururaj V Naik, Alexandra Boltasseva, Evgenii E Narimanov, and Vladimir M Shalaev. Engineering photonic density of states using metamaterials. *Applied physics B*, 100(1):215–218, 2010.

[27] Muamer Kadic, Graeme W Milton, Martin van Hecke, and Martin Wegener. 3d metamaterials. *Nature Reviews Physics*, 1(3):198–210, 2019.

[28] M Kafesaki, I Tsiapa, N Katsarakis, Th Koschny, CM Soukoulis, and EN Economou. Left-handed metamaterials: The fishnet structure and its variations. *Physical Review B*, 75(23):235114, 2007.

[29] Saima Ishfaque Khan. *The optical properties of metamaterials*. PhD thesis, University of Glasgow, 2016.

[30] Th Koschny, M Kafesaki, EN Economou, and CM Soukoulis. Effective medium theory of left-handed materials. *Physical review letters*, 93(10):107402, 2004.

[31] Th Koschny, P Markoš, Eleftherios N Economou, DR Smith, DC Vier, and CM Soukoulis. Impact of inherent periodic structure on effective medium description of left-handed and related metamaterials. *Physical Review B*, 71(24):245105, 2005.

[32] Th Koschny, P Markoš, DR Smith, and CM Soukoulis. Resonant and antiresonant frequency dependence of the effective parameters of metamaterials. *Physical Review E*, 68(6):065602, 2003.

[33] Th Koschny, Lei Zhang, and CM Soukoulis. Isotropic three-dimensional left-handed metamaterials. *Physical Review B*, 71(12):121103, 2005.

[34] Edward F Kuester, Nadja Memic, Simone Shen, Aaron D Scher, Sung Kim, Kendra Kumley, and Hung Loui. A negative refractive index metamaterial based on a cubic array of layered nonmagnetic spherical particles. *Progress In Electromagnetics Research*, 33:175–202, 2011.

[35] Irving Langmuir. Oscillations in ionized gases. *Proceedings of the National Academy of Sciences of the United States of America*, 14(8):627, 1928.

[36] Ulf Leonhardt. Optical conformal mapping. *science*, 312(5781):1777–1780, 2006.

[37] Xiaoliang Ma, Wenbo Pan, Cheng Huang, Mingbo Pu, Yanqin Wang, Bo Zhao, Jianhua Cui, Changtao Wang, and Xiangang Luo. An active metamaterial for polarization manipulating. *Advanced Optical Materials*, 2(10):945–949, 2014.

[38] R Marques and DR Smith. Comment on "electrodynamics of metallic photonic crystals and the problem of left-handed materials". *Physical review letters*, 92(5):059401, 2004.

[39] Christoph Menzel, Carsten Rockstuhl, Thomas Paul, Falk Lederer, and Thomas Pertsch. Retrieving effective parameters for metamaterials at oblique incidence. *Physical Review B*, 77(19):195328, 2008.

[40] Keshav Samrat Modi, Jasleen Kaur, Satya Pratap Singh, Umesh Tiwari, and Ravindra Kumar Sinha. Extremely high figure of merit in all-dielectric split asymmetric arc metasurface for refractive index sensing. *Optics Communications*, 462:125327, 2020.

[41] Carol Gray Montgomery. Technique of microwave measurements. *MIT Radiation Laboratory Series*, 11:561–570, 1947.

[42] Adrian I Nachman. Reconstructions from boundary measurements. *Annals of Mathematics*, 128(3):531–576, 1988.

[43] Evgenii E Narimanov, H Li, Yu A Barnakov, TU Tumkur, and MA Noginov. Reduced reflection from roughened hyperbolic metamaterial. *Optics express*, 21(12):14956–14961, 2013.

[44] AM Nicolson and GF Ross. Measurement of the intrinsic properties of materials by time-domain techniques. *IEEE Transactions on instrumentation and measurement*, 19(4):377–382, 1970.

[45] MA Noginov, H Li, Yu A Barnakov, D Dryden, G Nataraj, G Zhu, CE Bonner, M Mayy, Z Jacob, and EE Narimanov. Controlling spontaneous emission with metamaterials. *Optics letters*, 35(11):1863–1865, 2010.

[46] Stephen O'Brien and John B Pendry. Photonic band-gap effects and magnetic activity in dielectric composites. *Journal of Physics: Condensed Matter*, 14(15):4035, 2002.

[47] Mark A Ordal, Robert J Bell, Ralph W Alexander, Larry L Long, and Marvin R Querry. Optical properties of fourteen metals in the infrared and far infrared: Al, co, cu, au, fe, pb, mo, ni, pd, pt, ag, ti, v, and w. *Applied optics*, 24(24):4493–4499, 1985.

[48] Oliver Paul, Christian Imhof, Bert Lägel, Sandra Wolff, Jan Heinrich, Sven Höfling, Alfred Forchel, Remigius Zengerle, René Beigang, and Marco Rahm. Polarization-independent active metamaterial for high-frequency terahertz modulation. *Optics express*, 17(2):819–827, 2009.

[49] Oliver Paul, Christian Imhof, Benjamin Reinhard, Remigius Zengerle, and René Beigang. Negative index bulk metamaterial at terahertz frequencies. *Optics express*, 16(9):6736–6744, 2008.

[50] John B Pendry, AJ Holden, DJ Robbins, and WJ Stewart. Low frequency plasmons in thin-wire structures. *Journal of Physics: Condensed Matter*, 10(22):4785, 1998.

[51] John B Pendry, AJ Holden, WJ Stewart, and I Youngs. Extremely low frequency plasmons in metallic mesostructures. *Physical review letters*, 76(25):4773, 1996.

[52] John B Pendry, Anthony J Holden, David J Robbins, and WJ Stewart. Magnetism from conductors and enhanced nonlinear phenomena. *IEEE transactions on microwave theory and techniques*, 47(11):2075–2084, 1999.

[53] John B Pendry, David Schurig, and David R Smith. Controlling electromagnetic fields. *science*, 312(5781):1780–1782, 2006.

[54] John Brian Pendry. Negative refraction makes a perfect lens. *Physical review letters*, 85(18):3966, 2000.

[55] Carl Pfeiffer, Naresh K Emani, Amr M Shaltout, Alexandra Boltasseva, Vladimir M Shalaev, and Anthony Grbic. Efficient light bending with isotropic metamaterial huygens' surfaces. *Nano letters*, 14(5):2491–2497, 2014.

[56] David Pines and David Bohm. A collective description of electron interactions: Ii. collective vs individual particle aspects of the interactions. *Physical Review*, 85(2):338, 1952.

[57] D Polder. Viii. on the theory of ferromagnetic resonance. *The London, Edinburgh, and Dublin Philosophical Magazine and Journal of Science*, 40(300):99–115, 1949.

[58] AG Ramm. Does negative refraction make a perfect lens? *Physics Letters A*, 372(43):6518–6520, 2008.

[59] William S Rodney and Robert J Spindler. Index of refraction of fused quartz glass for ultraviolet, visible, and infrared wavelengths. *JOSA*, 44(9):677–679, 1954.

[60] Walter Rotman. Plasma simulation by artificial dielectrics and parallel-plate media. *IRE Transactions on Antennas and Propagation*, 10(1):82–95, 1962.

[61] David Schurig, Jack J Mock, BJ Justice, Steven A Cummer, John B Pendry, Anthony F Starr, and David R Smith. Metamaterial electromagnetic cloak at microwave frequencies. *Science*, 314(5801):977–980, 2006.

[62] Richard A Shelby, DR Smith, SC Nemat-Nasser, and Sheldon Schultz. Microwave transmission through a two-dimensional, isotropic, left-handed metamaterial. *Applied Physics Letters*, 78(4):489–491, 2001.

[63] Zhongyan Sheng and Vasundara V Varadan. Tuning the effective properties of metamaterials by changing the substrate properties. *Journal of applied physics*, 101(1):014909, 2007.

[64] VP Shestopalov and KP Yatsuk. Methods of measuring dielectric constants of substances at microwave frequencies. *Soviet Physics Uspekhi*, 4(4):617, 1962.

[65] Dongheok Shin, Junhyun Kim, Do-Sik Yoo, and Kyoungsik Kim. Design of 3d isotropic metamaterial device using smart transformation optics. *Optics express*, 23(17):21892–21898, 2015.

[66] Ari Sihvola. Metamaterials in electromagnetics. *Metamaterials*, 1(1):2–11, 2007.

[67] Mário Silveirinha and Nader Engheta. Tunneling of electromagnetic energy through subwavelength channels and bends using ε-near-zero materials. *Physical review letters*, 97(15):157403, 2006.

[68] CR Simovski and PA Belov. Low-frequency spatial dispersion in wire media. *Physical Review E*, 70(4):046616, 2004.

[69] CR Simovski and B Sauviac. Role of wave interaction of wires and split-ring resonators for the losses in a left-handed composite. *Physical Review E*, 70(4):046607, 2004.

[70] David R Smith, Willie J Padilla, DC Vier, Syrus C Nemat-Nasser, and Seldon Schultz. Composite medium with simultaneously negative permeability and permittivity. *Physical review letters*, 84(18):4184, 2000.

[71] David R Smith, WJ Padilla, DC Vier, R Shelby, SC Nemat-Nasser, N Kroll, and S Schultz. Left-handed metamaterials. In *Photonic crystals and light localization in the 21st century*, pages 351–371. Springer, 2001.

[72] DR Smith, DC Vier, Th Koschny, and CM Soukoulis. Electromagnetic parameter retrieval from inhomogeneous metamaterials. *Physical review E*, 71(3):036617, 2005.

[73] GHB Thompson. Unusual waveguide characteristics associated with the apparent negative permeability obtainable in ferrites. *Nature*, 175(4469):1135–1136, 1955.

[74] Sergei A Tretyakov. A personal view on the origins and developments of the metamaterial concept. *Journal of Optics*, 19(1):013002, 2016.

[75] Mankei Tsang and Demetri Psaltis. Magnifying perfect lens and superlens design by coordinate transformation. *Physical Review B*, 77(3):035122, 2008.

[76] Jason Valentine, Shuang Zhang, Thomas Zentgraf, Erick Ulin-Avila, Dentcho A Genov, Guy Bartal, and Xiang Zhang. Three-dimensional optical metamaterial with a negative refractive index. *nature*, 455(7211):376–379, 2008.

[77] IB Vendik, MA Odit, and DS Kozlov. 3d isotropic metamaterial based on a regular array of resonant dielectric spherical inclusions. *Metamaterials*, 3(3-4):140–147, 2009.

[78] Victor Georgievich Veselago. The electrodynamics of substances with simultaneously negative values of ϵ and μ. *Physics-Uspekhi*, 10(4):509–514, 1968.

[79] Rodger M Walser. Metamaterials: What are they? what are they good for? In *APS March Meeting Abstracts*, 2000.

[80] William B Weir. Automatic measurement of complex dielectric constant and permeability at microwave frequencies. *Proceedings of the IEEE*, 62(1):33–36, 1974.

[81] P Weis, O Paul, C Imhof, R Beigang, and M Rahm. Strongly birefringent metamaterials as negative index terahertz wave plates. *Applied Physics Letters*, 95(17):171104, 2009.

[82] William B Westphal and AR Von Hippel. Dielectric materials and applications. *ed. Hippel, A. von, Tech. Press of MIT and J. Wiley, NY*, page 63, 1954.

[83] Emil Wolf and Tarek Habashy. Invisible bodies and uniqueness of the inverse scattering problem. *Journal of Modern Optics*, 40(5):785–792, 1993.

[84] J Woodley and M Mojahedi. On the signs of the imaginary parts of the effective permittivity and permeability in metamaterials. *JOSA B*, 27(5):1016–1021, 2010.

[85] Shumin Xiao, Vladimir P Drachev, Alexander V Kildishev, Xingjie Ni, Uday K Chettiar, Hsiao-Kuan Yuan, and Vladimir M Shalaev. Loss-free and active optical negative-index metamaterials. *Nature*, 466(7307):735–738, 2010.

[86] Ta-Jen Yen, WJ Padilla, Nicholas Fang, DC Vier, DR Smith, JB Pendry, DN Basov, and Xiang Zhang. Terahertz magnetic response from artificial materials. *Science*, 303(5663):1494–1496, 2004.

[87] Kai-Lun Zhang, Zhi-Ling Hou, Ling-Bao Kong, Hui-Min Fang, and Ke-Tao Zhan. Origin of negative imaginary part of effective permittivity of passive materials. *Chinese Physics Letters*, 34(9):097701, 2017.

[88] Shuang Zhang, Wenjun Fan, KJ Malloy, SRJ Brueck, NC Panoiu, and RM Osgood. Near-infrared double negative metamaterials. *Optics Express*, 13(13):4922–4930, 2005.

[89] Shuang Zhang, Wenjun Fan, NC Panoiu, KJ Malloy, RM Osgood, and SRJ Brueck. Experimental demonstration of near-infrared negative-index metamaterials. *Physical review letters*, 95(13):137404, 2005.

[90] Jiangfeng Zhou, Eleftherios N Economon, Thomas Koschny, and Costas M Soukoulis. Unifying approach to left-handed material design. *Optics Letters*, 31(24):3620–3622, 2006.

Appendix A

DERIVATIONS

A.1 Expression of the effective permeability of capacitative arrays of sheets wound on cylinders and of the "swiss roll" capacitor (Section 2.3)

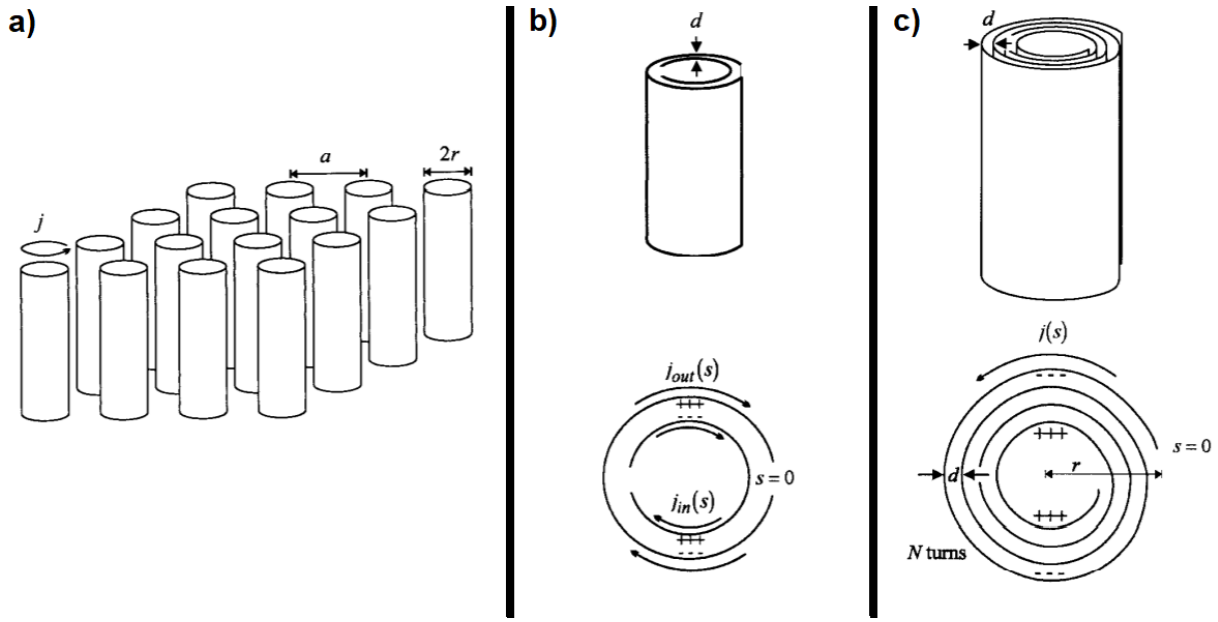

Figure A.1: Microstructures proposed by Pendry: a) array of cylinders; b) capacitative arrays of sheets wound on cylinders; c) "swiss roll" capacitor (reproduced from [52]).

A.1.1 Cylinders array

Considering a square array of hollow metallic cylinders (Fig. A.1 a)). When an external magnetic field strength H_0 is applied onto this microstructures, aligned with the direction of the cylinders, this generates an internal magnetic field strength H within the cylinders of the form:

$$H_{int} = H_0 + j(1 - F) \tag{A.1}$$

with j the surface current flowing over the cylinders, $F = \frac{\pi r^2}{a^2}$ the fractional volume of space occupied by the cylinders and their interior, and r and a defined in Fig. 2.2 a). The total electromotive force around the circumference of a cylinder needs to remain zero, therefore:

$$\text{emf} = -\pi r^2 \mu_0 \frac{\partial H_{int}}{\partial t} - 2\pi r \sigma j = 0 \tag{A.2}$$

with σ the resistance per unit area of the cylinder's surface. This leads to an expression for the surface current:

$$j = -\frac{H_0}{1 - F + i\frac{2r\sigma}{\omega r^2 \mu_0}} \tag{A.3}$$

Using the expression of this surface current to compute the average magnetic field strength *outside* of the cylinders $\overline{H}_{ext} = H_0 - Fj$ and noting the average magnetic flux density $\overline{B} = \mu_0 H_0$, the expression for the effective permittivity of this structure becomes:

$$\mu_{\text{eff}}^{\text{cyl}} = \frac{\overline{B}}{\mu_0 \overline{H}_{ext}} = 1 - \frac{F}{1 + i\frac{2\sigma}{\omega r \mu_0}} \tag{A.4}$$

A.1.2 Capacitative arrays of sheets wound on cylinders

In the case of capacitative arrays of sheets wound on cylinders, or split cylinders resonators (SCR), the derivation is very similar but for a capacitance term that slightly modifies the expression of the internal magnetic field strength so that the effective permeability of this microstructure become:

$$\mu_{\text{eff}}^{\text{SCR}} = \frac{\overline{B}}{\mu_0 \overline{H}_{ext}} = 1 - \frac{F}{1 + i\frac{2\sigma}{\omega r \mu_0} - \frac{3}{\pi^2 \mu_0 \omega^2 C r^3}} \tag{A.5}$$

with the capacitance defined as $C = \frac{\varepsilon_0}{d}$ with d the distance of the cylinder's split.

A.2 Expression of the transmission of an incident wave upon a NIM-made optical system (Section 2.6.2)

Considering a TE-polarized electric evanescent wave of unity amplitude in vacuum, with electric field:

$$\mathbf{E} = e^{i(k_x x + k_z z - \omega t)}\mathbf{e_y} \tag{A.6}$$

Evanescence implies $k_x > \frac{\omega}{c}$ and $k_z = i\sqrt{k_x^2 - \frac{\omega^2}{c^2}}$. When incident upon a material of properties ε, μ, part of that electric wave is transmitted:

$$\mathbf{E} = t_{\text{in}} e^{i(k_x x + k'_z z - \omega t)}\mathbf{e_y} \tag{A.7}$$

with $k_x > \frac{\omega}{c}\sqrt{\varepsilon\mu}$ and $k'_z = i\sqrt{k_x^2 - \frac{\omega^2}{c^2}\varepsilon\mu}$.

Wave fields are continuous across interfaces, leading to:

$$t = \frac{2\mu k_z}{\mu k_z + k'_z} \tag{A.8}$$

and similarly at the material's outlet:

$$t_{\text{out}} = \frac{2k'_z}{\mu k_z + k'_z} \tag{A.9}$$

Transmittance across a thickness d of the material can then be calculated, taking into account the possibility of infinite internal reflections:

$$T = t_{\text{in}} t_{\text{out}} \sum_{i=0}^{\infty} r_{\text{out}}^{2i} e^{i(2i+1)k'_z d} = \frac{t_{\text{in}} t_{\text{out}} e^{ik'_z d}}{1 - r_{\text{out}}^2 e^{i2k'_z d}} \tag{A.10}$$

with r_{out} the outlet reflection defined by:

$$r_{\text{in/out}} = \pm\frac{\mu k_z - k'_z}{\mu k_z + k'_z} \tag{A.11}$$

Taking the limit $\varepsilon, \mu \to -1$ leads to:

$$T \to e^{-ik_z d} \tag{A.12}$$

Similar result is achieved for TM polarized waves.

VITA

Antoine Wegrowski was born in France. Obtained a Bachelor in Physics from the Universite Pierre et Marie Curie in Paris (France), then a Master in Physics at Osaka University, Osaka (Japan).